MASTERARBEIT | MASTER'S THESIS

Titel | Title

Dark state pair-production in underground accelerators and their detection

verfasst von | submitted by

Maximilian Fahrecker BSc

angestrebter akademischer Grad | in partial fulfilment of the requirements for the degree of

Master of Science (MSc)

Wien | Vienna, 2025

Studienkennzahl lt. Studienblatt | Degree programme code as it appears on the student record sheet:	UA 066 876
Studienrichtung lt. Studienblatt | Degree programme as it appears on the student record sheet:	Masterstudium Physics
Betreut von | Supervisor:	Assoz. Prof. Mag. Dr. Josef Pradler

Zusammenfassung

Die Suche nach der Natur von dunkler Materie dauert an. Im Falle von dunkler Materie in Teilchenform geschieht dies üblicherweise mittels Einschränkung des Parameterraums. In dieser Arbeit erforschen wir die Möglichkeit neuer leichter Fermionen mit Milli-Ladung oder elektromagnetischen Formfaktor-Wechselwirkungen. Diese Teilchen kommen als Kandidaten für dunkle Materie in Frage. Wir untersuchen die Produktion von solchen Teilchen und deren nachfolgende Detektion mittels CCD-Sensoren in unterirdischen Labors. Wir berechnen die S-Matrixelemente und die Phasenräume analytisch und werten danach die zugehörigen Wechselwirkungsquerschnitte numerisch aus. Letztendlich besprechen wir Einschränkungen des Parameterraums durch kosmologische und astrophysikalische Beobachtungen sowie durch Hochpräzisions-Teilchenphysik. Die theoretischen Ergebnisse können dann mit zukünftigen Messungen verglichen werden.

Abstract

The search for the nature of dark matter continues. In the case of particle dark matter this is usually done by constraining the parameter space. In this thesis we explore the possibility of new light fermionic particles with millicharge or electromagnetic form factor interactions. These could be dark matter candidates. We investigate the underground production of such particles via an electron beam and their subsequent detection using a CCD-sensor. We evaluate the S-matrix elements and the phase spaces analytically, and then calculate the corresponding cross sections numerically. Finally, we will discuss observational constraints from cosmology, astrophysics and high-precision particle physics. These theoretical results can then be checked against future measurements.

Acknowledgements

I am tremendously grateful to my supervisor Josef Pradler for his support and guidance of the work culminating in this thesis. I am also very thankful to Helmut Eberl for his great help in double-checking my numerical calculations. I thank Xiaoyong Chu and Stephan Nellen-Mondragon for helpful discussions. Additionally, I want to thank Massimiliano Procura for his recommendation as a Master Fellow.

Ich möchte noch meiner Familie danken, die mich während meines Studiums immer unterstützt hat, insbesondere in der Corona-Zeit, die auch meine Studienzeit geprägt hat. Außerdem möchte ich mich bei meinem ehemaligen Biologielehrer Günther Geber dafür bedanken, dass er mich stets ermutigt hat, die Naturwissenschaften weiterzuverfolgen.

This thesis was graciously supported by a Master Fellowship from the Vienna Doctoral School in Physics.

Contents

1 Introduction

1.1 Dark Matter Overview

The concept of dark matter initially arose from discrepancies in astronomical observations. In 1933 Fritz Zwicky noticed that the velocity dispersion of galaxies in clusters could not be explained by its visible matter alone [1]. Rather, he postulated, there existed non-luminous gravitating matter, which he named in German *dunkle Materie*, or *dark matter* (DM) in English. Using the virial theorem, he worked out that the abundance of dark matter must be greater than that of the luminous constituent of the cluster. This was the first sign of the existence of dark matter in the universe. Later, it was noticed, by Vera Rubin and others [2], that the rotation curves of galaxies, i.e. the average orbital velocity of a star at a given distance from the galactic centre, strayed from the expectation of ordinary Newtonian gravity [3]. It was then realised, that this deviation could be explained if spiral galaxies were surrounded by a diffuse dark matter halo, supplying the seemingly missing mass needed for the Newtonian prediction to align with observations. When the cosmic microwave background (CMB) was discovered in 1964/1965 [4], it corroborated the Big Bang model. This discovery, together with the need to explain large scale structure formation and the anisotropies in the CMB, lead to dark matter being postulated to dominate the total matter density in the universe [5]. The standard cosmological model, named ΛCDM from its reliance on the cosmological constant Λ and on cold dark matter (CDM), subsequently emerged. Thus, today the strongest evidence for dark matter comes from cosmological measurements and the large scale structure of the universe.

The biggest remaining issue with dark matter is its nature, or put simply: What *exactly* is dark matter? There have been numerous proposed explanations, ranging from large astrophysical objects to extraordinarily light particles. Regardless of the true character of DM, its candidates must posses certain characteristics [6]. They cannot interact strongly with electromagnetism, they must be massive and their average kinetic energy must be small (referred to as cold). These basic conditions are not very limiting, and are even met by standard model neutrinos, save for naturally occurring neutrinos being predominantly relativistic and thus not cold. Additionally, the DM candidates must have an underlying theory predicting the correct relic abundance and be compatible with the early universe in terms of Big Bang nucleosynthesis and other constraints. Hence, dark matter as new particles beyond the Standard Model is well motivated by these considerations, especially since baryonic DM such as MACHOs [7], have been increasingly ruled out as a dominant part of dark matter. Accordingly, there exists a large landscape of theoretical models for DM, some of which we will expand on later.

1.2 Dark Matter Evidence

Although it has continued to evade detection, the dominant scientific consensus is still that dark matter exists. Numerous pieces of evidence [5, 6] have been found and, crucially, some that are very difficult to explain without DM [8]. This evidence exists for phenomena of different scales. At first let us focus on the *intermediate* cosmic scale, i.e. galaxies and clusters. Something that is often taken as prime example for DM in popular science and introductory courses, although it is not a conclusive signature, are *galaxy rotation curves*. When plotting a star's position from the centre of its spiral host galaxy R against its galactic orbital velocity v, it is possible to describe the relationship between these quantities using a galaxy rotation curve. A theoretical prediction on the form of this curve using ordinary Newtonian mechanics and the content of luminous matter in the spiral galaxy yields a rigid body rotation $v \sim R$ for the dense bulge (i.e. the innermost part of the galaxy) and a Keplerian $v \sim 1/R^2$ curve in the spiral arms. This, however, was not measured by astronomers. Instead they discovered that most stars in typical spiral galaxies rotate at about the same velocity [2]. This would defy Newtonian gravity in the absence of additional, non-luminous, matter. It was quickly realised that the missing mass could be a new type of neutral dark matter, explaining the anomalous rotation curves [3]. However, the anomaly could also be explained by modifying Newtonian mechanics in a certain way, which will be discussed in more detail below.

As aforementioned, DM was originally introduced in 1933 by Fritz Zwicky [1]. He noted that the velocity dispersion of the galaxies in the Coma cluster, meaning the statistical deviation from the mean velocity of the components of an astrophysical object or structure, could not be explained by its luminous matter alone. Using the virial theorem he then predicted the amount of invisible dark matter in the cluster and came up with a number exceeding today's accepted value. This was mainly due to the value of the Hubble constant he used, which was very different from current accepted values [3]. Regardless of the incorrect calculation of the ratio of DM to luminous matter by Zwicky, the cluster's velocity dispersion still needed missing mass to be explained. Since then, telescopes have improved in capability such that they are able to detect the baryonic matter in clusters in great detail. This is especially interesting in conjunction with *gravitational lensing* [6]. Einstein's theory of general relativity predicts that light gets bent by matter. This can lead to massive cosmic structures acting as optical lenses by focussing light, hence gravitational lensing. Through this effect, it is possible to see structures that would otherwise be too faint to detect or obscured behind closer objects. Broadly speaking, there are two types of gravitational lensing, namely strong and weak. Strong lensing happens when the lens is compact and produces significant distortion of the object being lensed, thus resulting in elongated images in a circle around the lensing mass, commonly called Einstein rings. This effect can also create multiple images of the same lensed source. The second type is weak lensing. Here, light sources are slightly lensed by the general distribution of large scale structures. This effect is only detectable using statistical methods. The significance of gravitational lensing as dark matter evidence becomes clear when realising one can use the strength of it to determine the total mass of large structures and, more importantly, how that mass is distributed. When applying weak lensing methods to clusters, their measured mass exceeds their detectable luminous mass [8, 9, 10] and thus hints at dark matter. Even stronger evidence for DM comes from the 1E0657-558 merging cluster, called Bullet cluster, specifically [8, 11], pictured in Fig. 1.

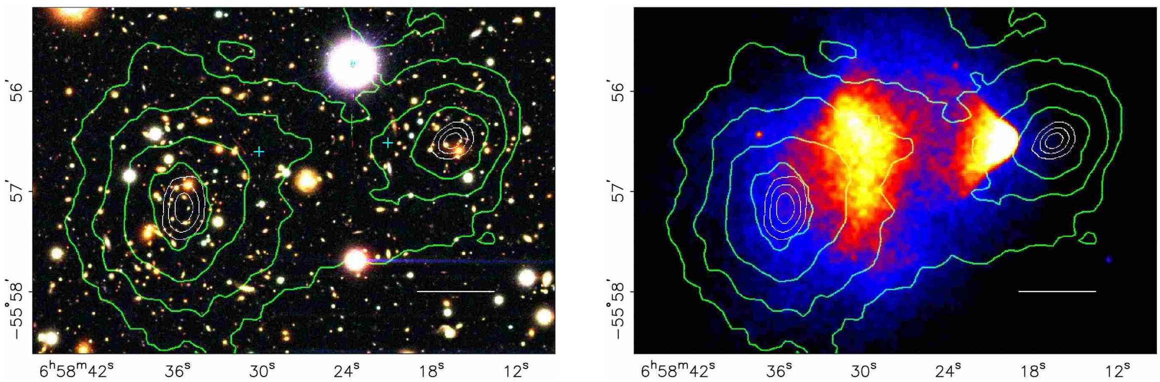

Figure 1: The left image by the Magellan Telescope depicts the Bullet cluster with superimposed mass contour lines inferred from gravitational lensing. The right image shows Chandra X-ray observations of the 1E0657-558 cluster, with the bullet visible, again superimposed by the contours. These two images clearly display the discrepancy between the centres of mass of the subclusters and the bulk of baryonic matter in the whole system; from [12].

As the name suggests, the bullet cluster underwent an interaction in which two clusters collided, where one “shot” through the other like a bullet. The stars inside the constituent galaxies hardly interacted during the collision and largely stayed bound to their respective host. Importantly, the main baryonic component of clusters and galaxies, ionised gas, does interact through electromagnetism and undergoes a shock when colliding, which can be observed, as seen in Fig. 1, using X-ray astronomy. This strips the clusters and their galaxies of most of their gas, which remains at the centre of the collision. Thus, the baryonic matter distribution shifts away from the galaxies towards the stripped gas while the dark matter distribution remains largely unchanged. We can then measure the distribution of mass in the Bullet cluster using weak lensing and compare it to the distribution from luminous matter alone. If they align, then no DM is needed to explain the lensing. When the measurement was taken, it was discovered that the effect is strongest around two lenses, namely the two clusters with their galaxies and DM halos and not the gas in the collision centre [8, 12]. This is extraordinarily difficult to explain without dark matter and thus the Bullet cluster is often named as a *smoking gun* signature for it. Additionally, it confirms that dark matter is largely collisionless, as the cluster's halos passed through each other without forming a shock and thus, puts limits on DM self-interaction [11]. The implications of this with regards to alternate theories of gravity will be discussed later.

All the evidence above comes from galactic and cluster scale structures and thus from later stages in the universe's cosmic history. This is due to the difficulty of observing the cosmos at times between the decoupling of the CMB and the advent of reionisation, even with the James Webb Space Telescope. Indeed, dark matter would not be so widely accepted if it was not so successful at explaining multiple phenomena at different scales. The very early universe, when it was still hot and dense, as predicted by Big Bang cosmology [5, 6], provides strong dark matter evidence as well. As we now know, the matter content in the universe consists of about 84% [13] dark matter, the rest being ordinary baryonic matter. This can be measured using multiple ways ranging from astrophysical to CMB methods that all have to align to get a consistent model.

The most extensive and definitive evidence for dark matter today comes from the cosmic microwave background [5, 13]. This radiation was emitted during the epoch of recombination at about redshift $z \approx 1100$ (ca. 380 000 years after the Big Bang [13]) when the universe first became neutral and transparent. When measuring this highly redshifted radiation it is possible to observe a nearly perfect black body spectrum with a temperature of about 2.7 K [13]. The primordial density fluctuations, that later went on to form the large scale structure of the universe we see today, are imprinted in the anisotropies of this spectrum. The way in which the CMB power spectrum, seen in Fig. 2, relates to the ΛCDM model, can be used to determine cosmological parameters by measuring this primordial radiation [14]. This yields yet another method for finding the dark matter abundance to compare to other predictions. For DM in particular, an important feature in the CMB power spectrum are baryo-acoustic oscillations, or BAO for short, visible as the peaks and troughs in Fig. 2. Here, the interplay of gravity and electromagnetism created oscillations of baryons in the primordial plasma. BAOs provide a telltale sign for DM, as the relative heights of the peaks in the spectrum give constraints on the relative abundance of dark to baryonic matter [15]. These oscillations are thought to be formed by dark matter potential wells attracting baryons. When the density of these baryons becomes high enough, radiation pressure forces them to expand again, but the DM remains and the cycle starts anew. The angular size of the anisotropies caused by BAOs is limited by the sound horizon, i.e. the distance these density waves could travel before decoupling. These anisotropies then provide the seeds for large scale structure (LSS) formation in the universe. LSS formation is dominated by dark matter, so much so that large modelling of it can often neglect baryons [16]. Extensive numerical simulations have shown that a dark matter dominated LSS can explain our present universe to a high degree [17]. The short discussion of some of the most widely accepted evidence for dark matter presented here, was just an overview to reassure ourselves that investigating DM, and ideally finding it, is crucial for modern cosmology. However, such an argument would be incomplete without briefly mentioning competing theories.

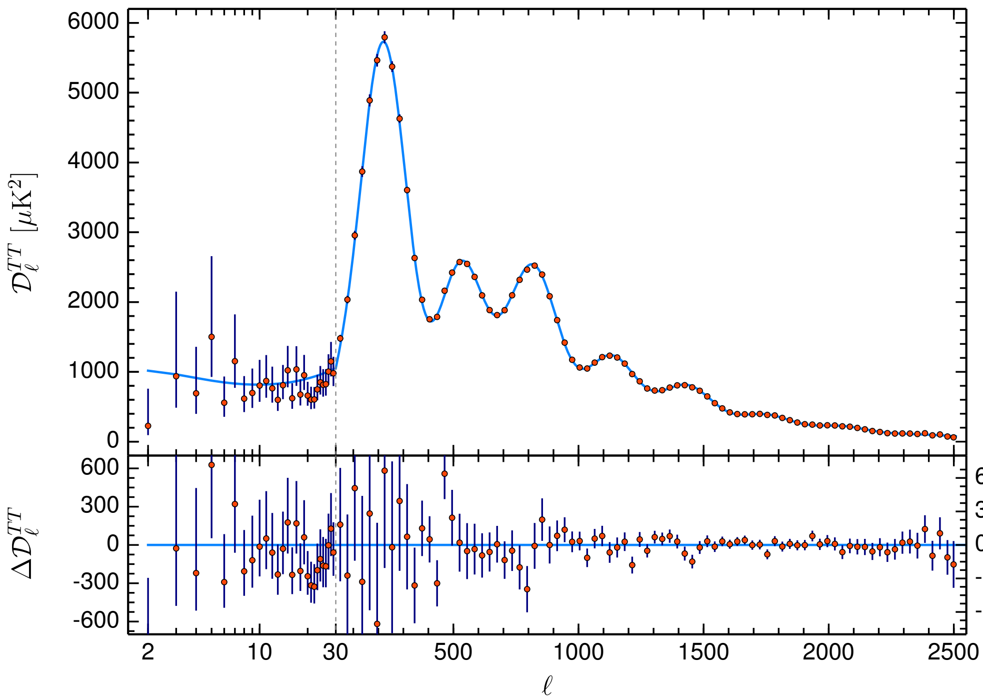

Figure 2: The temperature power spectrum D_ℓ^{TT} of the CMB as measured by the Planck space probe in 2018 with its residuals in the lower panel. Clearly visible are the baryon-acoustic oscillation peaks and troughs for medium multipoles ℓ; from [13].

While dark matter, and with it ΛCDM, is the most widely accepted theory of cosmology, some proponents of alternate theories do exist. A classic example of a simple way to do away with the need for dark matter in the context of galaxy rotation curves is modified Newtonian dynamics, or MOND [18]. In this non-relativistic theory, either Newton's second law or Newtonian gravity is modified at accelerations typically occurring in the outer regions of spiral galaxies, namely at around 10^{-8} cm/s^2 [6]. This scale is determined by fitting the modified law of gravity to rotation curve data. Standard MOND in particular is non-relativistic, so cannot describe a wide array of gravitational effects. Theories like MOND and its numerous different relativistic generalisations are called *modified gravity* or MOG. A number of proponents have also claimed that MOG models can accommodate the phenomenology of the CMB, although this is disputed [6]. Incidentally, the philosophy behind the two different approaches explaining anomalous behaviour of gravity has a long history. It is reminiscent of Urbain Le Verrier [3], who predicted the existence of Neptune by explaining the deviation of Uranus' orbit from the Newtonian model by postulating a yet unobserved object beyond its orbit. This approach mirrors dark matter, were gravitational anomalies are due to additional unseen mass. But Le Verrier can also be used as an example for a failure of this explanation. The perihelion drift of the orbit of Mercury had too been observed to deviate from the Newtonian case. Le Verrier predicted it to be yet another unseen object orbiting between Mercury and the sun. He named it Vulcan and soon it was thought to be discovered. Although later, as we now know, it turned out to not exit. Instead Newtonian gravity itself needed to be modified and replaced by Einstein's general theory of relativity. The conclusion of this historical note is, that neither missing mass nor modified gravity solutions are a priori superior, if they predict similar phenomenology. The only way to distinguish them is by doing observations and comparing the predictions of each theory. The reason modified gravity is currently less favoured than DM, is that MOG models usually fail to predict the wide array of phenomena describable by ΛCDM. Going back to the bullet cluster as an example, here most MOG theories are thought to be incapable of explaining the observed gravitational lensing [10, 12]. A modification to the law of gravity would not shift the centre of lensing, while DM correctly does. The observation that there are two distinct lenses surrounding the galaxies is not a prediction of MOG and therefore a strong sign that it cannot fully replace dark matter. To conclude, we are interested in DM for its extraordinary ability to explain a wide array of observed phenomena in cosmology using a simple concept. In the next section we will be discussing what DM may be in particular.

1.3 Particle Dark Matter

After realising dark matter plays an outsized role in modern cosmology, the question naturally arises as to what it is exactly. There are broadly speaking, two types of DM, astrophysical candidates and particle candidates. The astrophysical case consists of macroscopic or otherwise non-particle objects. These can comprise ordinary baryonic matter, but not necessarily. Potential candidates include faint ordinary baryonic objects like brown dwarfs or Jupiter-like gas giants, and prominently black holes [19]. These objects are examples of MACHOs, standing for *massive astrophysical compact halo objects* [20]. In particular, black holes serve as prospective candidates as they fulfil the important condition of having little to no interactions with electromagnetism and are non-luminous, at least when they are accretion-less and we neglect the faint Hawking radiation. Of particular interest are primordial black holes or PBHs. These can form, among other mechanisms, from inflationary perturbations, and are therefore well motivated. Though observations have shown that, for most PBH masses, PBHs cannot account for all the DM and, if they exist, can constitute only a tiny fraction of it [21]. Additionally, MACHOs in general were found to be unable to account for all of the dark matter, at least in the Milky Way [7, 22]. One PBH windows, however, remains open, which will be pointed out later.

A natural assumption for dark matter is that it consists of *particles*, analogously to baryonic matter. These particles could be either elementary or composite. They must have mass and can only interact with the Standard Model (SM) weakly [6]. These conditions are very permissive and open up a wide a array of models that are able to fulfil them. Indeed, a dark matter particle might not interact with the SM at all. Such DM would be undetectable with current technology and would require advances in the detection of small gravitational forces [23]. Therefore, under the assumption that some weak SM-DM interactions occur, a complete model should also be able to explain the relic abundance of dark matter particles in the universe, i.e. their primordial creation. For this, there are two prominent scenarios, *freeze-out* and *freeze-in* [6]. In the first scenario, after the Big Bang in the early hot universe, dark matter exists and is in thermal equilibrium with the SM. When the temperature of the universe decrease due to its expansion, so too does the DM abundance. If the interaction rates of DM and SM particles then become of the order of the Hubble rate, DM falls out of thermal equilibrium. Subsequently, its self-annihilation also mostly stops due to the decreased density and its abundance will *freeze-out.* In the second scenario, initially there is no DM after the Big Bang and the DM particles are not in thermal equilibrium with the SM because of extremely weak interactions. Hence there is a net creation through SM particles and thermal production. This continues until the universe cooled sufficiently, never reaching thermal equilibrium. This process is called *freeze-in* [24], as the initial DM amount is zero until the relic abundance is reached. Requiring a creation scenario in addition to the DM constraints helps to narrow the field of viable theories.

There are numerous particle dark matter theories, so it is useful to broadly classify them. Here we want to outline the types of DM particles and discuss them briefly, with some select types getting a more detailed discussion below. A very straightforward type of DM would be Standard Model particles, in particular the *neutrino.* While neutrinos appear at first as promising DM candidates, their abundance and their relativistic velocities make them incapable of explaining the observed structure of the universe [25, 26]. There are also the hypothetical right-handed *sterile neutrinos* as potential "SM-adjacent" DM candidates [6]. An important class of beyond the Standard Model (BSM) particles are referred to as *WIMPs*, short for Weakly Interacting Massive Particles [6]. These WIMPs have large masses, i.e. in the GeV to TeV range, and interact with the SM only weakly. The initial motivation for these came from cosmology, later reinforced by supersymmetry, and will be discussed later in more detail. On the other end of the mass spectrum there are *axions* and *axion-like particles* (ALP) [6]. These have sub-eV masses and initially arose out of solving the strong CP problem of QCD. We will discuss them in more detail as well. Another common type of dark matter are *dark photon* mediated theories [28]. Here, instead of having the dark sector interact with the SM in a direct way, we introduce a new type of force between them, mediated by new particle called a dark photon. Naturally, there are numerous additional models and theories that are allowed by the dark matter constraints, so this was not an exhaustive listing.

1.3.1 Sterile Neutrinos

Ordinary neutrinos were once thought to be prime dark matter candidates. Even with them being massless, the weakly interacting and numerous particles seemed to provide a natural explanation for DM with known physics. They constitute a type of DM called hot dark matter, comprised of relativistic particles with high velocity dispersion. Later, however, it was shown through further study that hot dark matter cannot explain the observed large scale structure of the universe [25, 26]. After the discovery of neutrino oscillation [29] and with it, the insight that neutrinos must have mass, the existence of sterile, i.e. right-handed, neutrinos is implied by the dynamic mixing of chirality [27]. The mass of these particles depends on their exact nature. A typical treatment of sterile neutrinos is to assume that they have a Majorana mass term, in addition to the Dirac mass term that leads to active-sterile mixing. Diagonalising these terms gives rise to the mass of the ordinary neutrinos through the so-called see-saw mechanism [6, 27]. The details of how this mechanism works are not too important for the discussion here. The somewhat "natural" appearance of these particles and their properties make them appealing dark matter candidates.

1.3.2 WIMPs and Supersymmetry

Probably the most well-researched category of dark matter are the Weakly Interacting Massive Particles, or WIMPs. Their name comes from their characteristics of having large masses, compared to baryons, as well as participating in weak interactions [6] or interactions reminiscent of them. The reason they are so prominent is that the original WIMP arose from the requirements on the production of dark matter in the early universe, leading to the current relic density. This is called the *WIMP miracle* [5]. During the early stages after the Big Bang, when the universe was still hot and dense, dark matter particles would get created and annihilated in thermal equilibrium with the primordial plasma. To describe the evolution of the DM abundance, it is necessary solve the Boltzmann equation for the DM number density n, with the equilibrium density n_{eq} and the thermally averaged annihilation cross section of DM $\langle \sigma v \rangle$ [5]

$$\frac{d(na^3)}{dt} = -\left(n^2 - n_{\text{eq}}^2\right) a^3 \langle \sigma v \rangle,$$

where a is the universe's scale factor. If one now assumes the interactions described by $\langle \sigma v \rangle$ become significant at high temperatures, n equals its equilibrium value n_{eq} at very early times. As the equilibrium density drops with the temperature of the primordial plasma, at some point the DM falls out of thermal equilibrium and a relic density remains. Hence this describes a freeze-out scenario. One needs to solve for the relic abundance of DM using the Boltzmann equation in order to compare it to measurements. From this, for a particle with electroweak interactions,

$$\Omega_{\mathrm{DM}} h^2 \approx \frac{10^{-37}\,\mathrm{cm}^3/\mathrm{s}}{\langle \sigma v \rangle}$$

is obtained [6], where $\Omega_{\mathrm{DM}} h^2$ is the density parameter of dark matter normalised to the dimensionless Hubble parameter h with a measured value of $\Omega_{\mathrm{DM}} h^2 \approx 0.12$ [13]. This means that the thermally averaged annihilation cross section $\langle \sigma v \rangle$ needs to be around 1 pb, corresponding to weakly interacting particles with masses of order 100 GeV. This is the so-called WIMP miracle referred to earlier.

After discussing the motivation for the class of WIMPs, it is natural to ask what candidate particles could fit into this category. While one can postulate a theory of a WIMP by just introducing it by hand, they can also appear in some more encompassing models. This is, for instance, the case for the WIMP candidates arising naturally out of supersymmetry (SUSY) [6]. SUSY is a new symmetry of nature between fermion and bosons. In supersymmetric extensions of the Standard Model, there exists a lightest stable supersymmetric particle (LSP) [30]. This is due to R-parity conservation. Therefore, if such an LSP is massive, it is an ideal DM candidate, assuming it is uncharged and interacts only weakly. SUSY WIMPs were long considered to be the most promising dark matter candidates, especially considering their appearance in supersymmetric extensions of the SM. Of course, numerous other non-SUSY WIMP models also exist.

1.3.3 Axions and ALPs

On the lower end of the mass spectrum are *axions*. The axion [31, 32] is a light pseudoscalar neutral particle arising from a solution to the strong CP problem in quantum chromodynamics (QCD). To briefly outline, according to Gell-Mann's totalitarian principle, one must include all terms in the Lagrangian describing that are not forbidden by symmetries of the system [27]. In particular, for QCD this means it is necessary to include a CP violating kinetic term for the gluon field in addition to the ordinary one, as well as a complex mass term for the quarks. To illustrate this, let us look at the QCD Lagrangian with massive quarks and CP-violating terms [6, 27]

$$\mathcal{L}_{\mathrm{QCD}} = -\frac{1}{4} G_{\mu\nu} G^{\mu\nu} + \frac{\theta g^2}{32\pi^2} G_{\mu\nu} \tilde{G}^{\mu\nu} + \bar{\psi}(i\not{D} - M)\psi,$$

where $G_{\mu\nu}$ is the field strength tensor of the SU(3) gauge field, the gluon field, $\tilde{G}^{\mu\nu} = \varepsilon^{\mu\nu\alpha\beta} G_{\alpha\beta}/2$ its dual, g is the charge of the quark under SU(3), θ is a new angle parameter related to the degree of CP-violation, while ψ are the quark fields, $\not{D}$ the covariant derivative and M is the complex mass parameter having some angular argument, also leading to CP violation. The summation over the colour and flavour indices in the Lagrangian is left implicit. While it is possible to use a chiral transformation to remove either of the two angles described above, one of them remains. Removing both would be possible, if at least one quark was massless, but since the chiral symmetry of the SM is anomalous [27], nothing protects the quarks from acquiring mass. It is customary for QCD to make the mass real and keep the θ term. As this term involves $G_{\mu\nu}\tilde{G}^{\mu\nu}$, a total derivative, in the Lagrangian, it only contributes to non-perturbative effects. Specifically, this term leads to a neutron electric dipole moment proportional to θ. Therefore, the measurement of such a dipole moment directly quantifies the CP violation of the strong force. Considering CP is not protected by any symmetry of the Standard Model, but rather violated by the weak force, it would be expected for the θ term to be of order $\mathcal{O}(1)$, as nothing within the SM would force θ to be small or zero [27]. But, as it turns out, the measured value of θ is exceedingly small at less than 10^{-10} [27]. This apparent fine-tuning of θ is referred to as the *strong CP problem.* Incidentally, this also occurs for the other forces of the SM, but can be completely removed for the weak force due to it only coupling to left-handed fermions and for the electromagnetic force due to the existence of neutral fermions, specifically neutrinos, in the SM [27].

One way to resolve the strong CP-problem is to introduce some mechanism which dynamically forces θ to vanish. A method to achieve this is the Peccei-Quinn mechanism [33, 34]. Here, a new global anomalous $\mathrm{U}(1)_{\mathrm{PQ}}$ symmetry, meaning a symmetry of the classical but not of the quantum theory, is introduced to the SM. This new symmetry is then spontaneously broken and generates a pseudo-Goldstone boson a. This new pseudoscalar particle is called *axion* [31, 32]. Due to the symmetry being anomalous, a term proportional to $aG_{\mu\nu}\tilde{G}^{\mu\nu}$ is generated. Consequently, this allows for the combination of the axion with the θ term above, in effect promoting it into a field. The axions then become excitations around the θ vacuum, dynamically relaxing the minimum of its potential $V(\theta)$ at $\theta = 0$ and thus solving the strong CP problem [35]. Interactions between the axion and the SM would also be very weak. This makes the axion a dark matter candidate. Today we know that the mass of this new particle would have to be small, in the 10^{-3} eV to 10^{-6} eV range [6]. Additionally, there can be dark matter models that are similar to axions, but do not arise from the strong CP problem, nor solve it. These are called ALPs, or *axion like particles*, with relaxed conditions on mass and coupling strength.

1.4 Dark Matter Detection

Regardless of what exact theory is used as a dark matter model, DM particles have to be detected in order to confirm their existence. While there is extensive evidence from cosmology, in the form of the CMB and large scale structure formation, one can only claim dark matter to be the correct theory after confirming it by observation. This section will focus on three main methods of trying to detect particle DM, by outlining the general methods and then look closer at particular set-ups and experiments. While the purpose of most dark matter searches is to find a dark matter candidate, in actuality they primarily constrain the vast parameter space of theories. The constraints placed by experiments depend on the DM model. For instance, in a WIMP theory, where the weak force already determines the interaction strength, DM experiments constrain the mass of the WIMPs. However, in a model with multiple input parameters such as mass, coupling strength, etc., one experiment often can only constrain combinations of them. Therefore, a variety of approaches to detection is needed. In the following paragraphs, we will broadly outline the source and detection of DM. Naturally, these categories are broad characterisations and there can be overlap between different methods.

In addition to the different experimental methods, there is also the question of the source of the particles to be detected. The most straightforward way is to observe the naturally occurring dark matter in the Solar System. The local mass density of DM in our region of the Milky Way is determined to be in the range of 0.3–0.6 $\mathrm{GeV\,cm^{-3}}$ [36]. How this translates to particle density is, of course, completely dependent on the mass of the particle in a given model. For example, a WIMP with a mass of a 100 GeV has a particle density of approximately $10^{-3}\,\mathrm{cm^{-3}}$. In order to measure DM, it is necessary to know its flux in a detector. The velocity of DM in our part of the Galaxy is typically 230 km/s [36]. This velocity, combined with the model-dependent number density, gives the natural dark matter flux that can be detected. Besides this, it is also possible to try to produce dark matter particles artificially, using accelerators and colliders to generate DM.

First, we will discuss a staple of particle physics, *accelerator/collider* experiments. Here, dark matter is generated by collisions in situ and subsequently detected, analogously to how, for instance, the Higgs boson was discovered. This approach can utilise all the sophisticated methods of particle detection already deployed in colliders. For example, dark matter was and is searched for at the LHC, most commonly in form of SUSY particles [6]. The discovery of these would have automatically yielded a good

DM candidate, although as of 2024 no SUSY particles have been detected [37]. Regardless, the results of measurements at colliders are still useful in constraining the parameter space of DM. A way to accomplish this is missing energy in Standard Model decays, like the Z-boson [6]. Unaccounted energy/momentum, without a viable SM explanation, constrains possible BSM models. Most of the methods using colliders are indirect, meaning they look for signatures left behind by the creation or annihilation of dark matter particles. It is, however, also possible to use the accelerators only as a production facility and try to detect the produced DM directly, such as in in some dedicated, so-called, intensity frontier experiments.

The accelerator/collider experiments belong to the broader class of dark matter *indirect detection*. The current evidence for dark matter is all indirect, hence such methods are very useful in constraining parameters, but are not sufficient to show the existence of particle dark matter conclusively. Nonetheless, indirect measurements of the consequences of different dark matter models are crucial in getting a handle on the vast number of possible theories. One type of indirect constraints comes from high-precision particle physics. Any dark matter particle with SM interactions will imprint itself in such measurements, constraining models by limiting how much impact they are allowed to have on the SM. The observables of this type include, for instance, the anomalous magnetic moments of leptons [6]. Another important indirect way of determining DM properties is the CMB. The structure of its anomalies puts constraints on how dark matter can interact with baryons in the early universe. The most recent measurement the CMB was conducted in 2018 by Planck [13]. The observations that are most commonly associated with indirect detection, are from astrophysical sources. There are a variety of signatures that can arise from model-dependent processes of DM interactions, most commonly their annihilation in the case of symmetric DM. A typically expected signal is gamma radiation emitted from pair annihilation in high density DM regions like galactic centres [6], especially of the Milky Way. Experiments looking for such signals are, prominently, space telescopes and ground-based Cherenkov telescopes. Depending on the exact annihilation process and which particles are produced, the composition of cosmic rays might also be influenced [6]. A closer source of indirect DM signals could be our sun, as it may accumulate a higher concentration of DM in its centre due to model-dependent collisions of DM with its baryonic matter. While this would happen for all dense objects, the sun being the densest in the solar system would lead to it experiencing the most DM accumulation. A possible method is using solar neutrinos, as DM annihilation in the sun's core could potentially result in an excess of high energy neutrinos not expected from ordinary solar processes [6].

The most definitive way to find particle dark matter is *direct detection*. As the name implies, such methods try to directly determine the energy deposited by a dark matter particle into a detector [6]. This energy can then be measured and compared to expected values for specific dark matter models. Depending on the mass and coupling of a DM particle, the main modes of energy transfer include nuclear and electron scattering as well as condensed matter effects like phonons. The way this is measured depends on the detector material and the amount of energy that is typically expected to be transferred to this material. A common type of direct detection experiment is a bulk detector, usually made from a scintillator [6]. This is in principle similar to a typical neutrino detector, like Super-Kamiokande, which also uses a large amount of a substance, in this case water, to facilitate rare interactions and subsequently observe them. Another important aspect for bulk detectors is the mass of the nuclei that make them up, especially in order to detect very heavy DM like WIMPs, as the interaction cross section grows with nuclear mass [6]. The detector can use either a solid or liquid material and employs scintillation and ionisation, typically in conjunction with photomultipliers, to detect DM scattering. An example for a typical liquid scintillator is xenon, for instance, used in the experiment XENONnT at the Gran Sasso underground laboratory [38]. Solid crystal scintillators are often tungsten compounds due to its high nuclear mass. These are commonly used in cryogenic detectors, where superconducting sensors are held right at the critical temperature and, when even a small amount of energy is deposited into it, the resulting heating will lead to the measurable loss of superconductivity. An experiment of this type is CRESST at Gran Sasso [39]. Such solid-state detectors can also exploit condensed matter effects, like phonons and plasmons, potentially leading to higher energy sensitivity. Some experiments can also be purpose-built to probe a specific model that predicts a unique interaction. An example for this are axion models, which all include an interaction term of a single axion converting into two photons, and vice versa, in the presence of a strong magnetic field [6, 35]. ADMX is an example of this [40]. While bulk detectors are well suited to heavy DM and can, especially cryogenic experiments, also probe lighter particles, low mass (sub-GeV) DM is still less explored than high mass models [41].

A newer type of detector, made technologically possible only recently [42], are semiconductors, in particular charge-coupled devices (CCDs). CCDs are a type of sensor that principally use the photoelectric effect to measure the charge liberated by photons incident on it. Due the nature of the CCD, however, any energy deposition that can lead to ionisation in the sensor, can be detected. This includes alpha and beta radiation, as well as dark matter particles, not just photons. Using sophisticated methods to achieve single-charge precision, energy thresholds can be lowered to a few eV [42]. Examples of such an experiments are SENSEI [43] and DAMIC [44] at the Sudbury underground laboratory. In this work we will focus on computing event rates for such a CCD detector, with its functioning explained in more details later. Of course, the list of examples and methods presented here is incomplete. There is no end to interesting ideas and people still come up with new concepts to further our understanding of DM.

In order to actually constrain the vast dark matter parameter space, it is necessary to compute cross sections of the processes relevant for the phenomena observed in astrophysics or in a detector. This allows for the prediction of the expected results of observations for different dark matter parameters, which can then be compared to measurements. In summary, one states a model, calculates cross sections of relevant interactions and computes theoretical event rates for a detector. The corresponding measurements are then taken and compared to the expected theory values for different parameters. Non-detection of such expected events will exclude a range of model parameters. All this means is, that in the absence of a direct observation of a dark matter particle interaction, we primarily try to narrow down the vast space of theoretically possible models.

1.5 Dark Matter Current State

Before discussing the particulars of this work, it is instructive to quickly review the current state of dark matter searches in 2024. To put a perspective on non-particle dark matter, we briefly look at the state of primordial black holes as dark matter. In general, the range of mass where PHBs can make up a significant portion of dark matter has been highly constrained, as can be seen in Fig. 3. Even if PBHs were created during inflation, it has become increasingly unlikely that they constitute the majority of dark matter in the universe [21]. Notable in Fig. 3 is the one mass windows, where PBHs are still able to account for the total dark matter mass. This PBH mass range is asteroid-like from about 10^{17} g, below which PBHs would evaporate too quickly due to Hawking radiation, to about 10^{23} g. These are black holes of exceptionally small size. Their radii, under the simplified assumption that they are Schwarzschild, range from about 100 pm, comparable to the size of atoms, to 100 μm. Another apparent window is in the $10^{14}\,\mathrm{M}_\odot$ to $10^{17}\,\mathrm{M}_\odot$ mass range. These would be enormous objects, beyond even the heaviest supermassive black holes known. These could potentially still account for a significant portion of DM, but fail to explain the galactic halo level due to their sheer mass and size, so cannot make up the total DM amount in the universe. While it is difficult to imagine such objects being able to form, the main reason these are less constrained is likely due to the lack of attention given to them [21].

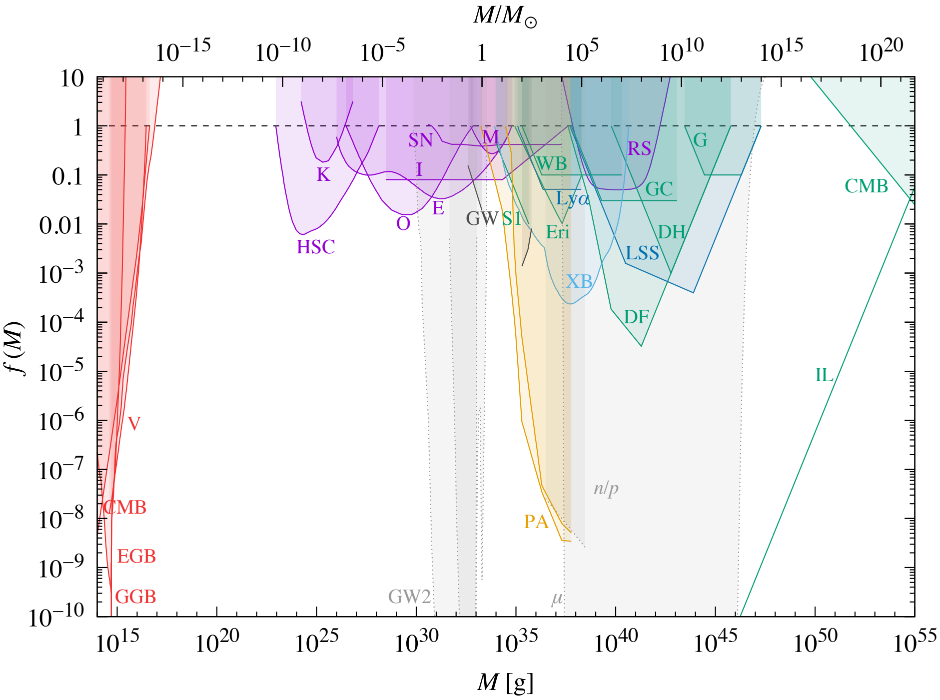

Figure 3: PBH dark matter constraints. The dark matter fraction $f(M)$ that PBHs can make up is shown in relation to their mass in grams and solar masses $M_{\odot}$. For a more detailed explanation of the limits, refer to [21].

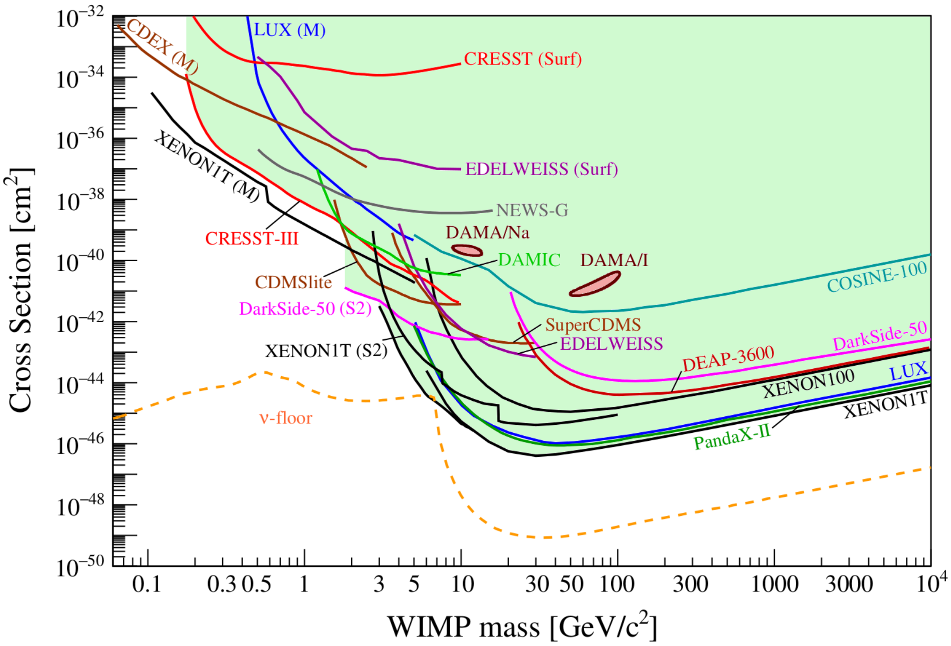

Figure 4: The constraints for a standard WIMP scenario in a isothermal dark matter halo. The spin-independent WIMP-nucleus cross section is plotted against the WIMP mass. The shaded region is excluded by the named experiments. For a more detailed explanation of the limits and the used standard parameters, refer to [45].

One of the most well studied dark matter paradigms are WIMPs, hence they have the best probed parameter space [45]. The allowed mass of a heavy supersymmetric WIMP interacting via the weak nuclear force is already quite constrained, as can be seen in Fig. 4, even gradually approaching the neutrino floor, where the solar neutrino background will inhibit, or at least greatly interfere with, their detection. While this limit is certainly not insurmountable, it will make direct detection experiments in the affected mass range more challenging. One can also observe that at the lower end of the mass range, there is a significant increase in the upper bound of the cross section. This is mainly due to the difficulty of probing lower mass WIMPs using existing detectors [45]. Xenon experiments are starting to probe this range, due to their energy threshold being low enough. A newer type of experiment, CCD sensors, are also starting to push to the lower mass end of WIMPs [43, 46].

As aforementioned, a type of low mass DM are axions and ALPs, as can be seen in Fig. 5. Much of the parameter space of axions and ALPs is still unconstrained [45], despite their theoretical basis being decades old [31]. This is in large parts due to the difficulty in detecting interactions of these light particles. Recently, technology has improved such as to make it possible to further the research of axions and ALPs, and new detectors are being built and designed [45]. As evident from Fig. 5, high mass axions would largely be in tension with astrophysical constraints. Importantly tough, the small mass range has sufficient unexplored space to still allow for axion DM.

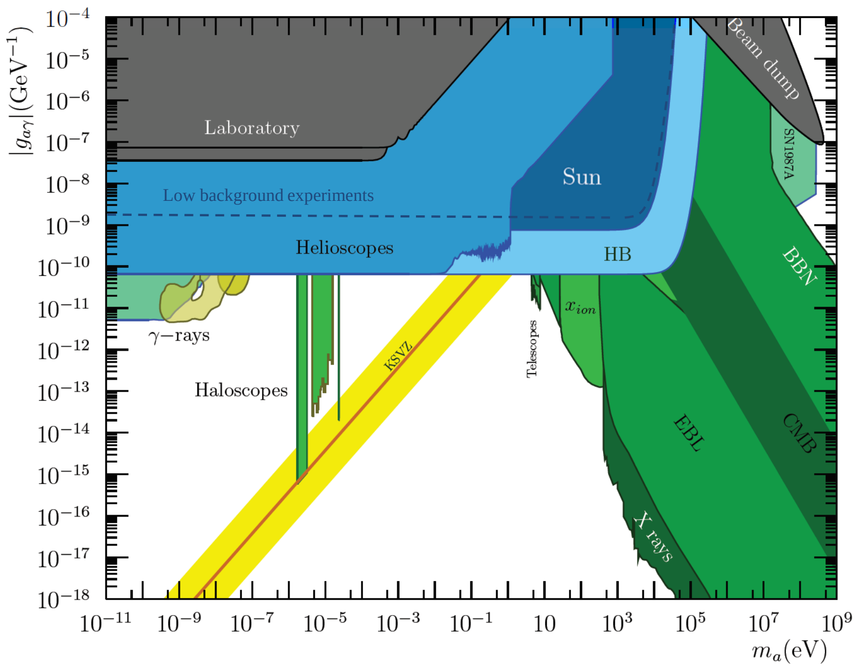

Figure 5: Axion constraints from astrophysics/cosmology and experiments. The magnitude of the axion-photon coupling is on the vertical axes, while the axion mass is on the horizontal axis. For an explanation of the constrained regions, refer to [45, 49].

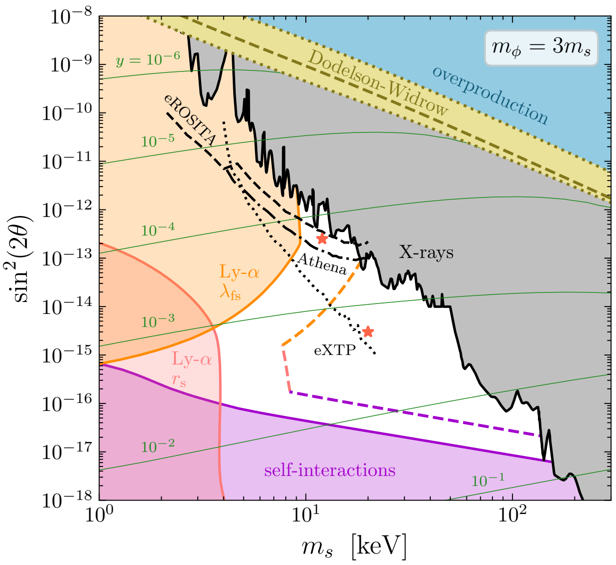

Figure 6: Sterile neutrino constraints for a minimal model with one additional sterile flavour and self-interaction through a scalar mediator. In the vertical axis, θ refers to the ratio of the sterile active mixing to the sterile mass m_s. A more thorough explanation can be obtained from [48].

Since the discovery and confirmation of neutrino oscillation [29], sterile neutrinos have been explored as dark matter candidates. A standard sterile neutrino, meaning that their only non-gravitational interaction is mixing with SM neutrinos, have already been largely excluded [47] as dark matter. But there are still alternate theories that remain viable. For example, a minimal model with self-interacting sterile neutrinos, e.g. through a scalar mediator [48], is not yet excluded. Fig. 6 shows the current status of sterile neutrinos bounds for a such a model from [48].

Another type of dark matter is the dark photon and dark photon mediated DM models [28]. We will discuss this theory in more detail later, but to explain briefly: A new U(1) symmetry, that mixes with the SM U(1), is introduced which has a corresponding gauge field resulting in a new vector boson called the dark photon. This particle couples the SM to a dark sector charged under the new U(1) and can mix with the SM photon, if it is massive, or induce a fractional electric charge in dark sector particles, called millicharge, if massless. In the massive dark photon case, the new boson itself is measured, or rather its effects on photons. The relevant parameters here are its mass and its kinetic mixing with the standard photon, as can be seen in Fig. 7. In the massless dark photon case, the new boson is only measured indirectly by trying to observe another new DM particle with an induced millicharge. The two relevant parameters in this case are the kinetic mixing, that presents itself as millicharge, and the mass of the new DM particle, as can be seen in Fig. 8.

This thesis is organised as follows. In Sec. 2 we will outline a potential production-detection set-up for an underground experiment that will serve as an exemplary way to measure the results of this work. In Sec. 3 we introduce the electromagnetic form factor dark matter model that will be studied. In Sec. 4 we compute the electron-DM and DM-DM scattering processes in that model. In Sec. 5, the production cross section of DM through electron-electron scattering will be evaluated and in Sec. 6 the events at a detector are predicted. In Sec. 7 we will review the numerical methods used to calculate the relevant integrals and Sec. 8 will discuss the detector that provides the material parameters for the prediction. In Sec. 9 we present the results, in Sec. 10 we review constraints and Sec. 11 is our conclusion.

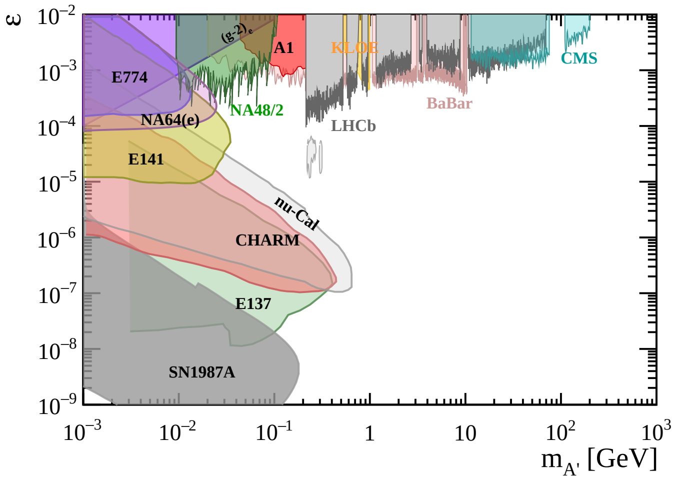

Figure 7: Constrained parameter space of a massive dark photon with kinetic mixing ε and mass $m_{A'}$ in the range from 1 MeV to 1 TeV. Detailed description in [28].

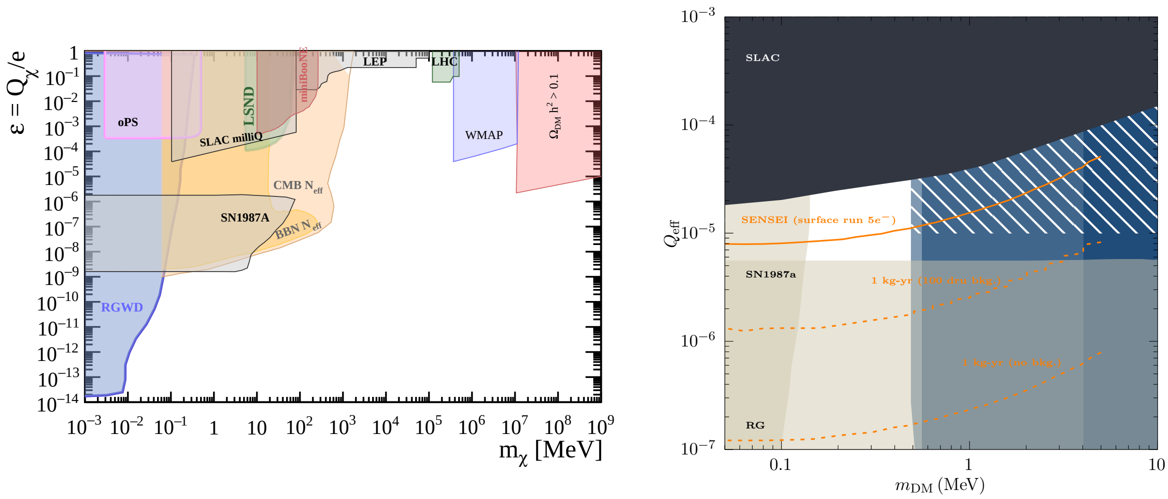

Figure 8: The left figure from [28] shows millicharge ε constraints over a wide array of DM fermion mass m_χ. The right figure from [50] also shows those constraints but zoomed into an experimental window that is still unprobed directly. The difference between the two figures comes from the left one's inclusion of model dependent and indirect BBN effective degrees of freedom constraints.

2 Light Dark Matter Direct Detection from Accelerators

Now that we have sufficiently motivated dark matter and outlined its importance and current state, we can begin to discuss the particular goal of this thesis. *Light sub-GeV dark matter* has been of particular interest in the past decade, due to its relatively un-probed parameter space. A major issue with direct detection of lighter dark matter is its, compared to electroweak mass WIMPs, low kinetic energy when naturally occurring. To illustrate, in our local region of the Galactic halo, a DM particle of mass 1 MeV has only a few eV kinetic energy due to being non-relativistic at about 230 km/s [36]. This issue can be addressed in two ways, namely decreasing the detection energy thresholds or somehow making use of dark matter particles with higher kinetic energy. With DM that is gravitationally bound to the Galaxy, it is only really feasible to increase detector sensitivity to probe ever lower energy transfer. A way to address the second possibility, ideally in tandem with improvements in detection technology, is to impart DM particles with more kinetic energy. In order to achieve this, one can try to produce dark matter particles in such a way that they have high kinetic energy. This can make it possible to detect small mass DM particles by making them *ultra-relativistic*.

Naturally, it is necessary to facilitate some process that creates the dark matter particles. A standard method to achieve this is some type of accelerator or collider. In our case, we will focus on a *linear electron accelerator* that deposits its energy into a *beam dump*. The deposited electrons will interact with targets in the beam dump and produce DM particles in accordance with a particular model. Downstream from the the beam dump and in the beam line, a detector can be placed to observe the produced, ideally relativistic, DM flux. In order for such a detector to reasonably observe the produced DM, it is crucial to exclude other particles that would mask a dark state signal. For the desired signal not to be drowned out by the particle shower produced in the beam dump, a screen in the beam line shielding the detector is needed. This should ensure that predominantly weakly interacting particles, like DM, penetrate through to the detector. Additionally, other background radiation should be reduced as much as possible. A straightforward way to shield an experiment from background radiation is putting it deep underground, usually below high mountains. This automatically prevents cosmic or atmospheric interference due to the sheer amount of matter stopping virtually all external radiation. Remaining sources of radioactivity from the rock can be mitigated by air scrubbing and additional shielding of the experiment using materials with low levels of radiation. The thermal dark current can be reduced by cooling the detector to cryogenic temperatures. Neutrinos, predominantly solar neutrinos, constitute the biggest background that cannot be mitigated by shielding. In short, a potential accelerator-detector set-up should be placed in an *underground laboratory*, as is typical of dark matter experiments.

The advantage of this approach is that the detection of *light dark states* is enabled, as well as tunability of the input energy in addition to the decrease in necessary observation time. A big disadvantage is, of course, the needed electric power, which could be quite significant, and the additional cost of an accelerator set-up. Furthermore, the computational complexity of calculating both the production and the detection of the modelled DM particle can be much greater than for simpler bulk experiments using only naturally occurring DM. This is especially true for the production part that determines the flux onto the detector. Under the assumption that the dark matter model, as an extension to the Standard Model, does not lead to a violation of baryon or lepton number conservation, the minimal process for DM production from electron-electron or electron-nucleus scattering is a 2-to-3 process for bosonic DM and a 2-to-4 process for fermionic DM.

In conclusion, for our calculation of the production, we are interested in the *energy* and *angle* to the beam line of the produced dark matter particles, in order to determine the incoming energy onto the detection. In the detection part, the relevant parameter is the *recoil energy* of the targets inside the detector, which directly corresponds to the energy deposited by the DM. The only relevant kinematic parameters for the total production-detection process are the masses of the electrons and the DM particles and, importantly, the energy we put into the system in the form of the projectile's momentum, in our case electrons. Using these parameters, we will compute a prediction of the expected events in the detector. A schematic sketch of the described set-up can be seen in Fig. 9. In the following chapter a specific model will be used, described in greater detail below, to compute the cross section of the individual processes and then apply them to an experiment that could potentially be used to implement this work.

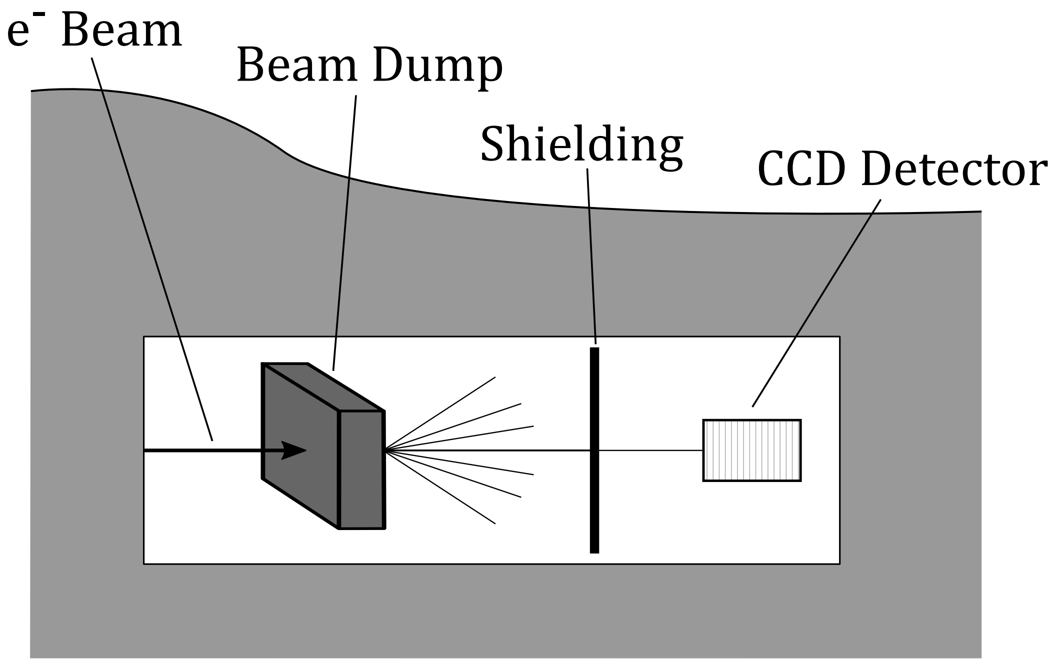

Figure 9: Schematic set-up diagram in an underground laboratory. A linear accelerator fires a pulse of electrons onto a beam dump. There, 2-to-4 inelastic scattering produces DM particles pairs that will be emitted favourably in the direction of the beam line, especially if they are relativistic. The created DM flux onto the detector then facilitates the detection of the produced dark matter.

3 Dark Matter with Electromagnetic Form Factor Interactions

3.1 Effective Model of the Electromagnetic Form Factors

In this work, we will specifically investigate a new light fermionic particle χ with mass m_χ and a proposed millicharge or electromagnetic form factor couplings [51]. Millicharge refers to a fractional electric charge that can arise from dark photon models. Electromagnetic form factors are the low energy Wilson coefficients of an effective field theory (EFT). Exemplary UV-complete models for these interactions will be briefly outlined later. These light states can then be dark matter candidates, although strictly they, do not need to be. Our interest in them is, of course, primarily motivated by their possibility to constitute DM. The Lagrangians for the model mentioned are:

millicharge (εe): $$\mathcal{L}_{\varepsilon e} = \varepsilon e\, \bar{\chi}\gamma^\mu \chi A_\mu, \tag{1a}$$

magnetic dipole moment - MDM (μ_χ): $$\mathcal{L}_{\text{MDM}} = \frac{1}{2}\mu_\chi\, \bar{\chi}\sigma^{\mu\nu}\chi F_{\mu\nu}, \tag{1b}$$

electric dipole moment - EDM (d_χ): $$\mathcal{L}_{\text{EDM}} = \frac{i}{2} d_\chi\, \bar{\chi}\sigma^{\mu\nu}\gamma^5\chi F_{\mu\nu}, \tag{1c}$$

anapole moment - AM (a_χ): $$\mathcal{L}_{\text{AM}} = -\, a_\chi\, \bar{\chi}\gamma^\mu\gamma^5\chi\partial^\nu F_{\mu\nu}, \tag{1d}$$

charge radius - CR (b_χ): $$\mathcal{L}_{\text{CR}} = b_\chi\, \bar{\chi}\gamma^\mu\chi\partial^\nu F_{\mu\nu}, \tag{1e}$$

where $F_{\mu\nu} = \partial_\mu A_\nu - \partial_\nu A_\mu$ is the usual electromagnetic field strength tensor, $\sigma^{\mu\nu} = \frac{i}{2}[\gamma^\mu, \gamma^\nu]$ and the fifth gamma matrix is $\gamma^5 = i\gamma^0\gamma^1\gamma^2\gamma^3$. Furthermore, e is the elementary charge, μ_χ and d_χ are the magnetic (MDM) and electric (EDM) dipole moment of the new particle χ, respectively. The factor a_χ is called anapole moment (AM) and b_χ is the charge radius (CR). These couplings are all real-valued. The mass dimension of the operators are: 4 for millicharge, 5 for MDM & EDM and 6 for AM & CR. This means that there are negative mass couplings for the interactions with mass dimension greater than four, namely $[\mu_\chi], [d_\chi] = -1$ and $[a_\chi], [b_\chi] = -2$, as expected for effective interactions. It is not necessary for χ to have an electric charge in order to have higher order EM form factors. These can arise, e.g. from loops in some UV-complete theory, or from χ being a composite particle. Millicharge is not an effective coupling, but instead is identical to quantum electrodynamics with a diminished charge. All calculations are done using the mostly minus $(+, -, -, -)$ using convention for the Minkowski metric.

In addition to the mass dimension 5 and 6 interactions (1b-1e), there are also mass dimension 7, so-called, Rayleigh or susceptibility interactions [52]:

scalar Rayleigh interaction - SR (r_χ): $$\mathcal{L}_{Rs} = \frac{1}{4} r_\chi\, \bar{\chi}\chi F_{\mu\nu}F^{\mu\nu}, \tag{2a}$$

pseudoscalar Rayleigh interaction - PR ($\tilde{r}_\chi$): $$\mathcal{L}_{Rp} = \frac{i}{4}\tilde{r}_\chi\, \bar{\chi}\gamma^5\chi F_{\mu\nu}\tilde{F}^{\mu\nu}, \tag{2b}$$

where $\tilde{F}_{\mu\nu} = \frac{1}{2}\varepsilon^{\mu\nu\rho\sigma}F_{\rho\sigma}$ is the dual EM field strength with the Levi-Civita symbol $\varepsilon^{\mu\nu\rho\sigma}$ and $\varepsilon^{0123} = 1$. Here r_χ and $\tilde{r}_\chi$ are the coupling strengths of mass dimension -3 for the scalar and pseudoscalar Rayleigh interactions, respectively. The name *Rayleigh* stems from the fact, that these interactions have two fermions and two photons at their vertex, akin to Rayleigh scattering. The label *susceptibility* comes from the relation of the coupling r_χ with the electric susceptibility χ_e. All the mentioned effective couplings are valid as long as the centre of mass (CM) energy of the interaction is sufficiently below the scale at which they are generated by some EFT.

Next, we want to derive Feynman rules for the interactions (1) and (2). This can be done by following a standard procedure. First, one takes the Lagrangian of the interaction and multiplies it by the imaginary unit i. Then the derivatives are replaced with $\partial_\mu \to -ip_\mu$, where p_μ is the momentum of the derived field, here following the convention of Schwartz [27]. Finally, one must sum over all permutations of the indices of indistinguishable momenta. Then the external fields are stripped away. This derivation can also be achieved more rigorously by using path integrals, which is done in App. (A). This leads to the following vertex functions Γ for the form factor interactions:

$$\begin{aligned}
\varepsilon e: &\qquad i\Gamma^\mu_\varepsilon(q) = i\varepsilon e\gamma^\mu, &\text{(3a)}\\
\text{MDM}: &\qquad i\Gamma^\mu_\text{M}(q) = -\mu_\chi\sigma^{\mu\nu}q_\nu, &\text{(3b)}\\
\text{EDM}: &\qquad i\Gamma^\mu_\text{E}(q) = -id_\chi\sigma^{\mu\nu}\gamma^5 q_\nu, &\text{(3c)}\\
\text{AM}: &\qquad i\Gamma^\mu_\text{A}(q) = -ia_\chi(q^2\gamma^\mu - q^\mu \not{q})\gamma^5, &\text{(3d)}\\
\text{CR}: &\qquad i\Gamma^\mu_\text{C}(q) = ib_\chi(q^2\gamma^\mu - q^\mu \not{q}), &\text{(3e)}\\
\text{SR}: &\qquad i\Gamma^{\mu\nu}_{Rs}(q_1,q_2) = ir_\chi(q_2^\mu q_1^\nu - q_1\cdot q_2\eta^{\mu\nu}), &\text{(3f)}\\
\text{PR}: &\qquad i\Gamma^{\mu\nu}_{Rp}(q_1,q_2) = -\tilde{r}_\chi\gamma^5\varepsilon^{\mu\nu\sigma\rho}q_{1\sigma}q_{2\rho}, &\text{(3g)}
\end{aligned}$$

where the q refers to the momentum of the photon at the vertex and q_1, q_2 to the momenta of the two photons at the Rayleigh vertices. Expectedly, (3a) is just the normal QED fermion-photon vertex with a modified charge, hence the name millicharge. Interestingly, all of the effective operators considered here include derivatives, meaning the electromagnetic form factor interactions (3b-3g) are all dependent on the momentum of the photon(s) at the vertex. Furthermore, the pairs MDM-EDM and AM-CR are just differentiated by a fifth gamma matrix γ^5. As a result of this, in the low mass limit, each of these pairs will converge into a single interaction, effectively making the γ^5 redundant for the low mass case, as will be shown later. We can also see that the vertex functions for AM (3d) and CR (3e) are of the same form as the photon two point Green's function in Feynman gauge. Due to this, AM and CR interactions are not present for on-shell photons, as these are the free Green's function solutions, which that vanish. To make this more explicit, one can take the $(q^2\gamma^\mu - q^\mu\not{q})$ part, set the photon on-shell by contracting it with a polarisation vector ε^μ, and notice that for on-shell photons $q^2 = 0$ as well as $\varepsilon^\mu p_\mu = 0$, hence $(q^2\gamma^\mu - q^\mu\not{q})\varepsilon_\mu = 0$.

It is also interesting to investigate the CPT behaviour of these interactions, following Schwartz [27] and Peskin-Schroeder [53]. The CPT operators acting on a spinor ψ are

$$\begin{aligned}
\text{Charge conjugation:}\quad & C:\psi\mapsto -i\gamma^2\psi^*,\ C\gamma^\mu = (\gamma^\mu)^T C,\ C\gamma^5 = \gamma^5 C,\ C^2 = \mathbb{1}\\
\text{Parity transformation:}\quad & P:\psi\mapsto \gamma^0\psi,\ P\gamma^\mu = (\gamma^\mu)^\dagger P,\ P\gamma^5 = -\gamma^5 P,\ P^2 = \mathbb{1}\\
\text{Time reversal:}\quad & T:\psi\mapsto \gamma^1\gamma^3\psi,\ T\gamma^5 = \gamma^5 T,\ T^2 = \mathbb{1}.
\end{aligned} \tag{4}$$

From this, the general transformation under charge conjugation is $C\bar{\psi}\Gamma\psi C^\dagger = -\bar{\psi}\gamma^2\gamma^0\Gamma^T\gamma^0\gamma^2\psi$ for a vertex function Γ. The behaviour of Dirac bilinears and vectors is displayed in Tab. 1, with $(-1)^\mu = \{1 \text{ for } \mu = 0, -1 \text{ for } \mu = 1,2,3\}$ [53]:

Table 1: CPT behaviour of Dirac bilinears, the partial derivative and the four potential.

	$\bar\psi\psi$	$i\bar\psi\gamma^5\psi$	$\bar\psi\gamma^\mu\psi$	$\bar\psi\gamma^\mu\gamma^5\psi$	$\bar\psi\sigma^{\mu\nu}\psi$	$i\bar\psi\sigma^{\mu\nu}\gamma^5\psi$	∂_μ	A^μ
P	$+1$	-1	$(-1)^\mu$	$-(-1)^\mu$	$(-1)^\mu(-1)^\nu$	$-(-1)^\mu(-1)^\nu$	$(-1)^\mu$	$(-1)^\mu$
T	$+1$	-1	$(-1)^\mu$	$(-1)^\mu$	$-(-1)^\mu(-1)^\nu$	$(-1)^\mu(-1)^\nu$	$-(-1)^\mu$	$(-1)^\mu$
C	$+1$	$+1$	-1	$+1$	-1	-1	$+1$	-1
CP	$+1$	-1	$-(-1)^\mu$	$-(-1)^\mu$	$-(-1)^\mu(-1)^\nu$	$(-1)^\mu(-1)^\nu$	$(-1)^\mu$	$-(-1)^\mu$
CPT	$+1$	$+1$	-1	-1	$+1$	$+1$	-1	$+1$

Using these relations, and recalling that $\Lambda^{\mu}{}_{\alpha}\Lambda^{\nu}{}_{\beta}\Lambda^{\sigma}{}_{\gamma}\Lambda^{\rho}{}_{\delta}\varepsilon^{\alpha\beta\gamma\rho} = \det(\Lambda)\varepsilon^{\mu\nu\sigma\rho}$ for the Levi-Civita symbol $\varepsilon^{\mu\nu\sigma\rho}$ under any transformation Λ, we can derive the CPT behaviour of the interaction Lagrangians (1) and (2):

Table 2: CPT behaviour of interactions Lagrangians.

Form Factor	C	P	T	CP	CPT
εe	$+1$	$+1$	$+1$	$+1$	$+1$
MDM	$+1$	$+1$	$+1$	$+1$	$+1$
EDM	$+1$	-1	-1	-1	$+1$
AM	-1	-1	$+1$	$+1$	$+1$
CR	$+1$	$+1$	$+1$	$+1$	$+1$
Rayleigh	$+1$	$+1$	$+1$	$+1$	$+1$
Pseudo-Rayleigh	$+1$	$+1$	$+1$	$+1$	$+1$

From Tab. 2 it is possible to see that the EDM has CP violation, as expected of the electric dipole moment. Further, it can be seen that the AM violates C and P separately, while all other interactions are completely invariant under any discrete transformation.

3.2 Non-relativistic Correspondence of Form Factor Interactions

It is instructive to look at the low-energy forms of the form factor interactions, to see how they relate to non-relativistic quantum mechanics. In order to study the non-relativistic (NR) limit $\left|\vec{p}_\chi\right| \ll m_\chi$, we look at Dirac bilinears in the Dirac basis for the gamma matrices:

$$\gamma^0 = \begin{pmatrix} \mathbb{1} & 0 \\ 0 & -\mathbb{1} \end{pmatrix}, \; \gamma^j = \begin{pmatrix} 0 & \sigma^j \\ -\sigma^j & 0 \end{pmatrix}, \; \gamma^5 = \begin{pmatrix} 0 & \mathbb{1} \\ \mathbb{1} & 0 \end{pmatrix}, \; \vec{p}\cdot\vec{\sigma} = \begin{pmatrix} p_z & p_x - ip_y \\ p_x + ip_y & -p_z \end{pmatrix}, \tag{5}$$

where $\vec{\sigma} = (\sigma^1, \sigma^2, \sigma^3)$ is the vector of Pauli matrices and $\{\gamma^\mu, \gamma^\nu\} = 2\eta^{\mu\nu}\mathbb{1}$ is the defining relation of the Clifford algebra of Dirac matrices. It follows that $(\vec{p}\cdot\vec{\sigma})^2 = \vec{p}^{\,2}\mathbb{1}$. The Dirac spinors $u_s(p)$ are used in the Dirac-Pauli form [53]

$$u_s(p) = \sqrt{E_p + m_\chi}\begin{pmatrix} \xi_s \\ \frac{\vec{p}\cdot\vec{\sigma}}{E_p + m_\chi}\xi_s \end{pmatrix}, \quad \bar{u}_s(p) = u_s(p)^\dagger\gamma^0, \tag{6}$$

where $E_p^2 = m_\chi^2 + \vec{p}^{\,2}$ is the energy of the fermion with momentum p and mass m_χ, and ξ_s is a 2-component Pauli spinor with $s = 1, 2$ orthogonal spin states. Recalling the relation of the Pauli matrices $\sigma^i\sigma^j = \delta^{ij} + i\varepsilon^{ijk}\sigma^k$, the resulting NR approximations to lowest $\mathcal{O}\left(\left|\vec{q}_\chi\right|\right)$ are $(j = 1, 2, 3)$:

$$\bar{u}_s(p_2)u_r(p_1) \xrightarrow{NR} 2m_\chi\xi_s^\dagger\xi_r, \tag{7a}$$

$$\bar{u}_s(p_2)\gamma^5 u_r(p_1) \xrightarrow{NR} -\xi_s^\dagger[\vec{q}\cdot\vec{\sigma}]\xi_r, \tag{7b}$$

$$\bar{u}_s(p_2)\gamma^\mu u_r(p_1) \xrightarrow{NR} \begin{cases} 2m_\chi\xi_s^\dagger\xi_r, & \text{for } \mu = 0 \\ \xi_s^\dagger[p_1^j + p_2^j - i\varepsilon^{jil}q^i\sigma^l]\xi_r, & \text{for } \mu = j \end{cases}, \tag{7c}$$

$$\bar{u}_s(p_2)\gamma^\mu\gamma^5 u_r(p_1) \xrightarrow{NR} \begin{cases} \xi_s^\dagger[\vec{\sigma}\cdot(\vec{p}_1 + \vec{p}_2)]\xi_r, & \text{for } \mu = 0 \\ 2m_\chi\xi_s^\dagger\sigma^j\xi_r, & \text{for } \mu = j \end{cases}, \tag{7d}$$

$$\bar{u}_s(p_2)\sigma^{\mu\nu}q_\nu u_r(p_1) \xrightarrow{NR} \begin{cases} i\xi_s^\dagger[\vec{q}^{\,2} + i\varepsilon^{jil}q^j(p_1^i + p_2^i)\sigma^l]\xi_r, & \text{for } \mu = 0 \\ -i2m_\chi\xi_s^\dagger[-i\varepsilon^{jil}q^i\sigma^l]\xi_r, & \text{for } \mu = j \end{cases}, \tag{7e}$$

$$\bar{u}_s(p_2)\sigma^{\mu\nu}\gamma^5 q_\nu u_r(p_1) \xrightarrow{NR} \begin{cases} i2m_\chi\xi_s^\dagger[\vec{q}\cdot\vec{\sigma}]\xi_r, & \text{for } \mu = 0 \\ i\xi_s^\dagger[\vec{\sigma}\cdot(2\vec{p}_2 + \vec{q})q^j + i\varepsilon^{jil}q^i(p_1^l + p_2^l) - 2\vec{q}^{\,2}\sigma^j]\xi_r, & \text{for } \mu = j \end{cases}, \tag{7f}$$

with $q = (p_2 - p_1)$. Using the relations (7a-7f), it is possible to study the correspondence of the EM form factors (1) and (2) to physical quantities. This retroactively justifies the terminology introduced earlier. In terms of notation for the momenta, refer to Fig. 10a for (1) and Fig. 10b for (2), respectively. The relativistic state normalisation in the NR limit is

$$\langle p, s|k, r\rangle = 2E_p(2\pi)^3\delta^{(3)}(\vec{p} - \vec{k})\delta_{sr} \xrightarrow{NR} 2m_\chi(2\pi)^3\delta^{(3)}(\vec{p} - \vec{k})\delta_{sr}. \tag{8}$$

When comparing (8) to the NR state normalisation $\langle p, s|k, r\rangle = (2\pi)^3\delta^{(3)}(\vec{p} - \vec{k})\delta_{sr}$, we see that it is necessary to account for an additional factor of $2m_\chi$, coming from the NR limit. In non-relativistic quantum mechanics, relativistic effects are usually described by a perturbation V with the matrix element $\langle\psi| V |\psi\rangle$. The form of this V, derived from the NR limit of the vertex functions Γ in (3a-3f), indicates to which non-relativistic effect the interaction terms in the Lagrangian corresponds. This is essentially the Born approximation in perturbation theory [53]. Specifically, we couple a fermion χ to an external EM field A_μ^{ex} and investigate the static case for these interactions.

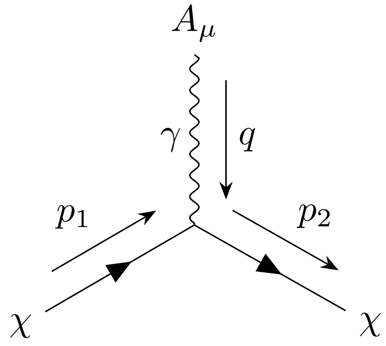

(a)

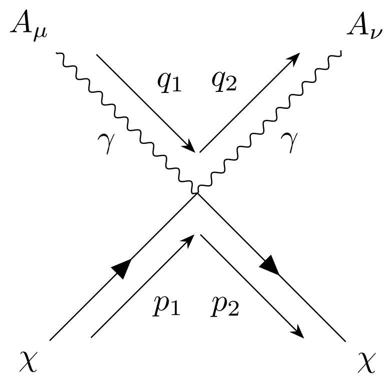

(b)

Figure 10: The vertices for the effective EM interactions: (a) shows the 3-vertex for εe, MDM, EDM, AM and CR. (b) shows the 4-vertex for the Rayleigh interactions. Momentum flow from left to right.

3.2.1 Correspondence of 3-vertex Interactions

We begin with the 3-vertex interactions and couple the *millicharge* vertex (3a) to an external electrostatic field $(A_\mu^{\text{ex}})(\vec{x}) = (\phi(\vec{x}), \vec{0})$, where $\phi(\vec{x})$ is the scalar Coulomb potential. Taking the NR limit yields

$$\frac{1}{2m_\chi}\left[\varepsilon e\bar{u}^s(p_2)\gamma^\mu u^r(p_1)\right]A_\mu^{\text{ex}} \xrightarrow{NR} \frac{1}{2m_\chi}\left[\varepsilon e 2m_\chi\xi_s^\dagger\xi_r\right]\phi(\vec{q}) = \xi_s^\dagger\left[\varepsilon e\phi(\vec{q})\right]\xi_r. \tag{9}$$

It is possible to read off the perturbation in momentum space from (9). Taking the Fourier transform of it results in $V(\vec{x}) = \varepsilon e\,\phi(\vec{x})$, which is a *Coulomb interaction* with charge εe, hence millicharge. This is expected of course, as the Lagrangian for this form factor has the same form as it does in ordinary QED.

Then, we couple the *magnetic dipole moment* vertex (3b) to an external potential $(A_\mu^{\mathrm{ex}})(\vec{x}) = (0, \vec{A}(\vec{x}))$ with static vector potential $\vec{A}(\vec{x})$, take the NR limit and Fourier transform (FT), resulting in

$$\begin{aligned}\frac{1}{2m_\chi}\Big[i\mu_\chi \bar{u}^s(p_2)\sigma^{\mu\nu}q_\nu u^r(p_1)\Big]A_\mu^{\mathrm{ex}} &\xrightarrow{NR} \frac{1}{2m_\chi}\Big[-i\mu_\chi 2m_\chi \xi_s^\dagger(-i\varepsilon^{jil}q^i\sigma^l)\xi_r\Big]A^j(\vec{q}) \\ &= \xi_s^\dagger\Big[i\mu_\chi\varepsilon^{ijl}q^iA^j(\vec{q})\sigma^l\Big]\xi_r \xrightarrow{FT} \xi_s^\dagger\Big[-\mu_\chi\varepsilon^{ijl}\partial^iA^j(\vec{x})\sigma^l\Big]\xi_r = \xi_s^\dagger\Big[-\mu_\chi B^l(\vec{x})\sigma^l\Big]\xi_r.\end{aligned} \tag{10}$$

Here the definition of the magnetic field $B^i = \varepsilon^{ijk}\partial^j A^k$ is used. One can read off the perturbation $V(\vec{x}) = -\mu_\chi\,\vec{\sigma}\cdot\vec{B} = -\vec{\mu}\cdot\vec{B}(\vec{x})$ with $\vec{\mu} = \mu_\chi\vec{\sigma}$. This is a *magnetic dipole interaction*, hence μ_χ is the *magnetic dipole moment* of the particle.

Next, we couple the *electric dipole moment* vertex (3c) with an external field $(A_\mu^{\mathrm{ex}})(\vec{x}) = (\phi(\vec{x}), \vec{0})$ and take the NR limit, yielding

$$\begin{aligned}\frac{1}{2m_\chi}\Big[-d_\chi\bar{u}^s(p_2)\sigma^{\mu\nu}\gamma^5q_\nu u^r(p_1)\Big]A_\mu^{\mathrm{ex}} &\xrightarrow{NR} \frac{1}{2m_\chi}\Big[-id_\chi 2m_\chi\xi_s^\dagger(\vec{q}\cdot\vec{\sigma})\xi_r\Big]\phi(\vec{q}) \\ &= \xi_s^\dagger\Big[-id_\chi\vec{q}\phi(\vec{q})\cdot\vec{\sigma}\Big]\xi_r \xrightarrow{FT} \xi_s^\dagger\Big[d_\chi\vec{\nabla}\phi(\vec{x})\cdot\vec{\sigma}\Big]\xi_r = \xi_s^\dagger\Big[-d_\chi\vec{E}(\vec{x})\cdot\vec{\sigma}\Big]\xi_r.\end{aligned} \tag{11}$$

Recalling that per definition $\vec{E} = -\vec{\nabla}\phi(\vec{x})$, the perturbation is $V(\vec{x}) = -d_\chi\,\vec{\sigma}\cdot\vec{E} = -\vec{d}\cdot\vec{E}(\vec{x})$, where $\vec{d} = d_\chi\vec{\sigma}$. This is an *electric dipole interaction*, thus d_χ is the *electric dipole moment* of the particle.

Coupling the *anapole moment* vertex (3d) with an external static vector potential $(A_\mu^{\mathrm{ex}})(\vec{x}) = (0, \vec{A}(\vec{x}))$, and taking the NR limit, results in

$$\begin{aligned}&\frac{1}{2m_\chi}\Big[-a_\chi\big(\bar{u}^s(p_2)\gamma^\mu\gamma^5q^2u^r(p_1) - \bar{u}^s(p_2)\gamma^\nu\gamma^5q^\mu q_\nu u^r(p_1)\big)\Big]A_\mu^{\mathrm{ex}} \\ \xrightarrow{NR}\ &\frac{-a_\chi}{2m_\chi}\Big[2m_\chi\xi_s^\dagger\sigma^jq^2\xi_r + 2m_\chi\xi_s^\dagger\sigma^kq^jq^k\xi_r\Big]A^j(\vec{q}) = \xi_s^\dagger\Big(-a_\chi\big(-\sigma^jq^2A^j - \sigma^kq^kq^jA^j\big)\Big)\xi_r \\ \xrightarrow{FT}\ &\xi_s^\dagger\Big[-a_\chi\big(\vec{\sigma}\cdot(-\Delta\vec{A}) + (\vec{\sigma}\cdot\vec{\nabla})\vec{\nabla}\cdot\vec{A}\big)\Big]\xi_r = \xi_s^\dagger\Big[-a_\chi\vec{\sigma}\cdot\big(\vec{\nabla}(\vec{\nabla}\cdot\vec{A}) - \Delta\vec{A}\big)\Big]\xi_r.\end{aligned} \tag{12}$$

Keeping in mind that here $\partial_0A^j = 0$, as $\vec{A}$ is static, and thus $q^2A^j \xrightarrow{FT} \Delta A^j$ in the signature used, it is possible to replace d'Alembertian with the Laplacian. Additionally, we have used the identity $\vec{\nabla}\times(\vec{\nabla}\times\vec{A}) = \vec{\nabla}(\vec{\nabla}\cdot\vec{A}) - \Delta\vec{A}$ and the definition of the magnetic field $\vec{B} = \vec{\nabla}\times\vec{A}$ to simplify the expression above. Consequently, the perturbation $V(\vec{x}) = -a_\chi\,(\vec{\sigma}\cdot(\vec{\nabla}\times\vec{B}))$ is obtained. This is called an *anapole interaction* with a_χ as the *anapole moment* [54] of the particle. Of note is also, that the AM operator is proportional to $\partial_\mu F^{\mu\nu} = J^\nu$, where J^ν is the electromagnetic current. This implies that the AM couples only to external currents, as noted previously, this interactions does not couple to on-shell photons.

Finally, we couple the *charge radius* vertex (3e) with an external electrostatic field $(A_\mu^{\mathrm{ex}})(\vec{x}) = (\phi(\vec{x}), \vec{0})$ and take the NR limit.

$$\begin{aligned}&\frac{1}{2m_\chi}\Big[b_\chi\big(\bar{u}^s(p_2)\gamma^\mu q^2u^r(p_1) - \bar{u}^s(p_2)\gamma^\nu q^\mu q_\nu u^r(p_1)\big)\Big]A_\mu^{\mathrm{ex}} \\ \xrightarrow{NR}\ &\frac{b_\chi}{2m_\chi}\Big[2m_\chi\xi_s^\dagger q^2\xi_r + \xi_s^\dagger\mathcal{O}(q^0)\xi_r\Big]\phi(\vec{q}) = \xi_s^\dagger\Big[b_\chi q^2\phi(\vec{q})\Big]\xi_r + \mathcal{O}\big(q^0\phi(\vec{q})\big)\xi_s^\dagger\Big[b_\chi q^2\phi(\vec{q})\Big]\xi_r \\ \xrightarrow{FT}\ &\xi_s^\dagger\Big[b_\chi\Delta\phi(\vec{x})\Big]\xi_r = \xi_s^\dagger\Big[-b_\chi\rho(\vec{x})\Big]\xi_r,\end{aligned} \tag{13}$$

where we neglected all terms with $q^0\phi(\vec{q})$, as these vanish after a Fourier transform due to ϕ being static. The Poisson equation $\Delta\phi(\vec{x}) = -\rho(\vec{x})$ for the charge distribution ρ was also used. Thus, the perturbation

$V(\vec{x}) = -b_\chi\,\rho(\vec{x})$ is derived, which can be interpreted as a Coulomb interaction with an induced charge distribution across a mean square *charge radius* of b_χ. To check this, it is possible to employ dimensional analysis of $b_\chi \sim r^2$ and $\rho \sim Qr^{-3}$, such that $b_\chi\rho \sim Qr^{-1}$, which has the dimensionality of a Coulomb potential.

3.2.2 Correspondence of 4-vertex Interactions

Now, moving on to 4-vertex interactions, we couple the scalar Rayleigh vertex (3f) with two external electrostatic field $(A_\mu^{\rm ex})(\vec{x}_1) = (\phi(\vec{x}_1), \vec{0})$ and $(A_\nu^{\rm ex})(\vec{x}_2) = (\phi(\vec{x}_2), \vec{0})$ then take the NR limit.

$$\begin{aligned}
&\frac{1}{2m_\chi}\Big[r_\chi\big(q_1^\mu q_2^\nu - q_1\cdot q_2\eta^{\mu\nu}\big)\bar{u}^s(p_2)u^r(p_1)\Big]A_\mu^{\rm ex}A_\nu^{\rm ex} \\
\xrightarrow{NR}\ &\frac{1}{2m_\chi}\Big[r_\chi\big(q_1^0 q_2^0 - q_1\cdot q_2\eta^{00}\big)2m_\chi\xi_s^\dagger\xi_r\Big]\phi(\vec{p}_1)\phi(\vec{p}_2) = \xi_s^\dagger\Big[-r_\chi(q_1\phi(\vec{p}_1))\cdot(q_2\phi(\vec{p}_2))\Big]\xi_r \\
\xrightarrow{FT}\ &\xi_s^\dagger\Big[r_\chi\vec{\nabla}\phi(\vec{x}_1)\cdot\vec{\nabla}\phi(\vec{x}_2)\Big]\xi_r = \xi_s^\dagger\Big[r_\chi\vec{E}(\vec{x}_1)\cdot\vec{E}(\vec{x}_2)\Big]\xi_r,
\end{aligned} \tag{14}$$

where all terms with $q^0\phi(\vec{q})$ vanished after the Fourier transform since ϕ is static. Additionally, the definition of the electric field $\vec{E}(\vec{x}) = -\vec{\nabla}\phi(\vec{x})$ was used. Now, the perturbation $V(\vec{x}) = r_\chi\,\vec{E}(\vec{x}_1)\cdot\vec{E}(\vec{x}_2)$ can be read-off. This V looks like the potential energy of an electric field $U = \frac{1}{2}(1+\chi_e)\varepsilon_0\vec{E}^2$ with χ_e being the electric susceptibility. As $\varepsilon_0 = 1$ in natural units, it is possible to identify a direct relation between r_χ and χ_e and call this interaction a *susceptibility interaction*. The name *Rayleigh interaction* comes from the fact that a particle and a photon scatter directly at a vertex. Rayleigh scattering takes place for photons with wavelengths λ_γ large compared to the size of particles they scatter off $\lambda_\chi \ll \lambda_\gamma$. The size of particles in quantum interactions can be taken as their Compton wavelength, and so $\lambda_\gamma \gg 1/m_\chi \Leftrightarrow E_\gamma \ll m_\chi$. This is the case when the incoming photon has an energy smaller than the mass of the particle, a Rayleigh-like scattering happens at the vertex, hence the name. Pseudo-Rayleigh scattering has no direct correspondence to a non-relativistic interaction.

3.3 Exemplary UV-complete Theories for Electromagnetic Form Factors

Before continuing with the explicit computation of the relevant cross sections, we want to briefly discuss two potential UV-complete theories that can give rise to millicharge and to a magnetic dipole moment interaction, respectively. Here, we will present a cursory treatment in order to motivate the previously mentioned models. For the purpose of this work, the full theory is largely unimportant, as our results are applicable to any theory giving rise to the interactions (3a-3g), assuming the low energy condition for the form factor EFT holds.

3.3.1 Dark Photon Theory and Millicharge

Let us begin by considering *millicharge*. This fractional electric charge may arise in a so-called *dark photon* mediated model. Following [28], a new abelian gauge symmetry, called $\mathrm{U(1)_D}$, is introduced to the SM with the corresponding gauge field $\tilde{B}_\mu$. This new gauge field kinetically mixes with the SM U(1) hypercharge gauge field $\hat{B}_\mu$. The corresponding Lagrangian of this modification reads

$$\mathcal{L} = \hat{g}_1 J^\mu_{\rm SM}\hat{B}_\mu - \frac{1}{4}\hat{B}_{\mu\nu}\hat{B}^{\mu\nu} - \frac{\epsilon}{2}\hat{B}_{\mu\nu}\tilde{B}^{\mu\nu} - \frac{1}{4}\tilde{B}_{\mu\nu}\tilde{B}^{\mu\nu} + g_{\rm D}J^\mu_{\rm D}\tilde{B}_\mu, \tag{15}$$

where $\tilde{B}_{\mu\nu} = \partial_\mu \tilde{B}_\nu - \partial_\nu \tilde{B}_\mu$ is the field strength of $\tilde{B}_\mu$, $\hat{B}_{\mu\nu}$ the field strength of $\hat{B}_\mu$, $\hat{g}_1$ and g_D are the respective gauge couplings; J^μ_SM is the hypercharge current of the SM, $J^\mu_\mathrm{D} = \bar{\chi}\gamma^\mu\chi$ is the dark current of the dark sector fermions χ charged under $\mathrm{U}(1)_\mathrm{D}$. ϵ is the kinetic mixing parameter of the gauge fields. Importantly, no mass term is introduced for the new $\tilde{B}_\mu$, although there are models with a massive vector boson. The focus here is on a *massless* theory for the dark photon, in order to investigate millicharge. The off-diagonal kinetic term, after *electroweak symmetry breaking* (EWSB), leads to a mixing of the new dark photon with the photon and the Z-boson of the SM. We want to diagonalise the kinetic term by introducing a real one-parameter transformation T, that takes the fields $\hat{B}_\mu$ and $\tilde{B}_\mu$ to the ordinary SM hypercharge field B_μ and the new dark photon field B'_μ, which has the form

$$T\begin{pmatrix} B \\ B' \end{pmatrix} = \begin{pmatrix} a & c \\ b & d \end{pmatrix}\begin{pmatrix} B \\ B' \end{pmatrix} = \begin{pmatrix} \hat{B} \\ \tilde{B} \end{pmatrix}. \tag{16}$$

A T that diagonalises the matrix K in the kinetic term $-\frac{1}{4}\vec{B}^\dagger K \vec{B}$, where $\vec{B}$ is the vector of the field strengths of $\hat{B}_\mu$ and $\tilde{B}_\mu$, must fulfil

$$-\frac{1}{4}T^\dagger K T = -\frac{1}{4}\begin{pmatrix} a & b \\ c & d \end{pmatrix}\begin{pmatrix} 1 & \epsilon \\ \epsilon & 1 \end{pmatrix}\begin{pmatrix} a & c \\ b & d \end{pmatrix} \stackrel{!}{=} -\frac{1}{4}\begin{pmatrix} 1 & 0 \\ 0 & 1 \end{pmatrix}. \tag{17}$$

When solving this system of equations, it becomes apparent that it has no solution unless an off-diagonal argument is set to zero. We choose $b = 0$ and solve for T, such that the SM hypercharge field B is just a rescaled version of $\hat{B}$. This results in

$$T = \begin{pmatrix} \frac{1}{\sqrt{1-\epsilon^2}} & 0 \\ -\frac{\epsilon}{\sqrt{1-\epsilon^2}} & 1 \end{pmatrix} \Rightarrow \begin{pmatrix} \hat{B} \\ \tilde{B} \end{pmatrix} = \begin{pmatrix} \frac{1}{\sqrt{1-\epsilon^2}}B \\ B' - \frac{\epsilon}{\sqrt{1-\epsilon^2}}B \end{pmatrix} \tag{18}$$

for the transform T. Correspondingly, the new fields B_μ and B'_μ are a mixture of the old fields $\hat{B}_\mu$ and $\tilde{B}_\mu$. No physical change to the system was made, since only transformations and field rescalings were applied to diagonalise the kinetic term. The resulting Lagrangian, transformed from (15), is

$$\mathcal{L}' = \frac{\hat{g}_1}{\sqrt{1-\epsilon^2}} J^\mu_\mathrm{SM} B_\mu - \frac{1}{4}B_{\mu\nu}B^{\mu\nu} - \frac{1}{4}B'_{\mu\nu}B'^{\mu\nu} + g_\mathrm{D} J^\mu_\mathrm{D}\left(B'_\mu - \frac{\epsilon}{\sqrt{1-\epsilon^2}}B_\mu\right), \tag{19}$$

where it is now possible to redefine the hypercharge coupling as $g_1 = \hat{g}_1/\sqrt{1-\epsilon^2}$, having separated the SM sector from the dark sector, save for a single interaction term of the dark current J^μ_D with the hypercharge field B_μ. Now, the phenomena we want to observe will overwhelmingly happen below the electroweak scale. Therefore, it is necessary to consider the Lagrangian (19) after EWSB. The canonical approach is implemented here, and includes the new field B' only trivially, such that

$$\begin{pmatrix} A \\ Z \\ A' \end{pmatrix} = \begin{pmatrix} \cos\theta_W & \sin\theta_W & 0 \\ -\sin\theta_W & \cos\theta_W & 0 \\ 0 & 0 & 1 \end{pmatrix}\begin{pmatrix} B \\ W^3 \\ B' \end{pmatrix} \tag{20}$$

where θ_W is the Weinberg, or weak mixing, angle, W^3 is the third component of the SU(2) gauge field, and A, Z, A' are the SM photon, the Z-boson and the dark photon fields, respectively. This yields the final Lagrangian for the Standard Model with a millicharged dark sector

$$\begin{aligned} \mathcal{L}_\mathrm{tot} &= \mathcal{L}_\mathrm{SM} - \frac{1}{4}F'_{\mu\nu}F'^{\mu\nu} + g_\mathrm{D} J^\mu_\mathrm{D} A'_\mu - \frac{\epsilon g_\mathrm{D}}{\sqrt{1-\epsilon^2}} J^\mu_\mathrm{D}\Big(\cos\theta_W A_\mu - \sin\theta_W Z_\mu\Big) \\ &= \mathcal{L}_\mathrm{SM} - \frac{1}{4}F'_{\mu\nu}F'^{\mu\nu} + g_\mathrm{D} J^\mu_\mathrm{D} A'_\mu - \varepsilon e J^\mu_\mathrm{D} A_\mu + Q^Z_\mathrm{eff} J^\mu_\mathrm{D} Z_\mu, \end{aligned} \tag{21}$$

where $F'_{\mu\nu}$ is the dark photon field strength, $Q^Z_\mathrm{eff} = (\epsilon g_\mathrm{D} \sin\theta_W)/\sqrt{1-\epsilon^2}$ is the effective induced coupling of the dark current to the SM Z-boson, and $\varepsilon e = (\epsilon g_\mathrm{D} \cos\theta_W)/\sqrt{1-\epsilon^2}$ is the effective coupling of the dark current to the SM photon, with ε being the induced millicharge. The normalisation of this millicharge to the fundamental charge e is chosen such that it is possible to treat dark fermions just like leptons, albeit with a diminished electric charge. The different sign of the photon-dark coupling term just means a positive $\mathrm{U(1)_D}$ charge of a dark fermionic particle χ leads to a negative millicharge and vice-versa. For our purposes, we can largely ignore the interaction of χ with the Z-boson, as it is suppressed by the Z-mass. After seeing this derivation, it becomes quite clear as to why the coupling of the induced interaction of the dark sector with the SM photon is called millicharge. Since this induced coupling must be small, otherwise the effects would have long been seen, it must be a fraction of the fundamental charge, hence a *milli*-charge. Unfortunately, however, the measurement of a millicharge does not allow to uniquely determine the parameters of the theory, as it depends both on the dark coupling g_D as well as the kinetic mixing ϵ. For a more thorough treatment of dark photon theories see [28].

3.3.2 Charged Scalar Model and Magnetic Dipole Moment

Next, we will discuss a UV-complete toy model that gives rise to a magnetic dipole moment. The treatment here will follow [55] and [56]. This model adds a new heavy scalar S to the Standard Model that is charged under its hypercharge group $U(1)_Y$ with $Y = 1$. After electroweak symmetry, this gives S an electric charge of $Q_S = Ye$. This scalar couples a new fermion χ, with mass m_χ, to the SM leptons ψ_l via a Yukawa interaction y_l. The interaction Lagrangian reads

$$\mathcal{L}_\mathrm{int} = -y_l S \bar{\chi} P_R \psi_l + \mathrm{h.c.}, \tag{22}$$

where $P_R = (1+\gamma^5)/2$ is the right-handed projector. The Feynman rule stemming from (22) is then

$$\Gamma = -iy_l P_{R/L}, \tag{23}$$

with $P_L = (1-\gamma^5)/2$, where the projector changes depending on if the lepton on the vertex is an antiparticle or not. In order to see that this interaction gives rise to a magnetic dipole moment of χ, it is necessary to match the effective operator of MDM (1b) to the UV-complete theory. Similar to the anomalous MDM of charged leptons, the MDM of the uncharged χ arises through loop effects, specifically a triangle loop at a photon-fermion three-vertex. This can be seen in Fig. 11.

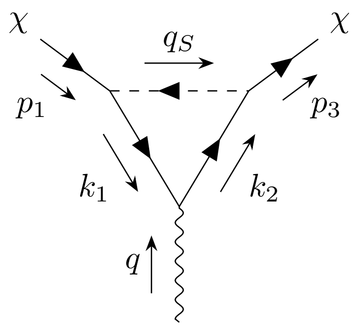

Figure 11: A triangle loop diagram inducing a MDM for the neutral χ.

In Fig. 11, k_1 is the free loop momentum, while $q = p_3 - p_1$, $q_S = p_1 - k_1$ and $k_2 = k_1 + q$. Importantly, there is a second diagram which has the internal lepton and scalar lines swapped, which will be neglected here. The reasons for this are twofold. Firstly this diagram has an additional suppression by the scalar mass M due to the added propagator and secondly, the coupling of charged scalars to photons is momentum dependent, which further suppresses the contribution of this diagram for small momenta q. Since

MDM is an effect of real particles, it is necessary to put the external χ spinors on-shell. The resulting amplitude is

$$\begin{aligned} i\mathcal{M}^\mu &= \bar{u}_3 \int \frac{d^4k_1}{(2\pi)^4} P_R \frac{(-iy_l)i(\not{k}_2+m_l)}{k_2^2-m_l^2+i\epsilon}(-iQ_S)\gamma^\mu \frac{i(\not{k}_1+m_l)}{k_1^2-m_l^2+i\epsilon} P_L \frac{(-iy_l)i}{q_S^2-M^2+i\epsilon} u_1 \\ &= (y_l^2 Q_S)\bar{u}_3 P_R \int \frac{d^4k_1}{(2\pi)^4} \frac{(\not{k}_1+\not{q}+m_l)\gamma_\mu(\not{k}_1+m_l)}{((k_1+q)^2-m_l^2+i\epsilon)(k_1^2-m_l^2+i\epsilon)((p_1-k_1)^2-M^2+i\epsilon)} P_L u_1 \end{aligned} \tag{24}$$

where $\bar{u}_3$ is the on-shell spinor of the outgoing χ, u_1 the on-shell spinor of the incoming χ and m_l is the lepton mass. Instead of the expected lepton charge Q_l, we have put the corresponding charge of the scalar, since $Q_l = -Q_S$ is enforced by gauge invariance and writing Q_S makes it more apparent that the effect arises due to S. Using Feynman parameters with $k = k_1 + yq - zp_1$, (24) becomes

$$i\mathcal{M}^\mu = (y_l^2 Q_S)\bar{u}_3 P_R \int_0^1 dz \int_0^{1-z} dy \int \frac{d^dk}{(2\pi)^d} \frac{(\not{k}+(1-y)\not{q}+z\not{p}_1+m_l)\gamma_\mu(\not{k}-y\not{q}+z\not{p}_1+m_l)}{(k^2-\Delta+i\epsilon)^3} P_L u_1, \tag{25}$$

where $\Delta = y(y-1)q^2 + z(1-z)p_1^2 - 2yz(p_1\cdot q) + z(m_l^2+M^2) + m_l^2$ and the integral is now in d-dimensions for later use in dimensional regularisation. The numerator in (25), after simplifying using the definition of k and the properties of the chiral projectors $P_{R/L}$, becomes

$$\bar{u}_3 P_R \Gamma_S^\mu u_1 = (y_l^2 Q_S)\bar{u}_3 P_R \left[(\not{k}+(1-y)\not{q}+z\not{p}_1)\gamma^\mu(\not{k}-y\not{q}+z\not{p}_1) + m_l^2\gamma^\mu\right] u_1. \tag{26}$$

To be able to match the UV-complete amplitude to the effective one, it is useful to project out the relevant operator (3b), namely $\sigma^{\mu\nu}q_\nu$. Since this operator has no γ^5, it is sufficient to look at the $\mathbb{1}$-part of the numerator by expanding the projector. To facilitate the extraction of the MDM, (26) can be simplified and rewritten using Dirac algebra, the on-shell conditions for the spinors $\not{p}_1 u_1 = m_\chi u_1$ and $\bar{u}_3\not{p}_1 = m_\chi \bar{u}_3$, and the integral identity for $k^\mu k^\nu d^dk = \frac{1}{d}k^2 g^{\mu\nu} d^dk$ due to Lorentz invariance, as well as the fact that integrals over an odd number of k vanish, resulting in

$$\begin{aligned} \frac{1}{2}\bar{u}_3\Gamma_S^\mu u_1 = \frac{y_l^2 Q_S}{2}\bar{u}_3 \bigg\{ &\left[\frac{2-d}{d}k^2 + \big(y(y-1)+\frac{1}{2}(1-2y)\big)q^2 - z^2 m_\chi^2 + m_l^2\right]\gamma^\mu \\ &+ z(1-2y)m_\chi q^\mu + 2zm_\chi p_1^\mu + iq_\alpha(k_\beta + zp_{1,\beta})\varepsilon^{\mu\alpha\beta\sigma}\gamma_\sigma \bigg\} u_1, \end{aligned} \tag{27}$$

where we have additionally used $q \cdot p_1 = -q^2/2$. The part of (27) proportional to the Levi-Civita tensor is not relevant to MDM and can thus be neglected in further calculations. As the MDM interaction also exists for on-shell photons, the part proportional to the photon momentum q^μ can also be neglected. Thus, the MDM (3b) operator is extracted from the p_1^μ part by using the Gordon identity

$$2\bar{u}_3 u_1 p_1^\mu = \bar{u}_3\left(2m_\chi\gamma^\mu - q^\mu - i\sigma^{\mu\nu}q_\nu\right)u_1. \tag{28}$$

As mentioned before, the q^μ part again vanishes for on-shell photons. Combining the Gordon identity (28) with the numerator (27) and the full integral in (25) results in the relevant Dirac structure for the MDM

$$\begin{aligned} i\Gamma_{\mathrm{MDM}}^\mu &= \frac{y_l^2 Q_S}{2}\int_0^1 dz \int_0^{1-z} dy \int \frac{d^dk}{(2\pi)^d}\frac{-zm_\chi}{(k^2-\Delta+i\epsilon)^3}(i\sigma^{\mu\nu}q_v) \\ &= \frac{iy_l^2 Q_S}{64\pi^2}\int_0^1 dz \int_0^{1-z} dy \frac{zm_\chi}{\Delta}(i\sigma^{\mu\nu}q_v). \end{aligned} \tag{29}$$

The the integral over the virtual momentum k is a standard result [27]. It is still necessary to solve the remaining integrals in (29). In this model, the mass hierarchy is $M \gg m_\chi$ and $M \gg m_l$, which, together with the on-shell condition for photons $q^2 = 0$, allows for the approximation of the integrand. The integration result consequently behaves like

$$i\Gamma^{\mu}_{\mathrm{MDM}} \sim y_l^2 Q_S \frac{m_\chi}{M^2} \sigma^{\mu\nu} q_v. \tag{30}$$

Now, when matching (30) with the vertex function for the MDM (3b), the magnetic dipole moment μ_χ, to the lowest order in $1/M$, shows a behaviour that goes as

$$\mu_\chi \sim \frac{y_l^2 Q_S}{M} \frac{m_\chi}{M}. \tag{31}$$

Having arrived at this result, it is instructive to check this manual calculation. We use Package-X [57, 58] for this purpose, by projecting out the MDM operator in the loop integral and subsequently evaluating (24). The output of this integration is then expanded in the same manner as the manual result, namely $M \gg m_\chi$, $M \gg m_l$ and $q^2 = 0$, yielding to the lowest order in $1/M$ for the MDM

$$\mu_\chi = \frac{y_l^2 Q_S}{96\pi^2} \frac{m_\chi}{M^2}. \tag{32}$$

The result from the full loop integration, without the approximation of the integrand used in the manual calculation, shows the same scaling behaviour, confirming (31). In conclusion, (31) and (32) have successfully shown how EM form factors can arise from a UV-complete model. As this is just a toy model, the exact numerical prefactors are unimportant, but the dependence of the MDM on the Yukawa coupling, as well as on the electric charge and the mass of the scalar mediator, are clearly apparent.

4 Elastic Scattering Processes of Form Factor Dark Matter

Now we will finally move on to the calculations needed in order to compute event rates at a detector. We will start off with 2-to-2 processes. Namely, electron-χ elastic scattering and $\chi\chi$ non-relativistic elastic scattering. While the $e^-\chi$ process is necessary for the calculation of our detection rate, we also briefly discuss χ self-scattering due to importance for astrophysical observations of the self-interaction of dark matter. The general formula for a 2-to-2 scattering cross section of incoming particles with momenta p_1, p_2 and masses m_1, m_2 into outgoing particles with momenta p_3, p_4 and masses m_3, m_4 is [53]:

$$d\sigma_{p_1,p_2\to p_3,p_4} = \frac{1}{4\sqrt{(p_1\cdot p_2)^2 - m_1^2 m_2^2}} |\mathcal{M}(p_1,p_2\to p_3,p_4)|^2 d\Pi_2(p_3,p_4), \tag{33}$$

where $\mathcal{M}(p_1,p_2\to p_3,p_4)$ is the scattering matrix element and $d\Pi_2(p_3,p_4)$ is the Lorentz invariant two-body phase space

$$d\Pi_2(p_3,p_4) = \prod_{i=3}^{4} \frac{d^3p_i}{(2\pi)^3 2E_i} (2\pi)^4 \delta^{(4)}\left(p_1 + p_2 - \sum_{j=3}^{4} p_j\right), \tag{34}$$

where $E_i = \sqrt{m_i^2 + \vec{p}_i^{\,2}}$ is the energy of the particle with three momentum $\vec{p}_i$ and mass m_i.

4.1 Electron-Dark Matter Elastic Scattering

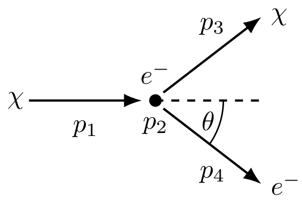

Figure 12: Kinematics of $e^-\chi$ elastic scattering in the electron's rest frame with corresponding momenta. The scattering angle of the electron is denoted by θ in the diagram.

We want to calculate the scattering cross sections of χ and electrons for all interactions (3a-3e) in the lab frame, i.e. the rest frame of the target electron. This will be the *detection cross section* of the χ-particles produced in the potential experimental set-up described earlier. The conventions and relativistic kinematics can be seen in Fig. 12. The outgoing particles have four-momenta $p_{3,4} = (E_{3,4}, \vec{p}_{3,4})^{\mathrm{T}}$, the incoming χ-particle has a four-momentum $p_1 = (E_\chi, \vec{p}_1)^{\mathrm{T}}$, while the initial electron has $p_2 = (m_e, \vec{0})^{\mathrm{T}}$ in the lab frame. The *recoil cross section* of the scattering is needed to relate measurements of the energy, deposited by the χ particle into the electrons of a detector, to the parameters of the model. Hence we define the scattered electron's relativistic *recoil energy* as

$$E_R = E_4 - m_e. \tag{35}$$

Using the definition 35 and energy-momentum conservation $p_1 + p_2 = p_3 + p_4$, it is possible to eliminate the lab frame scattering angle θ by

$$\cos\theta = \frac{E_R(E_\chi + m_e)}{\sqrt{E_\chi^2 - m_\chi^2}\sqrt{E_R(E_R + 2m_e)}} \tag{36}$$

and express the Mandelstam variables s and t [27] using only the masses of the particles m_e, m_χ, as well as the recoil energy E_R and the energy E_χ of the incoming χ-particle:

$$s := (p_1 + p_2)^2 = m_\chi^2 + m_e^2 + 2m_e E_\chi, \tag{37a}$$

$$t := (p_2 - p_4)^2 = -2m_e E_R. \tag{37b}$$

This also gives the third Mandelstam variable u by the identity $s + t + u = 2m_\chi^2 + 2m_e^2$. With these results, it is possible to express the flux factor in the cross section (33) as

$$4\sqrt{(p_1 \cdot p_2)^2 - m_1^2 m_2^2} = 4m_e\sqrt{E_\chi^2 - m_\chi^2}. \tag{38}$$

The next step of the calculation is evaluating the two-body phase space integral (34):

$$\begin{aligned}\int d\Pi_2(p_3, p_4) &= \int \frac{d^3p_3 d^3p_4}{(2\pi)^3 2E_3 (2\pi)^3 2E_4}(2\pi)^4 \delta(E_\chi + m_e - E_3 - E_4)\delta^{(3)}(\vec{p}_1 - \vec{p}_3 - \vec{p}_4) \\ &= \int \frac{d^3p_4}{(2\pi)^2 4E_4}\frac{1}{\sqrt{m_\chi^2 + |\vec{p}_1 - \vec{p}_4|^2}}\delta\Big(E_\chi - E_R - \sqrt{m_\chi^2 + |\vec{p}_1 - \vec{p}_4|^2}\Big).\end{aligned} \tag{39}$$

Now, our objective is to resolve the Dirac delta function inside (39) in terms of the final state electron momentum P_f, and subsequently integrate it out. P_f is the positive root of the function inside the delta distribution, while the unphysical negative solution is discarded. Hence, this momentum, using relativistic kinematics, is given by $E_4^2 = P_f^2 + m_e^2$ and, equivalently, as $P_f^2 = E_R(E_R + 2m_e)$. It is now possible to solve the integral (39) using spherical coordinates, with $d\Omega_4 = d\cos\theta d\varphi$ being the 2-sphere integration measure, where the polar angle θ is given by (36) and φ is the azimuthal angle:

$$\begin{aligned}\int d\Pi_2(p_3, p_4) &= \int \frac{|\vec{p}_4|^2 d|\vec{p}_4| d\Omega_4}{(2\pi)^2 4E_4}\frac{1}{\sqrt{m_\chi^2 + |\vec{p}_1 - \vec{p}_4|^2}}\delta(|\vec{p}_4| - P_f)\frac{P_f\sqrt{m_\chi^2 + |\vec{p}_1 - \vec{p}_4|^2}E_4}{m_e E_R(E_\chi + m_e)} \\ &= \frac{1}{4}\int \frac{d\cos\theta d\varphi}{(2\pi)^2}\frac{P_f^3}{m_e E_R(E_\chi + m_e)} \\ &= \frac{1}{8\pi}\int dE_R \frac{1}{\sqrt{E_\chi^2 - m_\chi^2}}\frac{m_e E_R(E_\chi + m_e)}{[E_R(E_R + 2m_e)]^{3/2}}\frac{[E_R(E_R + 2m_e)]^{3/2}}{m_e E_R(E_\chi + m_e)} \\ &= \frac{1}{8\pi}\int dE_R \frac{1}{\sqrt{E_\chi^2 - m_\chi^2}},\end{aligned} \tag{40}$$

where we integrated over φ as this problem is rotationally symmetric. Additionally, we made use of (35) and (36) in order to transform the integration variable from $\cos\theta$ into E_R. The scattering cross section 33 in the lab frame becomes

$$\frac{d\sigma_{e^-\chi}}{dE_R} = \frac{|\mathcal{M}|^2}{32\pi m_e(E_\chi^2 - m_\chi^2)}. \tag{41}$$

After investigating the kinematics and solving the phase space integration, we move onto the calculation of the matrix elements of electron-χ scattering for the different EM form factor interactions at tree level. From now on, $\mathcal{M}$ will refer to the spin-summed matrix elements. $\mathcal{M}$ is evaluated using FeynCalc [59][60][61]. We use the Feynman gauge $\xi = 1$ for convenience. The gauge dependent part of the photon propagator would drop out regardless, due to the on-shell electron spinors. The Feynman diagram in Fig. 13 shows the scattering $\chi e^- \to \chi e^-$ at tree level for the 3-vertex EM form factors.

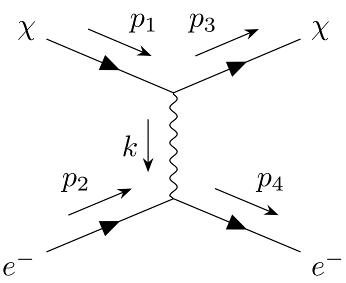

Figure 13: Elastic scattering of electrons with χ-particles at tree level. This diagram accounts for all 3-vertex EM form factor interactions.

We will not consider the dimension-7 operators (3f-3g) for further calculations in this work. The reasons for this are twofold. First, dimension-7 interaction couplings are even further suppressed by the EFT scale than dimension-5 and 6, reducing their cross section with respect to the higher dimensional ones. Secondly, the processes considered, $e^-\chi$ scattering for detection and $\chi\bar{\chi}$ particle pair production by e^-e^- bremsstrahlung, do not exist at tree level for these Rayleigh interactions. This introduces a further loop suppression into their cross sections.

The resulting squared spin-summed matrix elements $|\mathcal{M}|^2$ for each EM form factor (3a-3e) at tree level, in this case only the t-channel exists, expressed in terms of the particle masses, as well as the incoming energy E_χ and recoil energy E_R, are:

$$|\mathcal{M}|^2_{\varepsilon e} = \frac{2\varepsilon^2 e^4}{m_e E_R^2}\Big[2m_e E_\chi^2 - 2m_e E_\chi E_R + m_e E_R^2 - m_e^2 E_R - m_\chi^2 E_R\Big], \tag{42a}$$

$$|\mathcal{M}|^2_{\mathrm{MDM}} = \frac{4e^2\mu_\chi^2}{E_R}\Big[2m_e(E_\chi^2 - E_\chi E_R - m_\chi^2) + m_\chi^2 E_R\Big], \tag{42b}$$

$$|\mathcal{M}|^2_{\mathrm{EDM}} = \frac{4e^2 d_\chi^2}{E_R}\Big[2m_e E_\chi^2 - 2m_e E_\chi E_R - m_\chi^2 E_R\Big], \tag{42c}$$

$$|\mathcal{M}|^2_{\mathrm{AM}} = 8e^2 a_\chi^2 m_e\Big[m_e(2E_\chi^2 - 2E_\chi E_R + E_R^2 - 2m_\chi^2) - m_e^2 E_R + m_\chi^2 E_R\Big], \tag{42d}$$

$$|\mathcal{M}|^2_{\mathrm{CR}} = 8e^2 b_\chi^2 m_e\Big[m_e(2E_\chi^2 - 2E_\chi E_R + E_R^2) - m_e^2 E_R - m_\chi^2 E_R\Big]. \tag{42e}$$

This gives us the differential recoil cross section (41) with the fine-structure constant $\alpha = e^2/(4\pi)$:

$$\left(\frac{d\sigma_{e^-\chi}}{dE_R}\right)_{\varepsilon e} = \frac{\pi\varepsilon^2\alpha^2}{m_e^2(E_\chi^2 - m_\chi^2)E_R^2}\Big[2m_e E_\chi^2 + m_e E_R(E_R - m_e - 2E_\chi) - m_\chi^2 E_R\Big], \tag{43a}$$

$$\left(\frac{d\sigma_{e^-\chi}}{dE_R}\right)_{\mathrm{MDM}} = \frac{\alpha\mu_\chi^2}{2m_e(E_\chi^2 - m_\chi^2)E_R}\Big[2m_e(E_\chi^2 - E_\chi E_R - m_\chi^2) + m_\chi^2 E_R\Big], \tag{43b}$$

$$\left(\frac{d\sigma_{e^-\chi}}{dE_R}\right)_{\mathrm{EDM}} = \frac{\alpha d_\chi^2}{2m_e(E_\chi^2 - m_\chi^2)E_R}\Big[2m_e E_\chi^2 - 2m_e E_\chi E_R - m_\chi^2 E_R\Big], \tag{43c}$$

$$\left(\frac{d\sigma_{e^-\chi}}{dE_R}\right)_{\mathrm{AM}} = \frac{\alpha a_\chi^2}{(E_\chi^2 - m_\chi^2)}\Big[m_e(2E_\chi^2 - 2E_\chi E_R + E_R^2 - 2m_\chi^2) + (m_\chi^2 - m_e^2)E_R\Big], \tag{43d}$$

$$\left(\frac{d\sigma_{e^-\chi}}{dE_R}\right)_{\mathrm{CR}} = \frac{\alpha b_\chi^2}{(E_\chi^2 - m_\chi^2)}\Big[m_e(2E_\chi^2 - 2E_\chi E_R + E_R^2) - (m_\chi^2 + m_e^2)E_R\Big]. \tag{43e}$$

It is now possible to see from these results that the operators, that only differ by the fifth gamma matrix γ^5, (43b) and (43c), as well as (43d) and (43e), have the same matrix element structure, up to terms proportional to the mass of χ. When taking the low mass limit, these pairs will converge, only differing by the effective couplings. This suggests that the difference between these operator pairs is solely generated by the mass m_χ of the particle and becomes insignificant when χ is ultra-relativistic. This can be seen in Fig. 14 for the differential recoil cross section of MDM-EDM and AM-CR pairs at large values of E_R. The difference arises since the terms proportional to m_χ can also depend on E_R, meaning the interaction pairs begin to split near the kinematic endpoint of E_R.

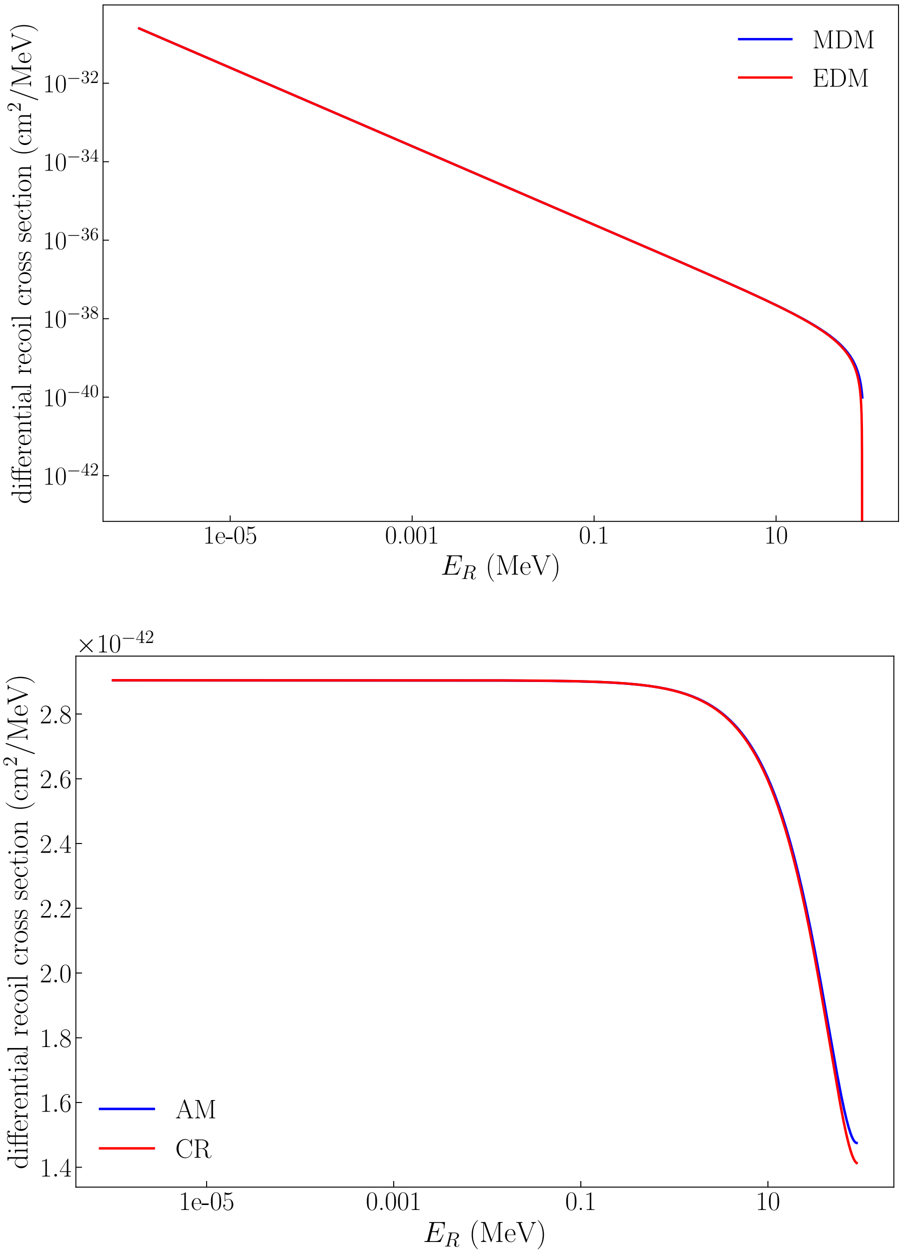

Figure 14: The upper image shows the total recoil cross section for MDM and EDM interactions for $m_\chi = 1\,\mathrm{MeV}$. The right graph similarly displays it for AM and CR. The values used are $E_\chi = 90\,\mathrm{MeV}$, $\mu_\chi = d_\chi = 10^{-6}\mu_B$ and $a_\chi = b_\chi = 10^{-3}\,\mathrm{GeV}^{-2}$, with μ_B being the Bohr magneton. The lower AM-CR graph, expectedly, shows only a weak dependence on the recoil energy.

In order to evaluate the total recoil cross section, it is necessary to determine the integration limits for E_R. Evidently, the theoretically possible minimum recoil energy is $E_R = 0$, meaning no scattering occurred and the electron acquires no kinetic energy. Additionally, this also represents the limiting case for the angle (36), namely $\theta = 90°$, at which no momentum transfer occurs. The recoil energy reaches its maximum when backscattering off of the incoming χ-particle, i.e. at $\theta = 0$. The maximal energy transfer is thus

$$E_R^{\max} = \frac{2m_e(E_\chi^2 - m_\chi^2)}{m_e(2E_\chi + m_e) + m_\chi^2}. \tag{44}$$

We have to be careful when considering the low recoil energy case, as the differential cross section diverges as $E_R \to 0$ for millicharge, MDM and EDM interactions (43a-43c). The AM and CR interactions (43d-43e) posses a finite cross section at $E_R = 0$. In order to evaluate total cross sections, especially for the divergent cases, care has to taken in finding appropriate screening conditions. These are dependent on the physical scattering environment that regularise the results, e.g. Debye screening. In our case the zero energy transfer divergence poses no issue, as a detector has a natural minimum energy threshold.

4.2 Dark Matter Non-Relativistic Self-Scattering

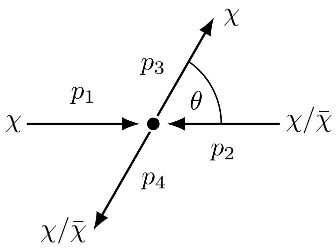

Figure 15: Sketch of the kinematics of the $\chi\chi$ or $\chi\bar{\chi}$ elastic scattering in the centre-of-momentum (CM) frame (CM) with corresponding momenta. The CM scattering angle of the χ-particles is denoted by θ in the diagram.

As previously discussed, it is also instructive to evaluate the $\chi\chi$, as well as the $\chi\bar{\chi}$, elastic scattering in the non-relativistic limit. $\bar{\chi}\bar{\chi}$ scattering is equivalent to $\chi\chi$ scattering for all EM form factors at tree level, which can be seen from the traces appearing when computing the matrix elements. Only tree level contributions of the same EM form factors will be considered here. Furthermore, the calculation of the differential cross section will be carried out in the centre-of-momentum (CM) frame of the χ-particles. The conventions and kinematics can be read off of Fig. 15. The four-momenta p_1, p_2, p_3, p_4 are such that $p_1 + p_2 = (E_{CM}, \vec{0})^{\mathrm{T}} = p_3 + p_4$, meaning that $\vec{p}_1 = -\vec{p}_2$, $\vec{p}_3 = -\vec{p}_4$ and $E_{CM} = E_1 + E_2 = E_3 + E_4$. In this case, the two scattering particles are identical, hence $E_1 = E_2$, $E_3 = E_3$ and $|\vec{p}_1| = |\vec{p}_2| = |\vec{p}_3| = |\vec{p}_4| = p_{CM}$ which implies

$$E_{CM} = 2E_i = 2\sqrt{m_\chi^2 + p_{CM}^2}, \tag{45}$$

where E_{CM} is the CM energy and p_{CM} is the CM momentum. We can use (45) to express the Mandelstam variables in term of the CM scattering angle θ and momentum p_{CM}:

$$s \coloneqq (p_1 + p_2)^2 = E_{CM}^2 = 4m_\chi^2 + 4p_{CM}^2, \tag{46a}$$

$$t \coloneqq (p_1 - p_3)^2 = -2p_{CM}^2(1 - \cos\theta), \tag{46b}$$

$$u \coloneqq (p_1 - p_4)^2 = -2p_{CM}^2(1 + \cos\theta). \tag{46c}$$

The focus on the momentum instead of the energy simplifies the computation of the non-relativistic limit. Instead of calculating the phase space integral directly, as previously done for $e^-\chi$ scattering (39), we use the Lorentz invariant, and thus reference frame independent, differential cross section for 2-to-2 scattering for incoming particles with masses m_1 and m_2 [62]:

$$\frac{d\sigma}{dt} = \frac{|\mathcal{M}|^2}{16\pi\lambda(s, m_1^2, m_2^2)}, \tag{47}$$

where $\lambda(s, m_1^2, m_2^2)$ is the Källén, or triangle, function $\lambda(x, y, z) = x^2 + y^2 + z^2 - 2xy - 2yz - 2xz$. Using the definitions from (46a-46c) yields

$$\frac{d\sigma}{d\cos\theta} = \frac{|\mathcal{M}|^2}{128\pi(m_\chi^2 + p_{CM}^2)}, \tag{48}$$

where $dt = 2p_{CM}^2 d\cos\theta$, since p_{CM} is a constant input parameter.

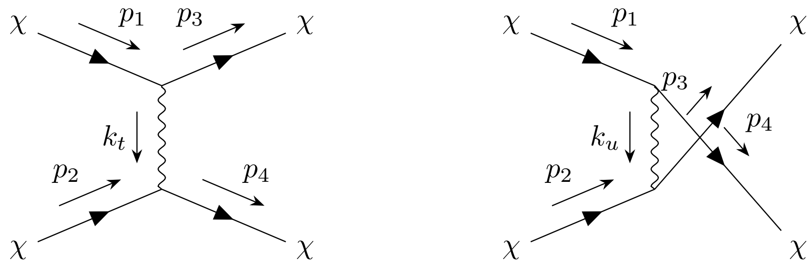

(a) t-channel

(b) u-channel

Figure 16: Elastic self-scattering of χ at tree level for both t-channel and u-channel.

First, we compute the differential cross section of $\chi\chi$ scattering in the non-relativistic (NR) limit by calculating the spin-summed matrix element $|\mathcal{M}|^2$ and inserting it into (48). App. D contains the full relativistic results for these matrix elements. Then $p_{CM} = m_\chi v/\sqrt{1 - v^2}$ is used and the NR limit is taken for small v, where v the CM velocity such that the relative velocity of the DM particles in the CM frame is $2v$. There are two diagrams that contribute to the $\chi\chi$ scattering amplitude at tree level, the t-channel and the u-channel, as seen in Fig. 16a and 16b respectively. Once again, Feynman gauge $\xi = 1$ is used when evaluating the matrix elements. The resulting non-relativistic differential cross section for $\chi\chi$ scattering in the CM frame, where the $\approx$ stands for the NR limit of small velocities v, are:

$$\left(\frac{d\sigma_{\chi\chi}}{d\cos\theta}\right)_{\varepsilon e} \approx \frac{\pi\varepsilon^4\alpha^2}{2m_\chi^2\sin^4\theta}\frac{1+v^2}{v^4}\left[1 + 3\cos^2\theta\right], \tag{49a}$$

$$\left(\frac{d\sigma_{\chi\chi}}{d\cos\theta}\right)_{\text{MDM}} \approx \frac{\mu_\chi^4 m_\chi^2}{4\pi}\left[3 + \frac{27 + \cos^2\theta}{8}v^4\right], \tag{49b}$$

$$\left(\frac{d\sigma_{\chi\chi}}{d\cos\theta}\right)_{\text{EDM}} \approx \frac{3d_\chi^4 m_\chi^2}{8\pi}\left[1 + 2v^2\right], \tag{49c}$$

$$\left(\frac{d\sigma_{\chi\chi}}{d\cos\theta}\right)_{\text{AM}} \approx \frac{a_\chi^4 m_\chi^6}{\pi}\left[\left(3 + \cos^2\theta\right)v^4 + 2\left(5 + \cos^2\theta\right)v^6\right], \tag{49d}$$

$$\left(\frac{d\sigma_{\chi\chi}}{d\cos\theta}\right)_{\text{CR}} \approx \frac{b_\chi^4 m_\chi^6}{2\pi}\left[\left(2 + 3\cos^2\theta\right)v^4 + \left(5 - \cos^2\theta\right)v^6\right], \tag{49e}$$

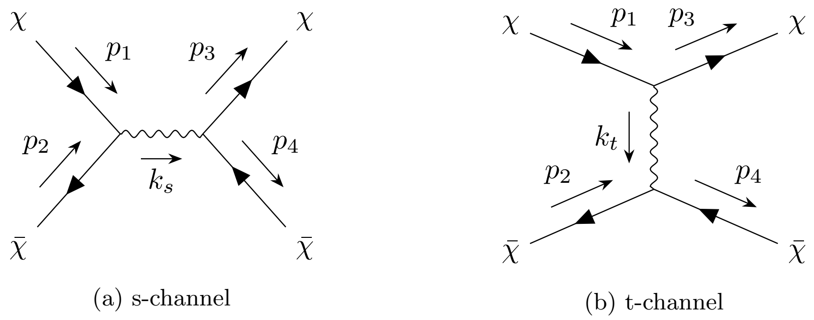

Figure 17: Elastic scattering of χ and $\bar{\chi}$ at tree level for both s-channel and t-channel.

Now, we move on to $\chi\bar{\chi}$ scattering. Here, the difference to $\chi\chi$ scattering at tree level is that instead of a u-channel contribution, $\chi\bar{\chi}$ scattering has an s-channel. The relevant s-channel and t-channel diagrams can be seen in Fig. 17a, 17b and respectively. The procedure is the same as for $\chi\chi$ scattering, again see App. D for the full relativistic result. This yields for the non-relativistic differential cross section of $\chi\bar{\chi}$ scattering in the CM frame:

$$\left(\frac{d\sigma_{\chi\bar{\chi}}}{d\cos\theta}\right)_{\varepsilon e} \approx \frac{\pi\varepsilon^4\alpha^2}{8m_\chi^2\sin^4\frac{\theta}{2}}\left[\frac{1}{v^4}+\frac{7\cos\theta-5}{2v^2}\right], \tag{50a}$$

$$\left(\frac{d\sigma_{\chi\bar{\chi}}}{d\cos\theta}\right)_{\mathrm{MDM}} \approx \frac{\mu_\chi^4 m_\chi^2}{8\pi}\left[7+\frac{7\cos\theta-5}{2}v^2\right], \tag{50b}$$

$$\left(\frac{d\sigma_{\chi\bar{\chi}}}{d\cos\theta}\right)_{\mathrm{EDM}} \approx \frac{3d_\chi^4 m_\chi^2}{8\pi}\left[1+2\left(1+\cos\theta\right)v^2\right], \tag{50c}$$

$$\left(\frac{d\sigma_{\chi\bar{\chi}}}{d\cos\theta}\right)_{\mathrm{AM}} \approx \frac{2a_\chi^4 m_\chi^6}{\pi}\left[\left(2\cos^2\theta-\cos\theta+1\right)v^4+\frac{\cos^3\theta+12\cos^2\theta-7\cos\theta-6}{2}v^6\right], \tag{50d}$$

$$\left(\frac{d\sigma_{\chi\bar{\chi}}}{d\cos\theta}\right)_{\mathrm{CR}} \approx \frac{b_\chi^4 m_\chi^6}{\pi}\left[6+\left(11+3\cos\theta\right)v^2\right]. \tag{50e}$$

Interestingly, while the full relativistic cross sections of $\chi\chi$ and $\chi\bar{\chi}$ scattering are related by the crossing symmetry of the s-channel 17a and u-channel 16b diagrams, as can be seen in App. D, their NR limits can be rather different. This is perhaps best illustrated by the CR interaction, as in this case, not even the velocity dependence matches between the two types of scattering, with the $\chi\bar{\chi}$ case having no dependence at lowest order, while $\chi\chi$ is behaving like $\mathcal{O}(v^4)$.

5 Dark Matter Particle Production by Electron Scattering

5.1 Kinematics and Four-Body Phase Space

The 2-to-2 cross sections (43b-43e) in the previous chapter will be used to calculate the detection cross section of χ particles at the sensor. These χ's will be produced by an electron beam hitting a beam dump. In order to calculate the production cross section of the χ at this target, we will need to evaluate a four-body phase space integral. The focus here will be the χ pair production process $N(p_1) + e(p_2) \to X(p_3) + e(p_4) + \chi(p_\chi) + \bar{\chi}(p_{\bar{\chi}})$, where N is a target nucleus with mass m_N, X is a hadronic final state with inclusive mass m_X, e are electrons with m_e, with χ and $\bar{\chi}$ being the new particle pair with mass m_χ. While the electron-electron scattering case will be used in the final calculation, it is still useful to derive the kinematics in full generality with regards to the second scattering partner. This allows for greater flexibility when further studying this model beyond the scope of this thesis. If we want to calculate the production cross section

$$d\sigma_{\text{prod}} = \frac{1}{4\sqrt{(p_1 \cdot p_2)^2 - m_N^2 m_e^2}} |\mathcal{M}(p_1, p_2 \to p_3, p_4, p_\chi, p_{\bar{\chi}})|^2 d\Pi_4(p_3, p_4, p_\chi, p_{\bar{\chi}}), \tag{51}$$

we need to integrate the four-body phase space of the final states

$$d\Pi_4(p_3, p_4, p_\chi, p_{\bar{\chi}}) = \prod_{i=3}^{6} \frac{d^3 p_i}{(2\pi)^3 2E_i} (2\pi)^4 \delta^{(4)} \left(p_1 + p_2 - \sum_{j=3}^{6} p_j \right), \tag{52}$$

where $5, 6 = \chi, \bar{\chi}$. To make the integration of this phase space tractable, a common method is phase space splitting, where the system is split into smaller subsystems. First, to introduce these subsystems one inserts full phase space integrals that evaluate to unity. There are countless possibilities to choose these subsystems, their frames and the Lorentz invariants to rewrite them in. Choosing the optimal set of frames/invariants is a non-trivial matter. For the purpose of this work, we seek a differential cross section that depends on the angle between the electron beam line and the particle χ (and not $\bar{\chi}$ a matter of convention), as well as on the energy of χ. The differential cross section expressed this way is suitable for further calculating the incoming particle flux onto the detector, as it has a finite angular aperture. After introducing these splittings, the original integral is transformed by choosing convenient reference frames for the subsystems.

With this in mind, we introduce the new four momenta of the subsystems $q_{4\bar{\chi}} := p_4 + p_{\bar{\chi}}$, as well as $q_{34\bar{\chi}} := p_3 + p_4 + p_{\bar{\chi}}$. While four outgoing momenta seemingly have 12 degrees of freedom (d.o.f.), this is reduced by four d.o.f. through energy-momentum conservation and by one d.o.f. through the redundancy of rotations around the incoming $\vec{p}_1 + \vec{p}_2$ axis [62]. In total, there are seven independent Lorentz invariants in a system with six four momenta. It turns out that, for our purposes, a convenient choice of are the five invariants

$$s_{4\bar{\chi}} := (p_4 + p_{\bar{\chi}})^2,\ s_{34\bar{\chi}} := (p_3 + p_4 + p_{\bar{\chi}})^2,\ t_{14} := (p_1 - p_4)^2,\ t_{2\chi} := (p_2 - p_\chi)^2,\ t_{13} := (p_1 - p_3)^2, \tag{53}$$

as well as the two scalar products $p_2 \cdot p_3$ and $p_3 \cdot p_4$. This is the same choice as [51]. Additionally, the four vector $q_{23\chi} = p_2 - p_3 - p_\chi$ will be used, which has the property

$$\begin{aligned} q_{23\chi}^2 := (p_2 - p_3 - p_\chi)^2 &= (p_4 + p_{\bar{\chi}} - p_1)^2 = m_N^2 + s_{4\bar{\chi}} - 2p_1 \cdot (p_4 + p_{\bar{\chi}}) \\ &= m_N^2 + s_{4\bar{\chi}} - 2p_1 \cdot (p_1 + p_2 - p_3 - p_\chi) = s_{4\bar{\chi}} + t_{2\chi} - s_{34\bar{\chi}} + 2p_1 \cdot p_3 \\ &= m_N^2 + m_X^2 + s_{4\bar{\chi}} + t_{2\chi} - s_{34\bar{\chi}} - t_{13}. \end{aligned} \tag{54}$$

As discussed previously, we will now split the four-body phase space (52) by integrating out the original external momenta by inserting the new variables, effectively making a Lorentz invariant substitution. The following integrals will be inserted into the phase space integral:

$$1 = \int \frac{d^4 q_{4\bar{\chi}}}{(2\pi)^4} (2\pi)^4 \delta^{(4)}(q_{4\bar{\chi}} - p_4 - p_{\bar{\chi}}) \Theta(q^0_{4\bar{\chi}}), \tag{55a}$$

$$1 = \int \frac{d^4 q_{34\bar{\chi}}}{(2\pi)^4} (2\pi)^4 \delta^{(4)}(q_{34\bar{\chi}} - p_3 - p_4 - p_{\bar{\chi}}) \Theta(q^0_{34\bar{\chi}}), \tag{55b}$$

$$1 = \int \frac{ds_{4\bar{\chi}}}{2\pi} 2\pi\delta(s_{4\bar{\chi}} - q^2_{4\bar{\chi}}), \tag{55c}$$

$$1 = \int \frac{ds_{34\bar{\chi}}}{2\pi} 2\pi\delta(s_{34\bar{\chi}} - q^2_{34\bar{\chi}}), \tag{55d}$$

where Θ is the Heaviside step function. These are subsequently simplified pairwise by expanding the delta distribution and integrating out the step functions:

$$\begin{aligned} 1 &= \int \frac{ds_{4\bar{\chi}}}{2\pi} \frac{d^4 q_{4\bar{\chi}}}{(2\pi)^4} (2\pi)^4 \delta^{(4)}(q_{4\bar{\chi}} - p_4 - p_{\bar{\chi}}) \Theta(q^0_{4\bar{\chi}}) 2\pi\delta\big(s_{4\bar{\chi}} - q^2_{4\bar{\chi}}\big) \\ &= \int \frac{ds_{4\bar{\chi}}}{2\pi} \frac{d^3 q_{4\bar{\chi}}}{(2\pi)^3} dq^0_{4\bar{\chi}} (2\pi)^4 \delta^{(4)}(q_{4\bar{\chi}} - p_4 - p_{\bar{\chi}}) \Theta(q^0_{4\bar{\chi}}) \delta\big(s_{4\bar{\chi}} + \vec{q}^{\,2}_{4\bar{\chi}} - (q^0_{4\bar{\chi}})^2\big) \\ &= \int \frac{ds_{4\bar{\chi}}}{2\pi} \frac{d^3 q_{4\bar{\chi}}}{(2\pi)^3 2E_{4\bar{\chi}}} (2\pi)^4 \delta^{(4)}(q_{4\bar{\chi}} - p_4 - p_{\bar{\chi}}), \end{aligned} \tag{56}$$

where $E^2_{4\bar{\chi}} = (q^0_{4\bar{\chi}})^2 = s_{4\bar{\chi}} + \vec{q}^{\,2}_{4\bar{\chi}}$ is used in the last equality. This implements the on-shell condition for the introduced momentum $q_{4\bar{\chi}}$. Likewise, for the second set of integrals with $E^2_{34\bar{\chi}} = (q^0_{34\bar{\chi}})^2 = s_{34\bar{\chi}} + \vec{q}^{\,2}_{34\bar{\chi}}$ the result is

$$1 = \int \frac{ds_{34\bar{\chi}}}{2\pi} \frac{d^3 q_{34\bar{\chi}}}{(2\pi)^3 2E_{34\bar{\chi}}} (2\pi)^4 \delta^{(4)}(q_{34\bar{\chi}} - p_3 - q_{4\bar{\chi}}). \tag{57}$$

Now we can insert the integrals (56) and (57) into the four-body phase space (52) and try to reduce the integration to the desired Lorentz invariants. In the notation used here, an expression of the form $E_{ab...}$ is always shorthand for the zeroth component of the four momentum $p_{ab...}$, regardless of it being on-shell.

5.1.1 First Subsystem of Phase Space Splitting

The first subsystem of (52) will be integrated by choosing a particular frame $d\Phi(q_{4\bar{\chi}})$. A convenient choice is the rest frame of $q_{4\bar{\chi}}$ where $\vec{q}_{4\bar{\chi}} = 0,\ E_{4\bar{\chi}} = \sqrt{s_{4\bar{\chi}}}$. All the resulting variables of this subsystem are thus implied to be in that frame. The integration is then be conducted by expanding the delta function using the positive root P_4 of the equation inside it. This yields, with $E_{\bar{\chi}}(\vec{p}_4) = \sqrt{m^2_{\chi} + \vec{p}^{\,2}_4}$, the following:

$$\begin{aligned} \int d\Phi(q_{4\bar{\chi}}) &= \int \frac{d^3 p_4}{(2\pi)^3 2E_4} \frac{d^3 p_{\bar{\chi}}}{(2\pi)^3 2E_{\bar{\chi}}} (2\pi)^4 \delta^{(4)}(q_{4\bar{\chi}} - p_4 - p_{\bar{\chi}}) \\ &= \int \frac{d^3 p_4}{(2\pi)^3 2E_4} \frac{d^3 p_{\bar{\chi}}}{(2\pi)^3 2E_{\bar{\chi}}} (2\pi)^4 \delta\big(\sqrt{s_{4\bar{\chi}}} - E_4 - E_{\bar{\chi}}\big) \delta^{(3)}(\vec{p}_4 + \vec{p}_{\bar{\chi}}) \\ &= \int \frac{d^3 p_4}{(2\pi)^2 2E_4} \frac{1}{2E_{\bar{\chi}}(\vec{p}_4)} \delta\Big(\sqrt{s_{4\bar{\chi}}} - \sqrt{m^2_{\chi} + \vec{p}^{\,2}_4} - \sqrt{m^2_e + \vec{p}^{\,2}_4}\Big) \\ &= \int \frac{|\vec{p}_4|^2 d|\vec{p}_4|}{(2\pi)^2} \frac{d\cos\theta_4}{E_{\bar{\chi}}(\vec{p}_4)} \frac{d\varphi_4}{E_4} \frac{E_4 E_{\bar{\chi}}(\vec{p}_4)}{P_4 \sqrt{s_{4\bar{\chi}}}} \delta(|\vec{p}_4| - P_4) \\ &= \int \frac{d\cos\theta_4}{2\pi} \frac{d\varphi_4}{2\pi} \frac{P_4}{4\sqrt{s_{4\bar{\chi}}}}. \end{aligned} \tag{58}$$

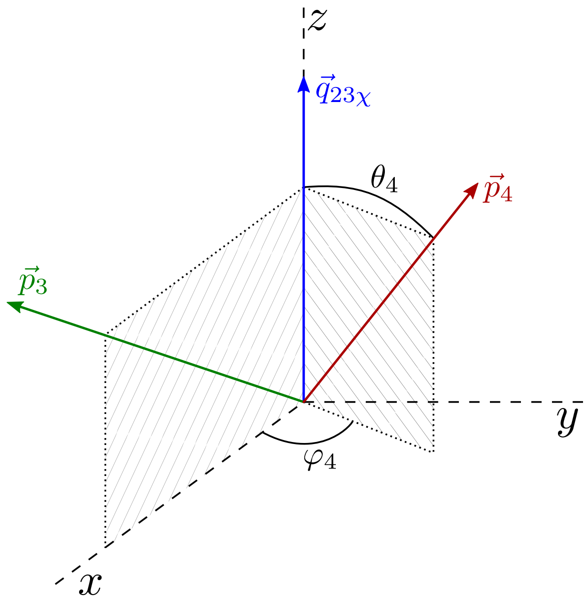

Figure 18: Illustration of the subsystem in the rest frame of $q_{4\bar{\chi}}$ with the angles θ_4 and φ_4.

As will be seen during the course of the calculation, the explicit form of P_4 is not important. Now, in this frame $\vec{q}_{4\bar{\chi}} = \vec{p}_4 + \vec{p}_{\bar{\chi}} = 0$, this amounts to $\vec{p}_1 + \vec{p}_2 - \vec{p}_3 - \vec{p}_\chi = \vec{p}_1 + \vec{q}_{23\chi} = 0$, and the subsystem can be taken as consisting of $\{q_{4\bar{\chi}}, q_{23\chi}, p_3, p_4\}$. Since we have already decided to integrate in the rest frame of $q_{4\bar{\chi}} = (\sqrt{s_{4\bar{\chi}}}, \vec{0})^{\mathrm{T}}$, it is possible to choose freely that $\vec{q}_{23\chi}$ is parallel to the z-axis and that $\vec{p}_3$ lies in the xz-plane, as shown in Fig. 18. The next step is to re-express the angle between $\vec{p}_4$ and $\vec{q}_{23\chi}$, given by $\vec{p}_4 \cdot \vec{q}_{23\chi} = P_4\sqrt{\vec{q}^{\,2}_{23\chi}}\cos\theta_4$, in terms of an invariant. The invariant we use is t_{14} (53), which is related to $\cos\theta_4$ by

$$\begin{aligned} t_{14} &= (p_1 - p_4)^2 = m_N^2 + m_e^2 - 2p_1 \cdot p_4 = m_N^2 + m_e^2 - 2E_1E_4 + 2\vec{p}_1 \cdot \vec{p}_4 \\ &= m_N^2 + m_e^2 - 2E_1E_4 - 2\vec{q}_{23\chi} \cdot \vec{p}_4 \\ &= m_N^2 + m_e^2 - 2E_1E_4 - 2P_4\sqrt{\vec{q}^{\,2}_{23\chi}}\cos\theta_4. \end{aligned} \tag{59}$$

The integral substitution $dt_{14} = -2P_4\sqrt{\vec{q}^{\,2}_{23\chi}}\,d\cos\theta_4$ in (58) yields

$$\int d\Phi(q_{4\bar{\chi}}) = \int \frac{dt_{14}}{2\pi}\frac{d\varphi_4}{2\pi}\frac{1}{-2P_4\sqrt{\vec{q}^{\,2}_{23\chi}}}\frac{P_4}{4\sqrt{s_{4\bar{\chi}}}} = -\int \frac{dt_{14}}{2\pi}\frac{d\varphi_4}{2\pi}\frac{1}{8\sqrt{s_{4\bar{\chi}}\vec{q}^{\,2}_{23\chi}}}, \tag{60}$$

where the negative sign comes from the change in the integration limits. There is still the magnitude of a 3-vector under the integral (60), that we want to express using only invariants. Recalling that $\vec{q}_{4\bar{\chi}} = 0$ leads to $q_{4\bar{\chi}} \cdot q_{23\chi} = \sqrt{s_{4\bar{\chi}}}E_{23\chi}$, and subsequently expanding $\vec{q}_{23\chi}$, thus results in:

$$\begin{aligned} \vec{q}^{\,2}_{23\chi} &= \frac{1}{s_{4\bar{\chi}}}(q_{4\bar{\chi}} \cdot q_{23\chi})^2 - q^2_{23\chi} = \frac{1}{4s_{4\bar{\chi}}}\left[4(q_{4\bar{\chi}} \cdot q_{23\chi})^2 - 4s_{4\bar{\chi}}q^2_{23\chi}\right] \\ &= \frac{1}{4s_{4\bar{\chi}}}\left[(m_N^2 - s_{4\bar{\chi}} - q^2_{23\chi})^2 - 4s_{4\bar{\chi}}q^2_{23\chi}\right] \\ &= \frac{1}{4s_{4\bar{\chi}}}\lambda(s_{4\bar{\chi}}, m_N^2, q^2_{23\chi}) \end{aligned} \tag{61}$$

by using $4(q_{4\bar{\chi}}\cdot q_{23\chi})^2 = ((q_{4\bar{\chi}}-q_{23\chi})^2 - s_{4\bar{\chi}} - q_{23\chi}^2)^2 = (p_1^2 - s_{4\bar{\chi}} - q_{23\chi}^2)^2 = (m_N^2 - s_{4\bar{\chi}} - q_{23\chi}^2)^2$. Inserting the result from (61) into the integral (60) yields

$$d\Phi(q_{4\bar{\chi}}) = -\int \frac{dt_{14}}{2\pi}\frac{d\varphi_4}{2\pi}\frac{1}{4}\lambda^{-1/2}(s_{4\bar{\chi}}, m_N^2, q_{23\chi}^2). \tag{62}$$

Lastly, we want to express the azimuthal angle φ_4 between the planes spanned by $(\vec{q}_{23\chi}, \vec{p}_3)$ and $(\vec{q}_{23\chi}, \vec{p}_4)$ in the reference frame $\vec{q}_{4\bar{\chi}} = 0$ using Lorentz invariant quantities. Since $q_{4\bar{\chi}} = p_1 + q_{23\chi}$, the most convenient choice, in this case, is the scalar product $p_3 \cdot p_4$, which is related to this angle via [62]

$$\begin{aligned}
p_3\cdot p_4 &= \frac{(q_{4\bar{\chi}}\cdot p_3)G(q_{4\bar{\chi}}, q_{23\chi}; q_{23\chi}, p_4)}{-\Delta_2(q_{4\bar{\chi}}, q_{23\chi})} - \frac{(q_{23\chi}\cdot p_3)G(q_{4\bar{\chi}}, q_{23\chi}; q_{4\bar{\chi}}, p_4)}{-\Delta_2(q_{4\bar{\chi}}, q_{23\chi})} \\
&\quad - \frac{\sqrt{\Delta_3(q_{4\bar{\chi}}, q_{23\chi}, p_3)\Delta_3(q_{4\bar{\chi}}, q_{23\chi}, p_4)}}{-\Delta_2(q_{4\bar{\chi}}, q_{23\chi})}\cos\varphi_4 \\
&= \frac{1}{-\Delta_2(p_1, q_{23\chi})}\Big\{\Big[(p_1\cdot p_3) + (q_{23\chi}\cdot p_3)\Big]G(p_1, q_{23\chi}; q_{23\chi}, p_4) \\
&\quad - (q_{23\chi}\cdot p_3)\Big[G(p_1, q_{23\chi}; q_{23\chi}, p_4) + G(p_1, q_{23\chi}; p_1, p_4)\Big] \\
&\quad - \sqrt{\Delta_3(p_1, q_{23\chi}, p_3)\Delta_3(p_1, q_{23\chi}, p_4)}\cos\varphi_4\Big\},
\end{aligned} \tag{63}$$

where Δ_2 is the Gram determinant, G is referred to in [62] as asymmetric Gram determinant, and we used the alternating property of the determinant as well as its multilinearity. Importantly, these are matrices of scalar products, making their determinants also Lorentz invariant. Finally, the relation between the invariant $p_3 \cdot p_4$ and the angle φ_4 becomes

$$\begin{aligned}
p_3\cdot p_4 &= \frac{(p_1\cdot p_3)G(p_1, q_{23\chi}; q_{23\chi}, p_4)}{-\Delta_2(p_1, q_{23\chi})} - \frac{(q_{23\chi}\cdot p_3)G(p_1, q_{23\chi}; p_1, p_4)}{-\Delta_2(p_1, q_{23\chi})} \\
&\quad - \frac{\sqrt{\Delta_3(p_1, q_{23\chi}, p_3)\Delta_3(p_1, q_{23\chi}, p_4)}}{-\Delta_2(p_1, q_{23\chi})}\cos\varphi_4.
\end{aligned} \tag{64}$$

5.1.2 Second Subsystem of Phase Space Splitting

The second subsystem $d\Phi(q_{34\bar{\chi}})$ of (52) will be treated in the same manner as the first one above. The difference being here, that the integration will take place over one original momentum, p_3, and one composite momentum, $q_{4\bar{\chi}}$. We will use the rest frame of $q_{34\bar{\chi}}$ where $\vec{q}_{34\bar{\chi}} = 0$, i.e. $\vec{q}_{4\bar{\chi}} + \vec{p}_3 = 0$ and $E_{34\bar{\chi}} = \sqrt{s_{34\bar{\chi}}}$. All variables derived at the end of this treatment are again understood to be in this rest frame. Similar to the first subsystem, the integration will be conducted by expanding the delta distribution using the positive root P_3 of the equation inside it:

$$\int d\Phi(q_{34\bar{\chi}}) = \int \frac{d^3 q_{4\bar{\chi}}}{(2\pi)^3 2E_{4\bar{\chi}}}\frac{d^3 p_3}{(2\pi)^3 2E_3}(2\pi)^4\delta^{(4)}(q_{34\bar{\chi}} - q_{4\bar{\chi}} - p_3) = \int \frac{d\cos\theta_3}{2\pi}\frac{d\varphi_3}{2\pi}\frac{P_3}{4\sqrt{s_{34\bar{\chi}}}}. \tag{65}$$

In the frame where $\vec{q}_{34\bar{\chi}} = \vec{p}_3 + \vec{p}_4 + \vec{p}_{\bar{\chi}} = 0$, which leads to $\vec{p}_1 + \vec{p}_2 - \vec{p}_\chi = \vec{p}_1 + \vec{q}_{2\chi} = 0$, we take the subsystem as consisting of $\{q_{34\bar{\chi}}, q_{2\chi}, p_2, p_3\}$. In the rest frame of $q_{34\bar{\chi}} = (\sqrt{s_{34\bar{\chi}}}, \vec{0})$, $\vec{q}_{2\chi}$ can be taken parallel to the z-axis and $\vec{p}_2$ to lie in the xz-plane, as seen in Fig. 19, without changing the kinematics.

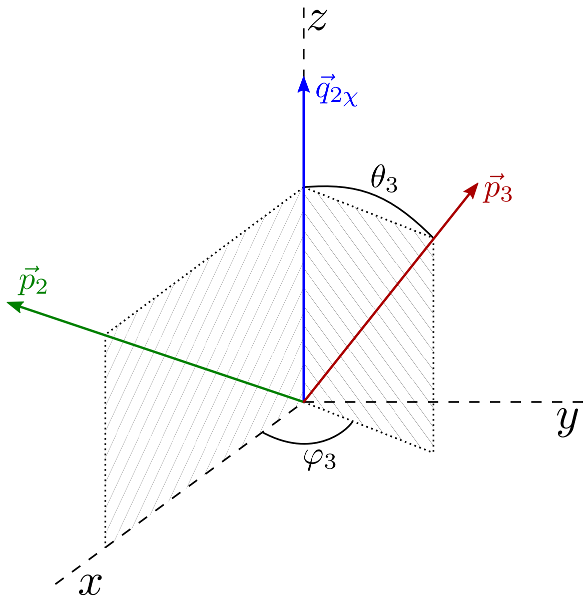

Figure 19: Illustration of the subsystem in the rest frame of $q_{34\bar{\chi}}$ with the angles θ_3 and φ_3.

Now we want to write the angle enclosed by $\vec{p}_3$ and $\vec{q}_{2\chi}$, given through $\vec{p}_3 \cdot \vec{q}_{2\chi} = P_3\sqrt{\vec{q}^{\,2}_{2\chi}}\cos\theta_3$, in terms of the invariant t_{13} (53). Expanding t_{13} yields

$$t_{13} = m_N^2 + m_\chi^2 - 2E_1E_3 - 2P_3\sqrt{\vec{q}^{\,2}_{2\chi}}\cos\theta_3. \tag{66}$$

Using this result, the integral (65) can be transformed with $dt_{13} = -2P_3\sqrt{\vec{q}^{\,2}_{2\chi}}d\cos\theta_3$ into

$$\int d\Phi(q_{34\bar{\chi}}) = -\int \frac{dt_{13}}{2\pi}\frac{d\varphi_3}{2\pi}\frac{1}{8\sqrt{s_{34\bar{\chi}}\vec{q}^{\,2}_{2\chi}}}. \tag{67}$$

The sign in (67) is again due to the change of the integration limits because of the substitution. Next we eliminate the 3-momentum magnitude left inside the integral. Using $\vec{q}_{34\bar{\chi}} = 0$, which amounts to $q_{34\bar{\chi}} \cdot q_{2\chi} = \sqrt{s_{34\bar{\chi}}}E_{2\chi}$, the result

$$\vec{q}^{\,2}_{2\chi} = \frac{1}{4s_{34\bar{\chi}}}\lambda(s_{34\bar{\chi}}, m_N^2, t_{2\chi}) \tag{68}$$

is derived in the same way as done in (61). Using the result (68), the final form of the integral in (67) is

$$\int d\Phi(q_{34\bar{\chi}}) = -\int \frac{dt_{13}}{2\pi}\frac{d\varphi_3}{2\pi}\frac{1}{4}\lambda^{-1/2}(s_{34\bar{\chi}}, m_N^2, t_{2\chi}). \tag{69}$$

Finally, we want to relate the azimuthal angle φ_3 between the planes spanned by $(\vec{p}_2 - \vec{p}_\chi, \vec{p}_2)$ and $(\vec{p}_2 - \vec{p}_\chi, \vec{p}_3)$ in the reference frame $\vec{q}_{34\bar{\chi}} = 0$ to the scalar product $p_2 \cdot p_3$ the same way as in (63). Consequently, the relation between the invariant $p_2 \cdot p_3$ and the angle φ_3 is

$$\begin{aligned} p_2 \cdot p_3 = {} & \frac{(p_1\cdot p_2)G(p_1, p_2 - p_\chi; p_2 - p_\chi, p_3)}{-\Delta_2(p_1, p_2 - p_\chi)} - \frac{(m_e^2 - p_2\cdot p_\chi)G(p_1, p_2 - p_\chi; p_1, p_3)}{-\Delta_2(p_1, p_2 - p_\chi)} \\ & - \frac{\sqrt{\Delta_3(p_1, p_2 - p_\chi, p_2)\Delta_3(p_1, p_2 - p_\chi, p_3)}}{-\Delta_2(p_1, p_2 - p_\chi)}\cos\varphi_3. \end{aligned} \tag{70}$$

5.1.3 Full Phase Space Integral

Now it is possible to combine both subsystems discussed above to bring the phase space integral into its final form. Combining (62) and (67) together with the remaining terms from (52) yields

$$\begin{aligned}\int d\Pi_4(p_3,p_4,p_\chi,p_{\bar\chi}) = \int &\frac{d^3p_\chi}{(2\pi)^3 2E_\chi}\frac{ds_{34\bar\chi}}{2\pi}\frac{d^3q_{34\bar\chi}}{(2\pi)^3 2E_{34\bar\chi}}\frac{ds_{4\bar\chi}}{2\pi}(2\pi)^4\delta^{(4)}(p_1+p_2-p_\chi-q_{34\bar\chi})\\ &\times\frac{dt_{14}}{2\pi}\frac{d\varphi_4}{2\pi}\frac{1}{4}\lambda^{-1/2}(s_{4\bar\chi},m_N^2,q_{23\chi}^2)\frac{dt_{13}}{2\pi}\frac{d\varphi_3}{2\pi}\frac{1}{4}\lambda^{-1/2}(s_{34\bar\chi},m_N^2,t_{2\chi}).\end{aligned} \tag{71}$$

In order to reduce the integration to just Lorentz invariants, $q_{34\bar\chi}$ and p_χ need to be integrated out. This will be done in the rest frame of the target $p_1 = (m_N,\vec 0)^{\mathrm T}$, i.e. the lab frame, where $\vec p_2$ can be taken parallel to the z-axis:

$$\begin{aligned}&\int\frac{d^3p_\chi}{(2\pi)^3 2E_\chi}\frac{d^3q_{34\bar\chi}}{(2\pi)^3 2E_{34\bar\chi}}(2\pi)^4\delta^{(4)}(p_1+p_2-p_\chi-q_{34\bar\chi})\\ =&\int\frac{d^3p_\chi}{(2\pi)^2 2E_\chi}\frac{d^3q_{34\bar\chi}}{2E_{34\bar\chi}}\delta^{(3)}\left(\vec q_{34\bar\chi}-(\vec p_2-\vec p_\chi)\right)\\ &\times\delta\left(m_N+\sqrt{t_{2\chi}+(\vec p_2-\vec p_\chi)^2}-\sqrt{s_{34\bar\chi}+\vec q_{34\bar\chi}^{\,2}}\right)\\ =&\int\frac{d^3p_\chi}{(2\pi)^2 2E_\chi}\frac{1}{2E_{34\bar\chi}(\vec p_2-\vec p_\chi)}\delta\left(m_N+\sqrt{t_{2\chi}+(\vec p_2-\vec p_\chi)^2}-\sqrt{s_{34\bar\chi}+(\vec p_2-\vec p_\chi)^2}\right).\end{aligned} \tag{72}$$

Next, we want to integrate the p_χ out and transform the integral using $\vec p_\chi \longrightarrow \vec q_{2\chi} \coloneqq \vec p_2-\vec p_\chi$ and $t_{2\chi}=\vec q_{2\chi}^{\,2}$. This Lorentz invariant substitution is implemented by inserting the following integral, that evaluates to unity:

$$\begin{aligned}1 &= \int\frac{d^4q_{2\chi}}{(2\pi)^4}\frac{dt_{2\chi}}{2\pi}(2\pi)^4\delta^{(4)}(q_{2\chi}-p_2+p_\chi)\Theta(q_{2\chi}^0)(2\pi)\delta(t_{2\chi}-q_{2\chi}^2)\\ &= \int\frac{d^3q_{2\chi}}{2E_{2\chi}}dt_{2\chi}\delta^{(3)}(\vec q_{2\chi}-\vec p_2+\vec p_\chi)\delta(E_{2\chi}-E_2+E_\chi).\end{aligned} \tag{73}$$

Importantly, because $\vec p_2$ is parallel to the z-axis, the integration over the azimuthal angle φ_χ is invariant under this substitution, and it is possible to identify $d\varphi_{2\chi} = d\varphi_\chi$. After inserting (73) into (72) and resolving the delta function using its positive root $P_{2\chi}$, the integral becomes

$$\begin{aligned}&\int\frac{d^3p_\chi}{(2\pi)^2 2E_\chi}\frac{d^3q_{2\chi}}{2E_{2\chi}}\frac{dt_{2\chi}}{2E_{34\bar\chi}(q_{2\chi})}\delta\left(m_N+\sqrt{t_{2\chi}+(\vec p_2-\vec p_\chi)^2}-\sqrt{s_{34\bar\chi}+(\vec p_2-\vec p_\chi)^2}\right)\\ &\quad\times\delta^{(3)}(\vec q_{2\chi}-\vec p_2+\vec p_\chi)\delta(E_{2\chi}-E_2+E_\chi)\\ =&\int\frac{d^3q_{2\chi}}{(2\pi)^2 4E_\chi(q_{2\chi})E_{2\chi}}\frac{dt_{2\chi}}{2E_{34\bar\chi}(q_{2\chi})}\delta(E_{2\chi}-E_2+E_\chi)\delta\left(m_N+\sqrt{t_{2\chi}+\vec q_{2\chi}^{\,2}}-\sqrt{s_{34\bar\chi}+\vec q_{2\chi}^{\,2}}\right)\\ =&\int\frac{d\cos\theta_{2\chi}}{2\pi}\frac{d\varphi_\chi}{2\pi}\frac{|\vec q_{2\chi}|^2 d|\vec q_{2\chi}|}{4E_\chi(q_{2\chi})E_{2\chi}}\frac{dt_{2\chi}}{2E_{34\bar\chi}(q_{2\chi})}\delta(E_{2\chi}-E_2+E_\chi)\delta(|\vec q_{2\chi}|-P_{2\chi})\frac{E_{2\chi}E_{34\bar\chi}(q_{2\chi})}{P_{2\chi}m_N}\\ =&\int\frac{d\cos\theta_{2\chi}}{2\pi}\frac{d\varphi_\chi}{2\pi}\frac{dt_{2\chi}}{4E_\chi(q_{2\chi})}\frac{P_{2\chi}}{2m_N}\delta\left(E_{2\chi}-E_2+\sqrt{m_\chi^2+(\vec q_{2\chi}-\vec p_2)^2}\right),\end{aligned} \tag{74}$$

with $E_{34\bar\chi}(q_{2\chi})=\sqrt{s_{34\bar\chi}+(\vec p_2-\vec p_\chi)^2}$ and $E_\chi(q_{2\chi})=\sqrt{m_\chi^2+(\vec p_2-\vec p_\chi)^2}$. The azimuthal angle φ_χ can just be integrated out, as the problem has a rotational symmetry around the beam line of the incoming electron p_2. Additionally, we want to expand the remaining delta function using the solution $c_{2\chi}$. It is then possible to integrate over $\cos\theta_{2\chi}$. This yields

$$\begin{aligned}
&\int \frac{d\cos\theta_{2\chi}}{2\pi}\frac{d\varphi_\chi}{2\pi}\frac{dt_{2\chi}}{4E_\chi(q_{2\chi})}\frac{P_{2\chi}}{2m_N}\delta\left(E_{2\chi}-E_2+\sqrt{m_\chi^2+(\vec{q}_{2\chi}-\vec{p}_2)^2}\right)\\
=&\int \frac{d\cos\theta_{2\chi}}{2\pi}\frac{dt_{2\chi}}{4E_\chi(q_{2\chi})}\frac{P_{2\chi}}{2m_N}\delta(\cos\theta_{2\chi}-c_{2\chi})\frac{E_\chi(q_{2\chi})}{P_{2\chi}|\vec{p}_2|}\\
=&\int \frac{dt_{2\chi}}{2\pi}\frac{1}{8|\vec{p}_2|m_N}\\
=&\int \frac{dt_{2\chi}}{2\pi}\frac{1}{2}|J|,
\end{aligned} \tag{75}$$

where $|J|$ is the Jacobian of the integral transformation

$$\frac{dE_\chi d\cos\theta_\chi}{ds_{34\bar{\chi}}dt_{2\chi}} = \frac{|J|}{|\vec{p}_\chi|} = \frac{1}{4|\vec{p}_2||\vec{p}_\chi|m_N}. \tag{76}$$

This definition is chosen in a manner to facilitate its cancellation later in the calculation. Finally, combining (75) with (62) and (69) gives us the full phase space in terms of the 7 Lorentz invariants previously chosen

$$\frac{d\Pi_4}{ds_{34\bar{\chi}}dt_{2\chi}} = ds_{4\bar{\chi}}dt_{13}dt_{14}\frac{d\varphi_3}{2\pi}\frac{d\varphi_4}{2\pi}\frac{|J|}{(4\pi)^5}\lambda^{-1/2}(s_{4\bar{\chi}},m_N^2,q_{23\chi}^2)\lambda^{-1/2}(s_{34\bar{\chi}},m_N^2,t_{2\chi}). \tag{77}$$

5.1.4 Integration Limits for Dark Matter Production

After reducing the four-body phase space by integrating out the redundant degrees of freedom, we are interested in the physical region of the remaining seven Lorentz invariants. Namely, the integration limits of $s_{34\bar{\chi}}, s_{4\bar{\chi}}, t_{2\chi}, t_{13}, t_{14}, \varphi_3, \varphi_4$. In order to determine these limits, we examine the invariants in the frames used previously to reduce the integration. The limits are then calculated by rewriting them consecutively in terms of input parameters and already determined integration regions. Firstly, the limits of the two azimuthal angles are obvious from their definition:

$$\varphi_3 \in [0,2\pi),\ \ \varphi_4 \in [0,2\pi). \tag{78}$$

Next, we look at $s_{34\bar{\chi}} = (p_3+p_4+p_{\bar{\chi}})^2$. Its minimal value is, evidently, equivalent to the sum of the masses of the constituent momenta $(m_X+m_e+m_\chi)^2$. The maximum value is derived in the centre of mass (CM) frame of the incoming momenta $\vec{p_1}+\vec{p_2}=0$ with CM energy $s=(p_1+p_2)^2$. This results in

$$\sqrt{s} = E_\chi + E_{34\bar{\chi}} \ \Rightarrow\ \sqrt{s_{34\bar{\chi}}+\left|\vec{q}_{34\bar{\chi}}\right|^2} = \sqrt{s}-\sqrt{m_\chi^2+\left|\vec{p}_\chi\right|^2}. \tag{79}$$

The value of $s_{34\bar{\chi}}$ is maximal when the momentum $\vec{p}_\chi$ on the RHS of (79) is zero. But in the CM frame $\left|\vec{q}_{34\bar{\chi}}\right| = \left|\vec{p}_\chi\right|$, therefore, when $\vec{p}_\chi=0$ then $\vec{q}_{34\bar{\chi}}=0$. This can also be understood intuitively, as $\sqrt{s}$ is the total amount of energy available and has to be distributed to both the subsystem $\{p_3,p_4,p_{\bar{\chi}}\}$ and p_χ. Thus, in order to have the maximum amount of this energy allocated to $\{p_3,p_4,p_{\bar{\chi}}\}$, p_χ must gain the least energy possible, i.e. χ must be at rest. In summary, the integration limits of $s_{34\bar{\chi}}$ are

$$(m_X+m_e+m_\chi)^2 \le s_{34\bar{\chi}} \le (\sqrt{s}-m_\chi)^2. \tag{80}$$

The limits of the invariant $s_{4\bar{\chi}} = (p_4+p_{\bar{\chi}})^2$ are calculated in the rest frame of $q_{4\bar{\chi}}$. The minimum value can again be readily determined by the masses of the involved particles, namely $(m_e+m_\chi)^2$. The upper limit we identify using the value of $s_{34\bar{\chi}} = s_{4\bar{\chi}} + m_X^2 + 2E_3\sqrt{s_{4\bar{\chi}}}$. Solving this equation for $\sqrt{s_{4\bar{\chi}}}$, and only considering the positive (physical) solution, yields

$$\sqrt{s_{4\bar{\chi}}} = -E_3 + \sqrt{E_3^2 - m_X^2 + s_{34\bar{\chi}}}. \tag{81}$$

From (81) it becomes apparent that $s_{4\bar{\chi}}$ is maximal when E_3 is minimal, i.e. $E_3 = m_X$, for any given value of $s_{34\bar{\chi}}$, keeping in mind that $s_{34\bar{\chi}}$ is strictly positive and strictly larger than m_X. This gives the upper bound for the value of $s_{4\bar{\chi}}$, and thus, $s_{4\bar{\chi}}$ has the the following limits

$$(m_e + m_\chi)^2 \leq s_{4\bar{\chi}} \leq (\sqrt{s_{34\bar{\chi}}} - m_X)^2. \tag{82}$$

Now we move on to the momentum transfer invariants, starting with

$$t_{2\chi} = (p_2 - p_\chi)^2 = m_e^2 + m_\chi^2 - 2E_2E_\chi + 2|\vec{p}_2||\vec{p}_\chi|\cos\theta_\chi \tag{83}$$

in the CM frame of the incoming momenta, where $\vec{p_1} + \vec{p_2} = 0$. Evidently, the limits of $t_{2\chi}$ are given by the extremal values of $\cos\theta_{2\chi}$, namely ± 1. In order to express these bounds in parameters and other invariants, we apply the same method to derive the magnitude of the three-momenta, as used previously in the section on the four-body phase space integral (61) and (68). Using that $\vec{p_1} + \vec{p_2} = 0$, leads to $(p_1 + p_2) \cdot p_2 = \sqrt{s}E_2$. Expanding this gives

$$\begin{aligned}
\vec{p}_2^{\,2} &= \frac{1}{4s}\left\{4\big[(p_1+p_2)\cdot p_2\big]^2 - 4sp_2^2\right\} = \frac{1}{4s}\left\{4[p_1\cdot p_2 + m_e^2]^2 - 4sm_e^2\right\} \\
&= \frac{1}{4s}\left\{4\left[\frac{1}{2}(s - m_N^2 - m_e^2) + m_e^2\right]^2 - 4sm_e^2\right\} = \frac{1}{4s}\left\{[s - m_N^2 + m_e^2]^2 - 4sm_e^2\right\} \\
&= \frac{1}{4s}\lambda(s, m_N^2, m_e^2).
\end{aligned} \tag{84}$$

Similarly, the other 3-momentum magnitude is derived as

$$\vec{p}_\chi^{\,2} = \frac{1}{4s}\lambda(s_{34\bar{\chi}}, s, m_\chi^2). \tag{85}$$

Then we expand the energy term in the invariant (83) and take care of the sign, arising due to the square root inside them, such that the whole expression is positive, meaning physical, as following

$$\begin{aligned}
E_2E_\chi &= \sqrt{m_e^2 + \frac{1}{4s}\lambda(s, m_N^2, m_e^2)}\sqrt{m_\chi^2 + \frac{1}{4s}\lambda(s_{34\bar{\chi}}, s, m_\chi^2)} \\
&= \frac{1}{4s}\sqrt{(s - m_N^2 + m_e^2)^2}\sqrt{(s_{34\bar{\chi}} - s - m_\chi^2)^2} \\
&= \frac{1}{4s}(s - m_N^2 + m_e^2)(s + m_\chi^2 - s_{34\bar{\chi}}),
\end{aligned} \tag{86}$$

keeping in mind that $s > s_{34\bar{\chi}}$. Putting everything together, the physical region of $t_{2\chi}$ is

$$[t_{2\chi}]^\pm = m_e^2 + m_\chi^2 - \frac{1}{2s}(s - m_N^2 + m_e^2)(s + m_\chi^2 - s_{34\bar{\chi}}) \pm \frac{1}{2s}\lambda^{1/2}(s, m_N^2, m_e^2)\lambda^{1/2}(s, s_{34\bar{\chi}}, m_\chi^2). \tag{87}$$

For the remaining two momentum transfer invariants, we use the same procedure to determine their limits, described in greater detail in App. B. Next, $t_{13} = (p_1 - p_3)^2$ will be investigated in the rest frame of $q_{34\bar{\chi}}$, resulting in the physical region

$$\begin{aligned}
[t_{13}]^\pm = m_N^2 + m_X^2 &- \frac{1}{2s_{34\bar{\chi}}}(s_{34\bar{\chi}} + m_N^2 - t_{2\chi})(s_{34\bar{\chi}} + m_X^2 - s_{4\bar{\chi}}) \\
&\pm \frac{1}{2s_{34\bar{\chi}}}\lambda^{1/2}(s_{34\bar{\chi}}, t_{2\chi}, m_N^2)\lambda^{1/2}(s_{34\bar{\chi}}, s_{4\bar{\chi}}, m_X^2).
\end{aligned} \tag{88}$$

The physical region of the last invariant $t_{14} = (p_1 - p_4)^2$ is derived in the rest frame of $q_{4\bar{\chi}}$. This yields, with $q_{23\chi}$ defined in (54), the following integration limits

$$
\begin{aligned}
[t_{14}]^{\pm} = m_N^2 + m_e^2 &- \frac{1}{2s_{4\bar{\chi}}}(s_{4\bar{\chi}} + m_N^2 - q_{23\chi}^2)(s_{4\bar{\chi}} + m_e^2 - m_\chi^2) \\
&\pm \frac{1}{2s_{4\bar{\chi}}}\lambda^{1/2}(s_{4\bar{\chi}}, q_{23\chi}^2, m_N^2)\lambda^{1/2}(s_{4\bar{\chi}}, m_\chi^2, m_e^2).
\end{aligned}
\tag{89}
$$

In order to calculate the relevant cross sections for this work, we need to express all matrix elements in terms of input parameters $\{m_N, m_X, m_e, m_\chi, p_1 \cdot p_2\}$ and Lorentz invariants $\{s_{34\bar{\chi}}, s_{4\bar{\chi}}, t_{2\chi}, t_{13}, t_{14}, \varphi_3, \varphi_4\}$ by recasting all possible scalar products of the six four-momenta of the system. There are 15 independent scalar products of six vectors. $p_1 \cdot p_2$ is already determined by being an input parameter. Furthermore, seven of the scalar products are directly given through the definition of the Lorentz invariants. The energy-momentum conservation additionally relates six of the scalar products to the others, as can be seen in App. C in more detail. We notice, that there still remains one seemingly independent scalar product, which can be re-express as follows. In 4D, a set of more than four vectors cannot be linearly independent. Hence, it is possible to choose one of the scalar products and determine it through $\det \mathbf{M} = 0$, the Gram determinant. We will select $p_\chi \cdot p_{\bar{\chi}}$ for this purpose, the same as in [51]. This is motivated by our previously chosen subsystems and the resulting convenience of the further treatment. $\mathbf{M}$ is the Gram matrix, which in this case, is a 5×5 matrix of scalar products with $(\mathbf{M})_{ij} = p_i \cdot p_j,\ \ i, j \in 1, 3, 4, \chi, \bar{\chi}$. The usage of six vectors here would be redundant, as five are enough for linear dependence. The choice of the five momenta is in principle arbitrary, but here is chosen such that $p_\chi \cdot p_{\bar{\chi}}$ appears in the determinant. Unfortunately, the solution to $\det \mathbf{M} = 0$ gives two results for $p_\chi \cdot p_{\bar{\chi}}$. In order to resolve this degeneracy, we fix the rotation direction of φ_4, see Fig. 20, and use both solutions, one for $[0, \pi)$ and one for $(\pi, 2\pi]$.

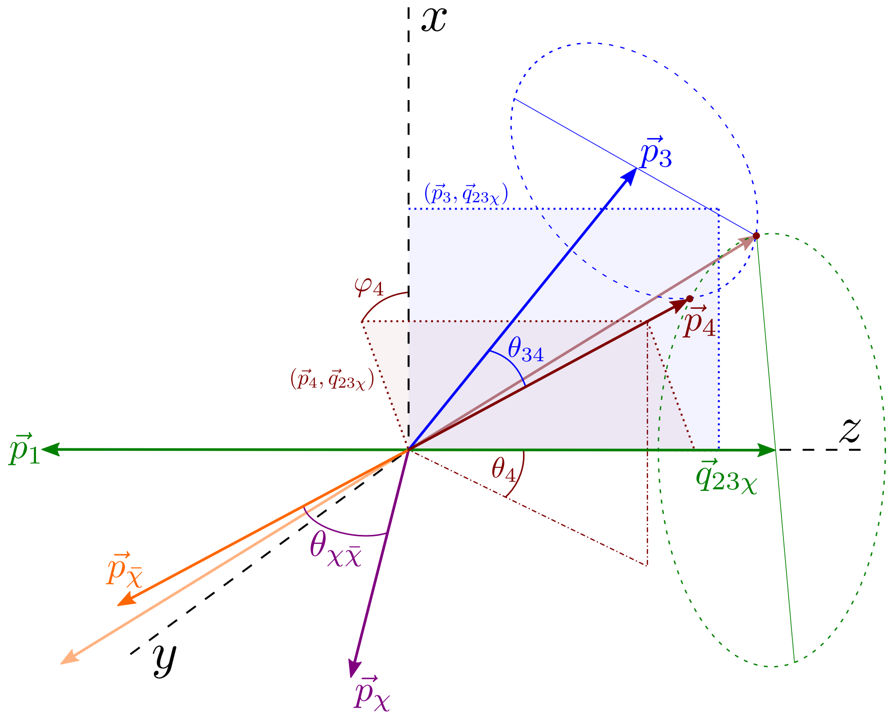

Figure 20: The system of the three-momentum vectors of the phase space in the frame with $\vec{q}_{4\bar{\chi}} = 0$. One can clearly see the degeneracy of the angle $\theta_{\chi\bar{\chi}}$, and consequently of $\vec{p}_\chi \cdot \vec{p}_{\bar{\chi}}$, illustrated by the lightly coloured vectors next to $\vec{p}_4$ and $\vec{p}_{\bar{\chi}}$. This is due to $\vec{p}_4$ not being uniquely defined by $\vec{q}_{23\chi}$ and $\vec{p}_3$.

We now examine this angle degeneracy more closely, using the diagram 20, in the frame where $\vec{q}_{4\bar{\chi}} = 0$. This is equivalent to $\vec{p}_1 + \vec{q}_{23\chi} = 0$, and makes it possible to take $\vec{p}_3$ to lie in the xz-plane and $\vec{q}_{23\chi}$ to be parallel to the z-axis. In this system, the azimuthal angle of $\vec{q}_{4\bar{\chi}}$, and accordingly of $\vec{p}_4$ and $\vec{p}_{\bar{\chi}}$ individually, has no unique value. Hence, it is necessary to fix the angle of $\vec{p}_4$ around the z-axis, and therefore, the angle around $\vec{q}_{23\chi}$, in order to define $\vec{p}_\chi \cdot \vec{p}_{\bar{\chi}}$. Because $\vec{q}_{23\chi}$ is parallel to the z-axis, it too has no unique azimuthal angle and its constituents can be rotated using this freedom. However, since we already put $\vec{p}_3$ in the xz-plane, this manifests in a rotation of $\vec{p}_4$ around $\vec{p}_3$. In conclusion, the orientation of $\vec{p}_4$, and in turn $\vec{p}_{\bar{\chi}}$, is determined by the intersection points of the angular freedom of $\vec{p}_4$ and the z-axis. Unfortunately, this still does not completely alleviate the degeneracy of $\vec{p}_\chi \cdot \vec{p}_{\bar{\chi}}$, shown in Fig. 20, due to two intersections existing. Thus, we resolve this issue, as described in the previous paragraph, by incorporating both solutions, as can be seen in Fig. 20 indicated by the additional light coloured vectors of $\vec{p}_4$ and $\vec{p}_{\bar{\chi}}$.

The previously derived limits are frame-independent, as they solely consist of Lorentz invariant quantities. In this work, however, we are explicitly interested in the lab frame of the target-beam system. Therefore, the differential variables $s_{34\bar{\chi}}$ and $t_{2\chi}$ in (77) need to be replaced by the energy of the outgoing χ particle E_χ and the cosine of the χ particle's angle to the beam line, $\cos\theta_\chi$. In the lab frame $\vec{p}_1 = 0$, the incoming energy is $s = m_N^2 + m_e^2 + 2m_N E_2$ and the χ energy is

$$\begin{aligned} E_\chi &= E_1 + E_2 - E_{34\bar{\chi}} = m_N + E_2 - \sqrt{s_{34\bar{\chi}} + P_{2\chi}^2} = m_N + E_2 - \frac{1}{2m_N}\sqrt{(s_{34\bar{\chi}} - m_N^2 - t_{2\chi})^2} \\ &= m_N + E_2 - \frac{1}{2m_N}(s_{34\bar{\chi}} - m_N^2 - t_{2\chi}), \end{aligned} \tag{90}$$

where $P_{2\chi}^2 = \frac{1}{4m_N^2}\lambda(s_{34\bar{\chi}}, t_{2\chi}, m_N^2)$ is the positive root of the delta function of (73) and care was taken of the sign arsing from the root to assure positivity of $E_{34\bar{\chi}}$. This results makes it possible to derive the limits of E_χ by realising that the value of E_χ is maximal, if $s_{34\bar{\chi}}$ is minimal and $t_{2\chi}$ is maximal, with the reverse being the case for E_χ being minimal. This leads to

$$[E_\chi]^\pm = \frac{1}{2}m_N + E_2 - \frac{1}{2m_N}\Big([s_{34\bar{\chi}}]^\mp - [t_{2\chi}]^\pm\Big). \tag{91}$$

After inserting the respective bounds from (80) as well as (87), and rearranging the terms, this yields the integration region of E_χ:

$$\begin{aligned} E_\chi &\geq \frac{m_\chi(m_N^2 + m_e^2 + m_N E_2)}{m_N\sqrt{m_N^2 + m_e^2 + 2m_N E_2}} \\ E_\chi &\leq \frac{1}{2}(m_N + E_2) - \frac{m_e^2}{2m_N} + \frac{(m_N^2 + m_e^2 + m_N E_2)[m_\chi^2 - (m_X + m_e + m_\chi)^2]}{m_N(m_N^2 + m_e^2 + 2m_N E_2)} \\ &\quad + \frac{\sqrt{E_2^2 - m_e^2}}{2(m_N^2 + m_e^2 + 2m_N E_2)}\sqrt{m_N(m_N + 2E_2) - m_X(m_X + 2m_e)} \\ &\quad \times \sqrt{m_N(m_N + 2E_2) - (m_X + 2m_\chi)(m_X + 2(m_\chi + m_e))}. \end{aligned} \tag{92}$$

Expectedly, for an observable like the energy of χ, the bounds of the physical region are solely determined by the physical parameters, i.e. the total energy we put into the system and the masses of the participating particles. Unfortunately, due to the complexity of a four-body phase space of distinguishable particles with two different input particle, the expressions obtained tend to be quite lengthy. While this is a general feature of relativistic kinematics, we will see that for our specific case, (92) will simplify somewhat.

For $\cos\theta_\chi$, we need to carefully examine the boost from the centre of mass frame $\vec{p}_1 + \vec{p}_2 = 0$, in which the limits of $t_{2\chi}$ are defined with the CM angle $\cos\theta_{2\chi} = \pm 1$ (87), into the LAB frame where $\vec{p}_1 = 0$. In general, such Lorentz boosts are highly non-trivial and we will use the invariants of our systems to simplify the calculation as much as possible. In the LAB frame it is convenient to put the incoming momentum $\vec{p}_2$, i.e. the beam line, into the z-axis, thus having $t_{2\chi} = m_e^2 + m_\chi^2 - 2E_2E_\chi + 2|\vec{p}_2||\vec{p}_\chi|\cos\theta_\chi$. This allows for the reduction of the boost from the CM frame to the LAB frame into a transformation along the z-axis by aligning the centre of mass three-momenta $\vec{p}_{1,\mathrm{CM}} = -\vec{p}_{2,\mathrm{CM}}$ parallel to this axis. This is permitted, since the CM frame only requires the two vectors to be equally long and oppositely oriented, otherwise having complete overall angular freedom. Hence, the maximum value for the χ's angle is evidentially 0, or $\cos\theta_\chi = 1$, in the LAB frame as well. The reason for this is that the boost from CM to LAB frame is along the beam line, so a vector parallel to it will experience no relativistic beaming, also called boosting or relativistic aberration. In principle, the lowest value of $\cos\theta_\chi$ could be -1. This, however, will be increased by the χ having kinetic energy. The minimum value of $\cos\theta_\chi$ is then determined by the minimum value of $s_{34\bar{\chi}}$ for a fixed E_χ, as this makes $t_{2\chi}$ also minimal and thus $\cos\theta_\chi$, which can be seen by recalling that $s_{34\bar{\chi}} = m_e^2 + t_{2\chi} + 2m_e^2E_2 - 2m_e^2E_\chi$. To find the exact lower limit, we use the definition of the invariant $s_{34\bar{\chi}}$ to derive a form for the cosine of the angle as

$$\begin{aligned} s_{34\bar{\chi}} &= (p_3 + p_4 + p_{\bar{\chi}})^2 = (p_1 + p_2 - p_\chi)^2 \\ &= m_N^2 + m_e^2 + m_\chi^2 + 2m_NE_2 - 2m_NE_\chi - 2E_2E_\chi + 2\sqrt{E_\chi^2 - m_\chi^2}\sqrt{E_2^2 - m_e^2}\cos\theta_\chi, \\ \Rightarrow \ \cos\theta_\chi &= \frac{s_{34\bar{\chi}} - m_N^2 - m_e^2 - m_\chi^2 + 2E_2E_\chi + 2m_NE_\chi - 2m_NE_2}{2\sqrt{E_\chi^2 - m_\chi^2}\sqrt{E_2^2 - m_e^2}}. \end{aligned} \tag{93}$$

After inserting the minimum value of $s_{34\bar{\chi}}$, $(m_X + m_e + m_\chi)^2$, into (93) and keeping in mind the fact that the absolute minimum value of $\cos\theta_\chi$ is -1, the integration limits are

$$\begin{aligned} 1 \leq \cos\theta_\chi \leq \max\Bigg\{ -1, &\frac{E_2(E_\chi - m_N)}{\sqrt{E_\chi^2 - m_\chi^2}\sqrt{E_2^2 - m_e^2}} \\ &+ \frac{m_N(2E_\chi - m_N) + m_X(2m_\chi + m_X) + 2m_e(m_X + m_\chi)}{2\sqrt{E_\chi^2 - m_\chi^2}\sqrt{E_2^2 - m_e^2}}\Bigg\}. \end{aligned} \tag{94}$$

5.2 Dark Matter Production Cross Section

After dealing with the four-body phase space integration, the differential production cross section (51) can be calculated by inserting (77) into (51). This is done in the LAB frame with $\vec{p}_1 = 0$, which results in

$$\frac{d^2\sigma_{\mathrm{prod}}}{dE_\chi d\cos\theta_\chi} = \frac{|\vec{p}_\chi|}{4m_N|\vec{p}_2|}\int \frac{d\Pi_{2\to 4}}{ds_{34\bar{\chi}}dt_{2\chi}}\frac{1}{|J|}|\mathcal{M}_{2\to 4}|^2, \tag{95}$$

where $|\mathcal{M}_{2\to 4}|^2$ is the fully spin-summed squared matrix element of the 2-to-4 particle production process, $1/(4m_N|\vec{p}_2|)$ is the flux factor in the LAB frame, and $|\vec{p}_\chi|/|J|$ comes from the transformation of the invariants $(s_{34\bar{\chi}}, t_{2\chi})$ to the LAB frame variables $(E_\chi, \cos\theta_\chi)$; the Jacobian $|J|$ will cancel with the one inside the phase space integral (77). Importantly, while we performed the calculations of the previous section more generally, for our case we will focus on the contributions from electron-electron scattering specifically. This is due the sub-leading contributions of electron-nucleus scattering for heavy atoms in a comparatively low energy regime of about a hundred MeV, which is the focus of this work. Specifically, while the bremsstrahlung-like pair production process is enhanced by the nucleus' charge and the lower momentum transfer to it, at beam energies much lower than m_N, electron-nucleus scattering is kinematically mass suppressed as $(m_e/m_N)^2$. Accordingly, from now $m_N \to m_e$ and $m_X \to m_e$ is taken, simplifying the kinematic expressions. The physical region of the invariants of the system $e^- + e^- \to e^- + e^- + \chi + \bar{\chi}$ thus becomes

$$
\begin{aligned}
1 \leq \cos\theta_\chi &\leq \max\left\{ -1, \frac{E_2(E_\chi - m_e) + m_e(E_\chi + 2m_\chi + m_e)}{\sqrt{E_\chi^2 - m_\chi^2}\sqrt{E_2^2 - m_e^2}} \right\}, \\
E_\chi &\geq \frac{m_\chi(2m_e + E_2)}{\sqrt{2m_e(m_e + E_2)}}, \\
E_\chi &\leq \frac{E_2}{2} + \frac{2m_e + E_2}{2m_e(m_e + E_2)}\left[m_\chi^2 - (2m_e + m_\chi)^2\right] \\
&+ \frac{\sqrt{E_2^2 - m_e^2}}{4m_e(m_e + E_2)}\sqrt{2m_e E_2 - 3m_e^2}\sqrt{2m_e E_2 - 2(m_e^2 + 2m_\chi^2 + 4m_e m_\chi)}, \\
(m_e + m_\chi)^2 \leq s_{4\bar{\chi}} &\leq (\sqrt{s_{34\bar{\chi}}} - m_e)^2, \\
[t_{13}]^\pm &= 2m_e^2 - \frac{1}{2s_{34\bar{\chi}}}(s_{34\bar{\chi}} + m_e^2 - t_{2\chi})(s_{34\bar{\chi}} + m_e^2 - s_{4\bar{\chi}}) \\
&\pm \frac{1}{2s_{34\bar{\chi}}}\lambda^{1/2}(s_{34\bar{\chi}}, t_{2\chi}, m_e^2)\lambda^{1/2}(s_{34\bar{\chi}}, s_{4\bar{\chi}}, m_e^2), \\
[t_{14}]^\pm &= 2m_e^2 - \frac{1}{2s_{4\bar{\chi}}}(s_{4\bar{\chi}} + m_e^2 - q_{23\chi}^2)(s_{4\bar{\chi}} + m_e^2 - m_\chi^2) \\
&\pm \frac{1}{2s_{4\bar{\chi}}}\lambda^{1/2}(s_{4\bar{\chi}}, q_{23\chi}^2, m_e^2)\lambda^{1/2}(s_{4\bar{\chi}}, m_\chi^2, m_e^2),
\end{aligned}
\tag{96}
$$

where we used that in the LAB frame $s = 2m_e(m_e + E_2)$ and $q_{23\chi}^2 = 2m_e^2 + s_{4\bar{\chi}} + t_{2\chi} - s_{34\bar{\chi}} - t_{13}$. The angular integration limits remain the same as in (78).

5.2.1 Feynman Diagrams and Matrix Elements

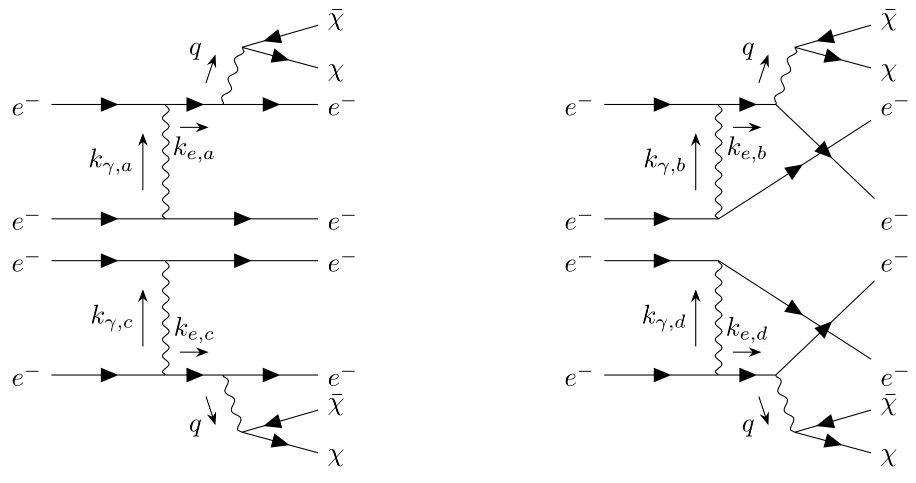

Figure 21: Final state radiation production of χ - $\bar{\chi}$ pairs. The $k_{\gamma,n}$ and $k_{e,n}$, with $n \in \{a, b, c, d\}$, represent the momenta for each diagram indexed by n.

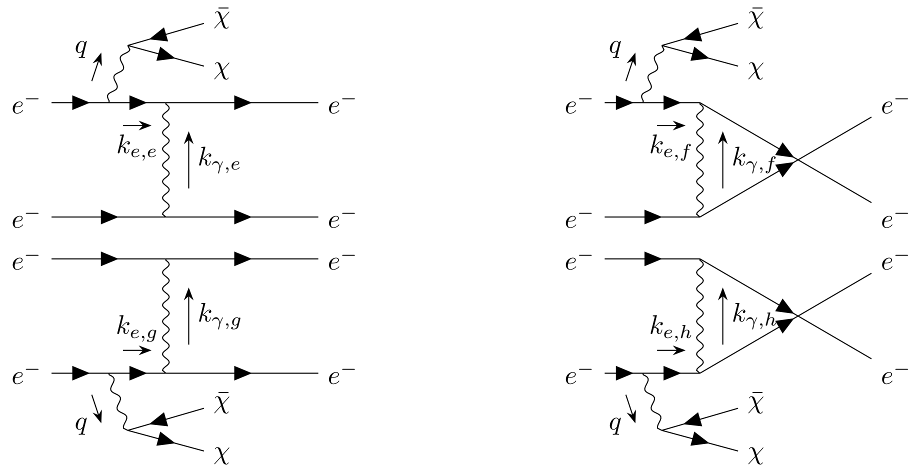

Figure 22: Initial state radiation production of χ - $\bar{\chi}$ pairs. The $k_{\gamma,n}$ and $k_{e,n}$, with $n \in \{e, f, g, h\}$, represent the momenta for each diagram indexed by n.

The relevant Feynman diagrams for the pair production of χ using electron-electron scattering are shown in Fig. 21 for final state radiation, and 22 for initial state radiation. They correspond to bremsstrahlung emission of a virtual photon, which subsequently produces a χ particle-antiparticle pair. The momentum transfer k_γ and the electron propagator momentum k_e in these figures depend on the particular diagram, while $q = p_\chi + p_{\bar{\chi}}$ is the total momentum of the χ particle-antiparticle pair. It is necessary to consider all eight diagrams due to the indistinguishable scattering partners, greatly increasing the number of terms in the resulting squared matrix element. This also prevents us from neglecting masses, as could be done with the electron mass in the case of electron-nucleus scattering. As can be seen from the Feynman diagrams, it is possible to split the production matrix element $i\mathcal{M}_{\text{prod}}$ into an electron scattering part with the emission of a virtual photon $i\mathcal{M}^\alpha_{ee}$, and a χ particle-antiparticle pair production part $i\mathcal{M}_{\chi,\alpha}$, as

$$i\mathcal{M}_{\text{prod}} = (i\mathcal{M}^\alpha_{ee})\frac{-ig_{\alpha\beta}}{q^2 + i\epsilon}(i\mathcal{M}^\beta_\chi) = \frac{-i}{q^2 + i\epsilon}(i\mathcal{M}^\alpha_{ee})(i\mathcal{M}_{\chi,\alpha}). \tag{97}$$

Again we use Feynman gauge, as this does not affect tree level calculation due to the on-shell spinors. The pair production part is then

$$i\mathcal{M}_{\chi,\alpha}(q) = \bar{u}_\chi(i\Gamma_\alpha(q))v_{\bar{\chi}}, \tag{98}$$

where u_i refers to the spinor for a fermion with momentum and mass (p_i, m_i) and its corresponding spin index, v_j refers to the spinor for an antifermion with momentum and mass (p_j, m_j) and its corresponding spin index, while $i\Gamma_\alpha(q)$ refers to the EM form factor vertices in (3a-3e). The electron-electron scattering part is

$$i\mathcal{M}^\alpha_{ee} = \sum_{n=1}^{8} i\mathcal{M}^\alpha_{ee,n} = \sum_{\text{FSR: } m=1}^{4} i\mathcal{M}^\alpha_{ee,m} + \sum_{\text{ISR: } r=1}^{4} i\mathcal{M}^\alpha_{ee,r}, \tag{99}$$

where the first part of the sum are the four final state radiation diagrams in (21) and the second part of the sum are the initial state radiation diagrams in (22). The general final state radiation is of the form

$$i\mathcal{M}^\alpha_{ee,m} = (ie)^3\bar{u}_k\gamma^\mu u_i\frac{-ig_{\mu\nu}}{k^2_{\gamma,m} + i\epsilon}\bar{u}_l\gamma^\alpha\frac{i(\not{k}_{e,m} + m_e)}{k^2_{e,m} - m_e^2 + i\epsilon}\gamma^\nu u_j, \tag{100}$$

with the corresponding electrons $\{i, j, k, l\}$, while $k_{\gamma,m}$ and $k_{e,m}$ refer to the momenta for each diagram as denoted in (21) for $m \in \{a, b, c, d\}$. Similarly, the general initial state radiation is of the form

$$i\mathcal{M}^\alpha_{ee,r} = (ie)^3\bar{u}_k\gamma^\mu u_i\frac{-ig_{\mu\nu}}{k^2_{\gamma,r} + i\epsilon}\bar{u}_l\gamma^\nu\frac{i(\not{k}_{e,r} + m_e)}{k^2_{e,r} - m_e^2 + i\epsilon}\gamma^\alpha u_j, \tag{101}$$

where $k_{\gamma,r}$ and $k_{e,r}$ are the momenta seen in (22) for $r \in \{e, f, g, h\}$. We calculate the spin-summed squared matrix elements from these amplitudes using FeynCalc [59],[60],[61] in Mathematica. With the analytical expressions obtained, much too long to list here, the final tree-level form for the electron-electron χ pair production cross section (95) is obtained. Importantly, there are additional tree-level diagrams that can contribute to χ pair production, but these all are of higher order in the form factor couplings than the ones in Fig. 21 and 22. Hence, graphs like Fig. 23, and similar ones, are not considered here, due to additional suppression of the production cross section by an EM form factor squared.

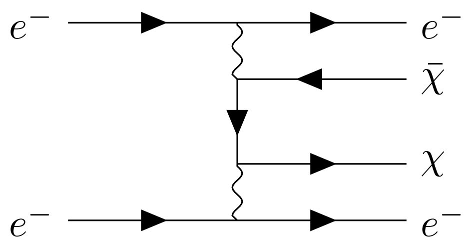

Figure 23: Example of an additional tree level contribution to the production cross section of higher order in the form factor couplings.

6 Detection of Produced Dark Matter

Having calculated both the production cross section σ_{prod} (95) and the elastic electron-χ cross section (41), from now on referred to as detection cross section σ_{det}, it is time to combine them in order to make predictions for a detector set-up. First of all, we want to find the number of χ particles produced in the beam dump upon being hit by an electron beam. If the beam dump is thick with respect to the radiation length X_T of its material, the maximum penetration depth of the beam is X_T. This is due to the attenuation of the incoming electron flux onto the beam dump through electron-electron scattering. The rate of χ-particles N_χ that are created in the beam dump, when it is hit by an electron flux Φ_e from the beam, is

$$\frac{dN_\chi}{dt} = \Phi_e A_T X_T n_T \sigma_{\text{prod}}, \tag{102}$$

where A_T is the area of the beam dump hit by the beam, n_T is the target density of the beam dump, here, its electron density. Since the detection cross sections (43a-43e) explicitly depend on the energy of the incoming particles E_χ, it is necessary to consider the differential production cross section with respect to E_χ. Additionally, the differential production cross section with respect to the angle of the created particles $\cos\theta_\chi$ is needed, as any detector will only have partial angular coverage of the flux from the beam dump. The differential rate of χ production at the beam dump (102), that are of energy E_χ and angle θ_χ, is then

$$\frac{d^2}{dE_\chi d\cos\theta_\chi}\left(\frac{dN_\chi}{dt}\right) = \Phi_e A_T X_T n_T \frac{\sigma_{\text{prod}}}{dE_\chi d\cos\theta_\chi}, \tag{103}$$

The angular dependence of (103) ensures that only the particles that actually hit the detector will contribute. After determining the number of produced χ at the beam dump, the next step is finding the detection event rate R_{event}. This rate is

$$R_{\text{event}} = \frac{dN_\chi}{dt} n_{\text{det}} L_{\text{det}} \sigma_{\text{det}}, \tag{104}$$

where n_{det} is the density of scattering sites in the detector, here electrons, L_{det} is the length of the detector, and σ_{det} are the detection cross sections (43a-43e). Since the χ particles only interact weakly, they are not attenuated, therefore, the total length of the detector needs to used. As discussed in the section above, it is necessary to consider the differential quantity in order to account for the geometry and energy sensitivity of the detector, as not all produced χ particles will actually hit it. Hence, the differential event rate, using (103), is

$$\frac{d^2 R_{\text{event}}}{dE_\chi d\cos\theta_\chi} = n_{\text{det}} L_{\text{det}} \sigma_{\text{det}} \frac{d^2}{dE_\chi d\cos\theta_\chi} \left(\frac{dN_\chi}{dt}\right) = \Phi_e A_T n_T X_T n_{\text{det}} L_{\text{det}} \frac{d^2\sigma_{\text{prod}}}{dE_\chi d\cos\theta_\chi} \sigma_{\text{det}}, \tag{105}$$

The detection cross section σ_{det} depends on the energy of the incoming χ particle, and therefore, needs to be integrated against the production cross section. Additionally, it is necessary to integrate over the angular coverage of the detector to get the desired event rate. It is often useful to consider not the total even rate, but instead the differential one, especially with respect to the energy transfer. In our case, this transfer is represented by the electron's recoil energy E_R (35). Thus, the final form of the *differential detection event rate per recoil energy* is

$$\frac{dR_{\text{event}}}{dE_R} = \Phi_e A_T n_T X_T n_{\text{det}} L_{\text{det}} \int dE_\chi d\cos\theta_\chi \frac{d^2\sigma_{\text{prod}}}{dE_\chi d\cos\theta_\chi} \frac{d\sigma_{\text{det}}}{dE_R}. \tag{106}$$

The integration limits for E_χ are in (96). For $\cos\theta_\chi$ however, it is necessary take into account that the lower limit can either be (96) or, if smaller, the maximum angular coverage of the detector. If, instead, we wanted to consider the detection event count N_{event}, the beam time needs to taken into account. Therefore, the *differential event count* is

$$\frac{dN_{\text{event}}}{dE_R} = N_{\text{EOT}} n_T X_T n_{\text{det}} L_{\text{det}} \int dE_\chi d\cos\theta_\chi \frac{d^2\sigma_{\text{prod}}}{dE_\chi d\cos\theta_\chi} \frac{d\sigma_{\text{det}}}{dE_R}. \tag{107}$$

where N_{EOT} represents the total electrons incident on the beam dump. An electron beam of sufficient intensity for the production to be efficient, will likely not continuously run, instead it will be pulsed. But since the relevant parameter N_{EOT} only counts the total number of incident electrons, the calculation still holds.

Now that we have calculated the algebraic expressions of the observables, we want to make concrete predictions. The values for the constants in (106) and (107) will depend on the particular materials used for the beam dump/detector and the electron beam that will be employed. The difficult part in explicitly computing these observables is the five dimensional integration, needed to determine the differential production cross section, and the additional two dimensional integration for (106) and (107). The upper integration bound for the recoil energy E_R is given by (44), while the lower one is determined by the sensitivity of the detector. Such higher dimensional integrals are usually difficult to compute in their own right, but for the long rational functions, that make up the matrix elements in the integrand, they are practically impossible to analytically solve. Therefore, we will have to treat them using numerical methods, if we are to actually calculate any observable. This will be handled in the next section.

7 Numerical Methods for Cross Sections

In order to evaluate the long and complex expressions encountered in the phase space integral and the production matrix elements in (95), we use *Monte Carlo integration.* Deterministic numeric integration methods, like the trapezoidal rule or the Newton-Cotes formula, sample the integration region at fixed points. While this is well suited to low dimensional integrals, the computational complexity of these methods grows exponentially with increasing dimension. To illustrate, for the simple case, in which an n-integration is treated as a series of one-dimensional ones, each dimension has to be sampled at the same number of fixed points k. Hence, such a method needs to sample the integrand at k^n points, making it unviable for high dimensions. Contrary to this, non-deterministic methods sample points in the integration region randomly. The advantage of this approach is that it is independent of the dimension of the integral. Probably the most common non-deterministic method is Monte Carlo integration. In the case of uniformly distributed sample points, this technique estimates the integral by the arithmetic mean of the function evaluated at those points. For an integral I, whose integration region has a volume of V, this takes the form

$$I = \int_V f(x) d^n x = V \int f(x) \frac{1}{V} d^n x = V \int f(x) p(x) d^n x = V \langle f(x) \rangle \approx V \frac{1}{N} \sum_{i=1}^{N} f(x_i). \tag{108}$$

In (108), $1/V$ is treated as continuous uniform distribution $p(x)$, hence making the integral evaluate to the expectation value of $f(x)$. This is subsequently approximated by the expectation value of a discrete uniform distribution, i.e. the arithmetic mean. As can be seen from (108), this method does not depend on the dimension and increases in accuracy as N becomes big due to the law of large numbers. It turns out that the rate of convergence is proportional to $1/\sqrt{N}$ or even $1/N$, depending on the sampling [62]. In order to reduce the number of required points and improve the variance of the result, modern implementations of Monte Carlo integration use schemes like importance sampling to preferentially sample points where the integrand is large or peaked.

Since the integrals in the event rate have dimension five in the space of Lorentz invariants, such a Monte Carlo integration is employed to evaluate them. The implementation used here is the package *CUBA* [63], version CUBA-4.2.2, in Fortran. We utilise the *VEGAS algorithm* from CUBA. First of all, the calculation will take place over the five dimensional unit hypercube, and therefore, it is necessary to normalise the integration region U. This is done by the standard procedure, i.e. take a variables u with integration limits u_-, u_+ and transform it into $\hat{u} = (u - u^-)/(u^+ + u^-)$ with $(u^+ + u^-)d\hat{u} = du$. The Jacobian of this transformation is just the product of $(u^+ + u^-)$ for all variables. This yields the desired integral on the n-dimensional unit hypercube as

$$\int_U f(u) d^n u = \int_{[0,1]^n} f(\hat{u}) \prod_{i=1}^{n} (u_i^+ + u_i^-) d^n \hat{u} \tag{109}$$

Operationally, the evaluation of the integrand and Jacobian is implemented by using functions that calculate the un-normalised Lorentz variables u from the normalised integration variables $\hat{u}$, using the input parameters, namely the electron mass m_e, χ mass m_χ and the input energy E_2. Subsequently, all scalar products are calculated from these using the relations in App. (C.1) and (C.2). Employing these functions, the integrand (95) is computed using a wrapper that interfaces with the CUBA algorithms. The matrix elements for the production part are too long to be compiled in Fortran as given by FeynCalc. Therefore, common expression are factored out and the single long expressions are subdivided into multiple in accordance with the limitations of Fortran. Overall, each of the files containing the production matrix element code for the different interactions are few thousand lines long. This streamlining of the code also increases the computational speed significantly by reducing superfluous evaluations of repeated sub-expressions.

Because the numerical integration using Monte Carlo is computationally expensive, we want to minimise the amount of calculations we need to perform. Hence, to get (95) as a function of $\cos\theta_\chi$ and E_χ, we sample the function at a few values for these variables and then interpolate. Additionally, (95) also needs to be a function of the mass m_χ in order to look at different models, hence m_χ is also sampled at a few values. Exponential sampling is used for $\cos\theta_\chi$ as well as m_χ, and Cauchy sampling for E_χ in order to prevent Runge's phenomenon when interpolating and to focus on areas where the integrated functions peak. Then, the differential event rate (107) is computed by first interpolating the numeric result from the Monte Carlo integration of (95) with respect $\cos\theta_\chi$, and then integrating over the angle. Finally, the intermediate result is interpolated with respect to E_χ and again integrated to obtain the final result for (107). We are primarily interested in detector events, hence (107) must also be integrated with respect to E_R. Since the detection cross sections (43a-43e) are analytic and have a simple dependence on E_R, it suffices to integrate E_R using numerical quadrature.

Additionally, it is also instructive to calculate the total production cross section σ_{prod} to see the mass dependence of the different interactions. This is done by integrating (95) with respect to E_χ and $\cos\theta_\chi$. This is implemented by directly computing the seven dimensional integral of the matrix elements using Monte Carlo integration for different values of m_χ. Due to numerical instability for low masses, a few integration runs are performed and subsequently fitted. Before moving on to the results, we will briefly discuss an exemplary detector that could be used to test the prediction of this work.

8 DAMIC-M CCD-Detector

In order to detect the sub-GeV dark matter particles described in this work, a detector with a low energy threshold is required. A relatively recent type uses charge-coupled devices (CCDs) with a sophisticated read-out method called *Skipper-CCD*. This method was proposed in the 1990's but has only become technologically feasible in last decade [42]. A few experiments have already been implemented using this technology and more are in development, like SENSEI or DAMIC. We will start off this section by quickly describing how a CCD functions and briefly outlining what Skipper-CCD is. Then DAMIC will be discussed, and its successor DAMIC-M will be investigated as a possible detector for the experimental set-up described in earlier sections. The properties of DAMIC-M will be used as a reference for calculating the final numerical results for the event rate.

A *charge-coupled device*, or CCD, is a doped semiconductor device that can accumulate individual charges, holes or electrons, and subsequently read out those charge packets [64, 65]. Roughly, it consists of an interior bulk made of doped silicon sandwiched between two electrodes, one of which is insulated towards the bulk, as can be seen in Fig. 24. Depending on what the CCD is supposed to detect, the insulated electrode needs to be transparent to the desired signal. Read-out gates are attached to the insulated electrode. Now, when applying a voltage to this device, a depletion layer forms in the doped silicon. When some process creates an electron/hole pair in the bulk, it is separated by the voltages, with one type of charge carrier drained away and the other type collect in the potential well of a gate. These accumulated charge packet can then be read out. Usually, CCDs consist of multiple units that function like described above, and are called pixels. While CCDs are commonly used in conjunction with the photoelectric effect to record light intensity, most often in photographic cameras or astronomical applications, in principle, they are sensitive to all processes that create hole/electron pairs in its bulk. This includes, for instance, alpha and beta radiation as well as any other interaction that is able to ionise its constituent atoms.

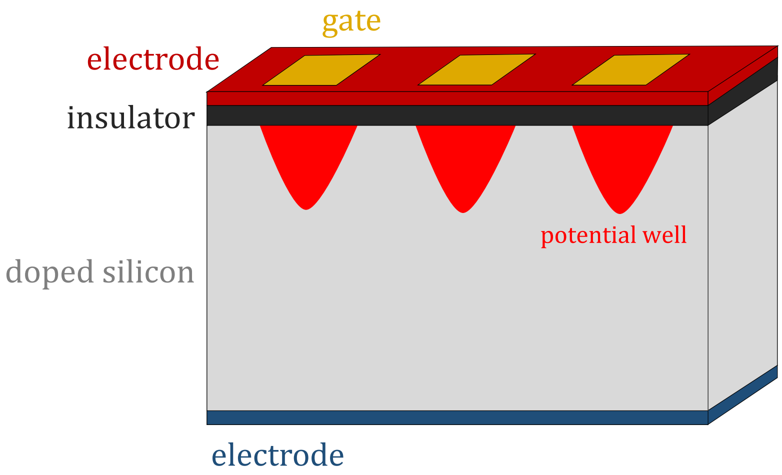

Figure 24: Schematic diagram of a CCD. Doped silicon is sandwiched between two electrodes, where one of them is insulated. On top of the insulated electrode, gates are located that deplete the silicon below them and form potential wells. Liberated charge carriers are then pulled to those wells and trapped there until read out.

The usual read-out method of CCDs is ill-suited for application in dark matter searches, as it destroys the charge packets. A single measurement of the packets is insufficient to achieve the low energy threshold, which in the case of CCDs is equivalent to individual electron precision, necessary for a DM detector due to high noise [42]. This is even true for radiation shielded and cryogenically cooled CCDs. Therefore, a different method for reading out the charge liberated by dark matter interactions is needed. Skipper-CCD [42] is exactly one such method. Here, the packets are read out multiple times, significantly reducing the effect of noise on the measurement. Skipper-CCD is even able to achieve single-electron precision. An example of an experiment that uses this method is SENSEI [43]. SENSEI stands for *Sub-Electron-Noise Skipper-CCD Experimental Instrument* and is located at SNOLAB in Sudbury Canada. Results from SENSEI has already been released and potentially help to indicates a low energy excess [66].

Another experiment that uses the same technology is DAMIC at SNOLAB [44]. DAMIC stands for *DArk Matter In CCDs*. It employs silicon CCDs of high radiation purity together with lead and copper shielding to achieve, ideally, single electron precision in measurements. The CCDs are cooled to cryogenic temperatures to ensure a low thermal dark current, leading to reduced noise. DAMIC is currently active and already underwent observational runs [67, 68, 69]. These results successfully demonstrated the technology and served as a prototype for a larger experiment. The successor of DAMIC is called DAMIC-M [70, 46], the M standing for the Laboratoire Souterrain de Modane, where it is located. DAMIC-M consists of 52 CCD modules that are inside a cryocooler, keeping the modules at about 130 K [71, 72]. The housing of the modules is shielded by lead, some of which is archaeological, and polyethylene. The individual CCDs are 670 μm thick and have an area of $(9 \times 2.25)\,\mathrm{cm}^2$ each. DAMIC-M also uses Skipper-CCD in order to reduce the noise by a factor of $1/\sqrt{N_{\text{skip}}}$, where N_{skip} is the number of read-outs of a single charge packet [71]. It will be capable of reaching single electron precision and an energy threshold of a few eV. The initial test runs have been completed and it is expected to be fully operational in 2025 [72]. DAMIC-M shall serve as an example detector that could be used for the experimental set-up briefly outlined earlier. Its CCDs facilitate the χ-electron scattering investigated here and the specifications of DAMIC-M are used in the numerical predictions of the next section.

9 Results for Predicted Events

Now we will give the numerical results of the computations, the main goal of this work. Although it is not used directly for further calculations, it is instructive to look at the total production cross section σ_{prod} (95) for all five interactions (3a-3e). Using the prescription given in the section on numerical methods, Fig. 25 shows the total production cross section for millicharge as a function of the mass of χ, Fig. 26 shows the magnetic and electric dipole moments and Fig. 27 likewise shows the anapole moment as well as the charge radius interaction.

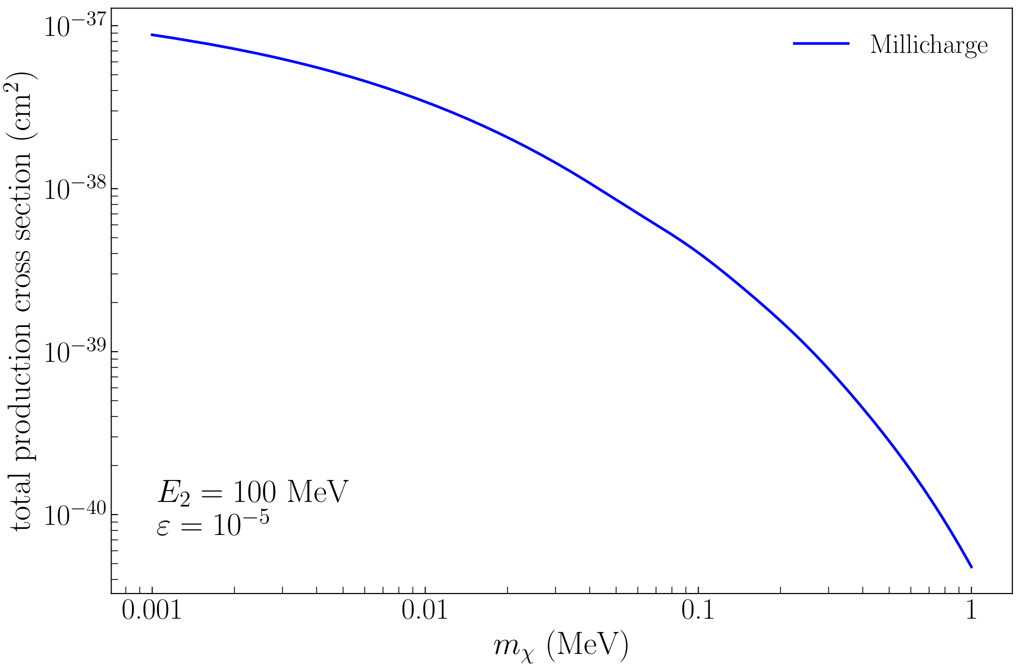

Figure 25: Total cross section for millicharge $\chi\bar{\chi}$ pair production from e^-e^- scattering for different masses m_χ of χ. The energy of the incoming electron is $E_2 = 100\,\text{MeV}$ and χ has a millicharge of $\varepsilon = 10^{-5}$.

Due to the millicharge being identical to a Coulomb interaction with a diminished electric charge, there is a significant mass dependence, as can be seen in Fig. 25. The effective operators show the expected low mass behaviour. MDM and EDM in Fig. 26 exhibit a weak mass dependence and converge for small mass, confirming that these two interactions only differ by mass-dependent terms. Likewise, for AM and CR in Fig. 27 this behaviour is even more pronounced and the mass dependence is even weaker.

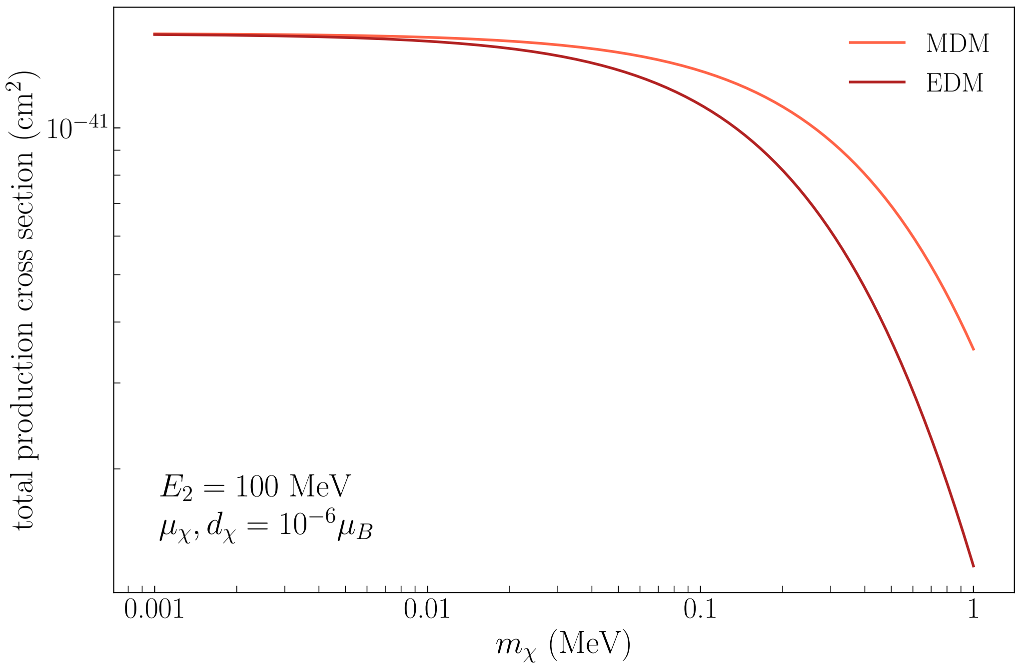

Figure 26: Total cross section for MDM and EDM $\chi\bar{\chi}$ pair production from e^-e^- scattering for different masses m_χ of χ. The energy of the incoming electron is $E_2 = 100\,\mathrm{MeV}$ and χ has a magnetic or electric dipole moment of $\mu_\chi = d_\chi = 10^{-6}\mu_B$.

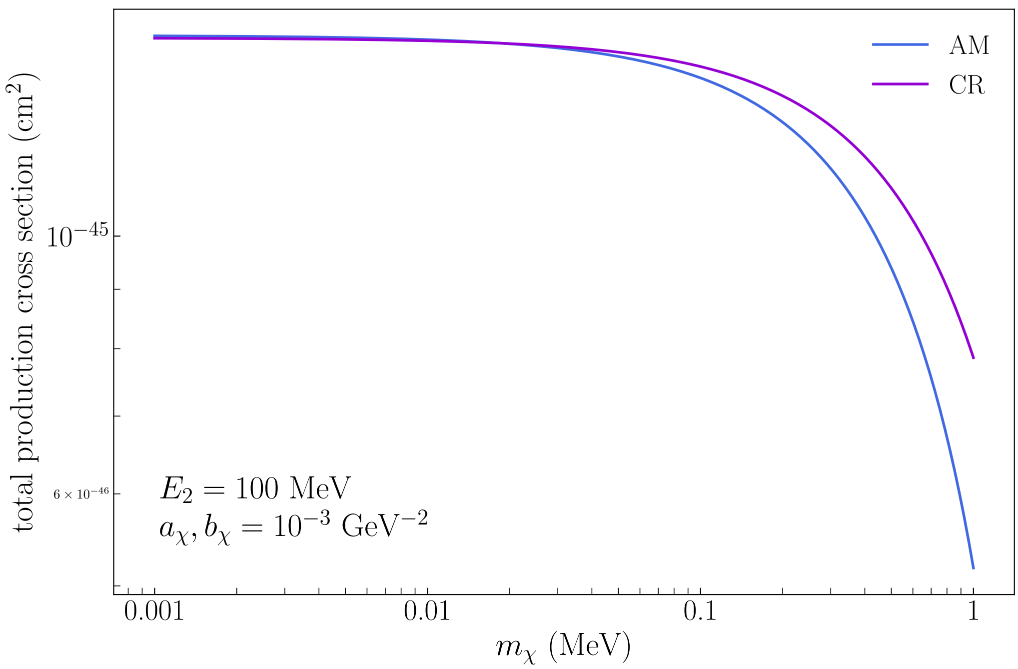

Figure 27: Total cross section for AM and CR $\chi\bar{\chi}$ pair production from e^-e^- scattering for different masses m_χ of χ. The energy of the incoming electron is $E_2 = 100\,\mathrm{MeV}$ and χ has a anapole moment or charge radius of $a_\chi = b_\chi = 10^{-3}\,\mathrm{GeV}^{-2}$.

Next, we will present the results of the calculation of the observable event count per recoil energy E_R (107), as well as the total amount of observed events N_{event}, obtained by integrating (107) with respect to E_R. In order to get predictions for an experimental set-up of production and detection, it is necessary to use some physical parameters. For the beam dump, lead is used as an exemplary material with a radiation length $X_T = 0.56\,\text{cm}$ and target (here electron) density of $n_T = Z_{\text{Pb}}\rho_{\text{Pb}}/m_{\text{Pb}}$, where $Z_{\text{Pb}} = 82$ is the atomic number of lead, $m_{\text{Pb}} = 207.2\,\text{u}$ its atomic mass in daltons and $\rho_{\text{Pb}} = 11.35\,\text{g}\,\text{cm}^{-3}$ its density. Furthermore, an electron beam is needed for the set-up. For this work we have used $N_{\text{EOT}} = 10^{20}$ for the total electrons on target, which can be achieved, for instance, by a 10 kW beam accelerating electrons with 100 MV for a total duration of ca. 45 h.

The detector used is the aforementioned DAMIC-M. Its active part consists of 52 silicon CCDs. The CCDs are stacked horizontally inside the detector, and it is assumed that the beam line is parallel to the long axis of the CCD stack. This density of detection sites, i.e. the electron density in the CCDs, is $n_{\text{det}} = Z_{\text{Si}}\rho_{\text{Si}}/m_{\text{Si}}$, where $Z_{\text{Si}} = 14$ is the atomic number, $m_{\text{Si}} = 28.08\,\text{u}$ the atomic mass and $\rho_{\text{Si}} = 2.33\,\text{g}\,\text{cm}^{-3}$ the density of silicon. The length of the active stack is $L_{\text{det}} = 52 \times 670\,\mu\text{m}$, since the χ flux is not attenuated due to the smallness of the cross sections involved. The values for the atomic quantities are taken from the Particle Data Group [73]. DAMIC-M CCDs have an energy threshold of 10 eV, which sets the lower integration limit of E_R. For the angular aperture of the detector we take $1°$, which roughly translates to a 9 cm detector size placed ca. 5 m away from the beam dump. Fig. 28 shows the result for the calculation of (107), using the aforementioned parameters, for a millicharged particle with $\varepsilon = 10^{-5}$ and a beam energy of 100 MeV for nine different masses of χ. Likewise, Fig. 29 displays the same result with a lower beam energy of 25 MeV.

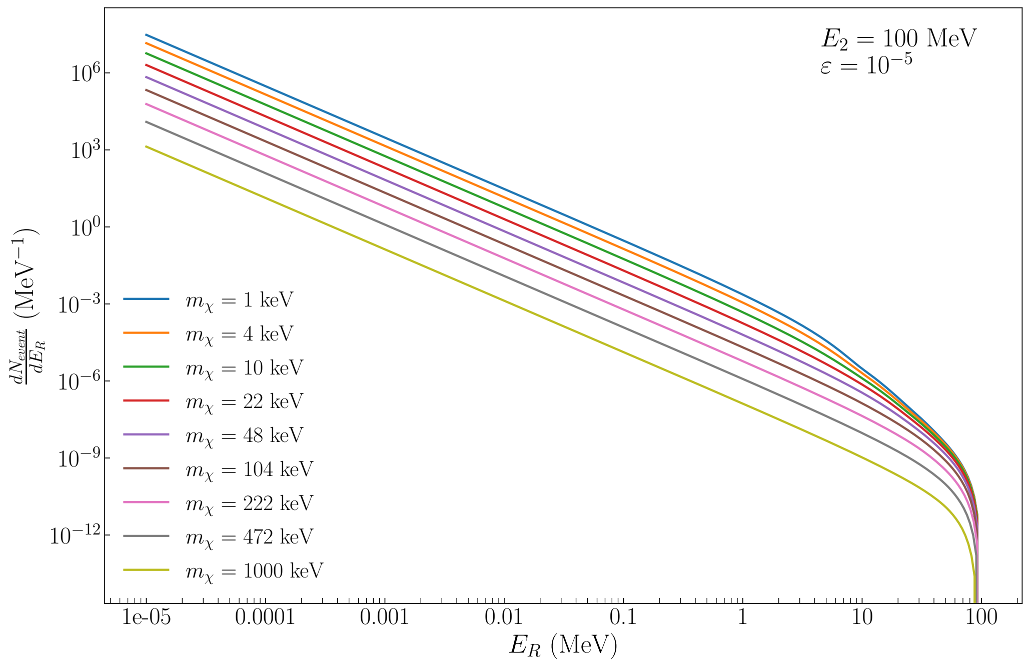

Figure 28: Differential event count per recoil energy E_R for χ with millicharge $\varepsilon = 10^{-5}$ and a beam energy of 100 MeV for nine different masses of χ.

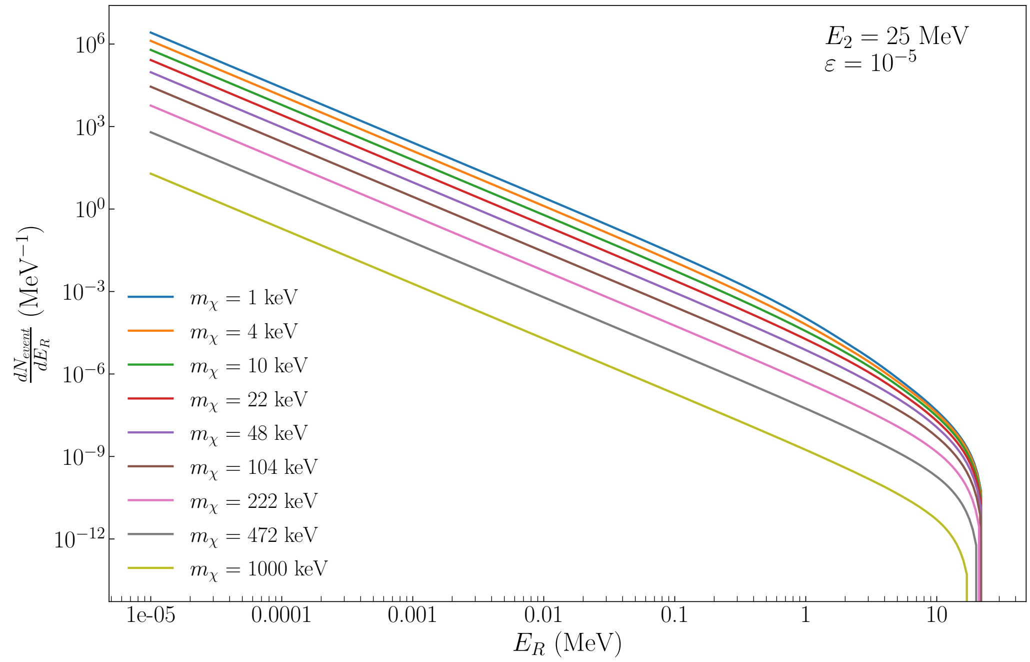

Figure 29: Differential event count per recoil energy E_R for χ with millicharge $\varepsilon = 10^{-5}$ and a beam energy of 25 MeV for nine different masses of χ.

Both Fig. 28 and Fig. 29 show a recoil energy dependence of E_R^{-2}, as expected from (43a). It can be seen from comparing those two graphs, that the beam energy dependence is more pronounced for higher masses, as the 25 MeV case is starting to approach the energy threshold of χ production. The steep drop at high recoil energies represents the kinematic endpoint of χ-electron scattering in the detector, vanishing for (44). To find the total events, it is necessary to integrate the differential event count. Table 3 shows the predicted events at the detector for four different beam energies with the millicharge ε and the electrons on target N_{EOT} factored out.

Table 3: The predicted detection events of produced millicharged χ particles for four different beam energies. All results are given with ε, the millicharge of χ, and N_{EOT}, the number of total electrons incident on the beam dump, factored out.

	$N_{\mathrm{event}} \times (10^{20}\varepsilon^4) \times (10^{-20} N_{\mathrm{EOT}})$			
m_χ(MeV)	100 MeV	75 MeV	50 MeV	25 MeV
0.001	302	186	95	26
0.01	55	36	20	5
0.1	2.2	1.6	1.0	0.3
1	1.3×10^{-2}	6.9×10^{-3}	2.3×10^{-3}	1.9×10^{-4}

The results for MDM and EDM can be seen in Fig. 30. The differential event count is evaluates for a beam energy of 100 MeV for nine different χ masses and a MDM or EDM of $\mu_\chi = d_\chi = 10^{-5}\mu_B$, where μ_B is the Bohr magneton. While their values are comparable, their χ mass dependence deviates. This difference stems from the γ^5 that distinguishes MDM and EDM. Fig. 30 shows that the mass dependence is more pronounced for EDM relative to MDM. Expectedly, the E_R behaviour largely follows (43b) for MDM and (43c) for EDM, only starting to deviate near the kinematic endpoint.

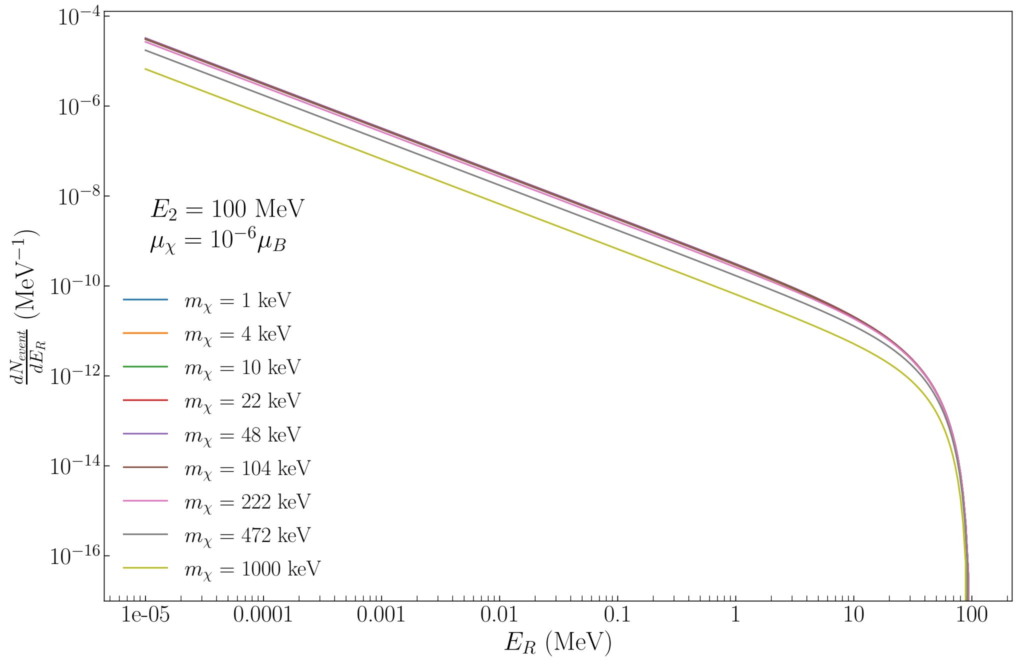

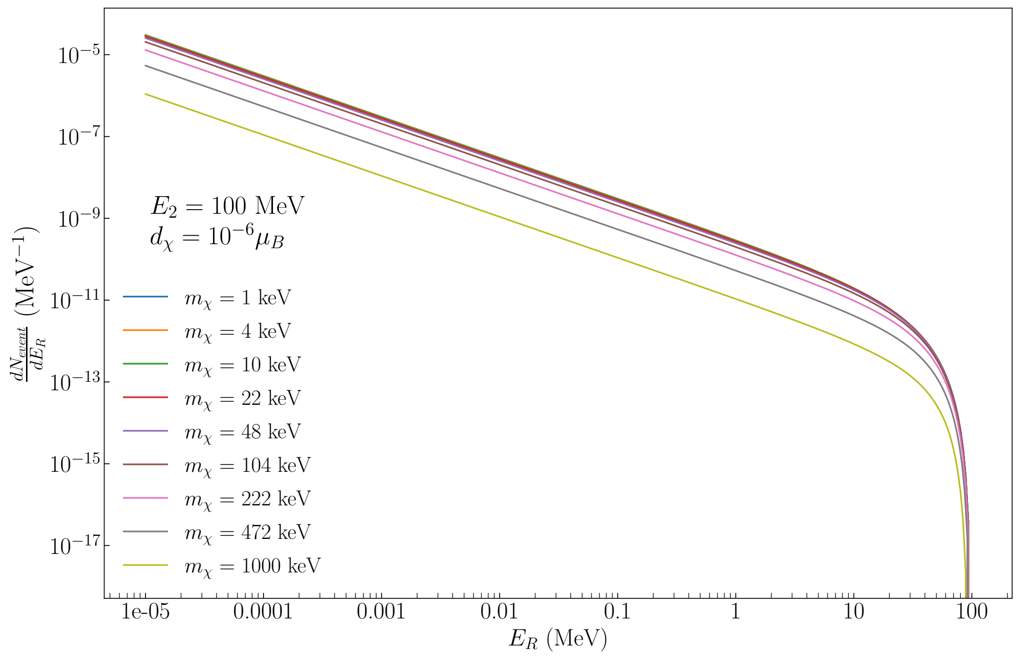

Figure 30: Differential event count per recoil energy E_R of produced χ particles with an MDM or EDM at a beam energy of $E = 100\,\text{MeV}$ for nine different masses of χ. The upper graph shows the results for an MDM $\mu_\chi = 10^{-5}\mu_B$. The lower graph shows the results for an EDM of $d_\chi = 10^{-5}\mu_B$. The different mass scaling of the two interactions is noticeable.

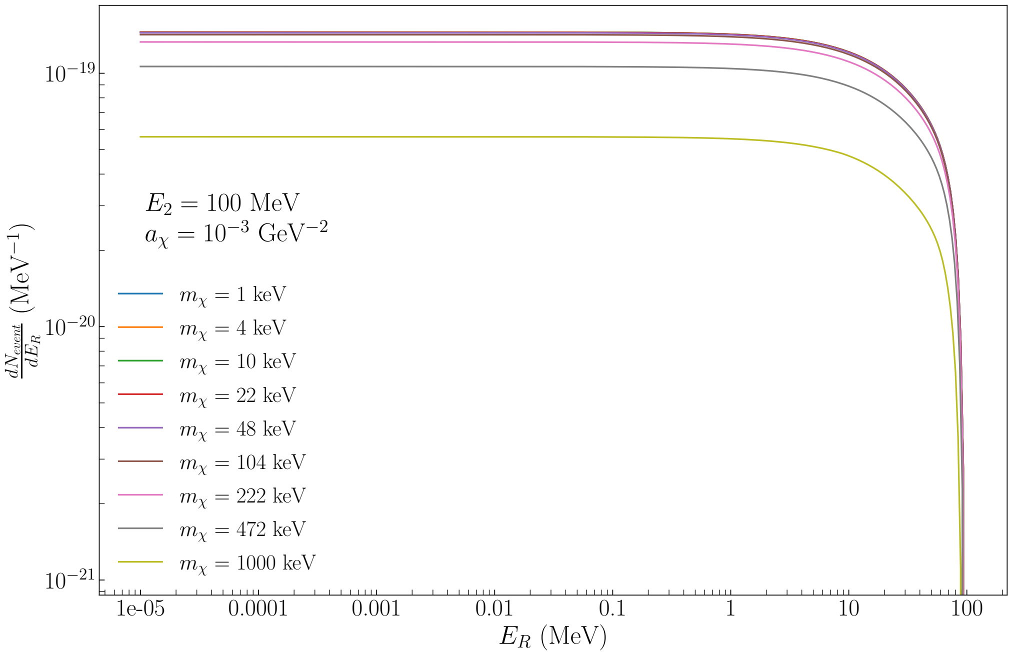

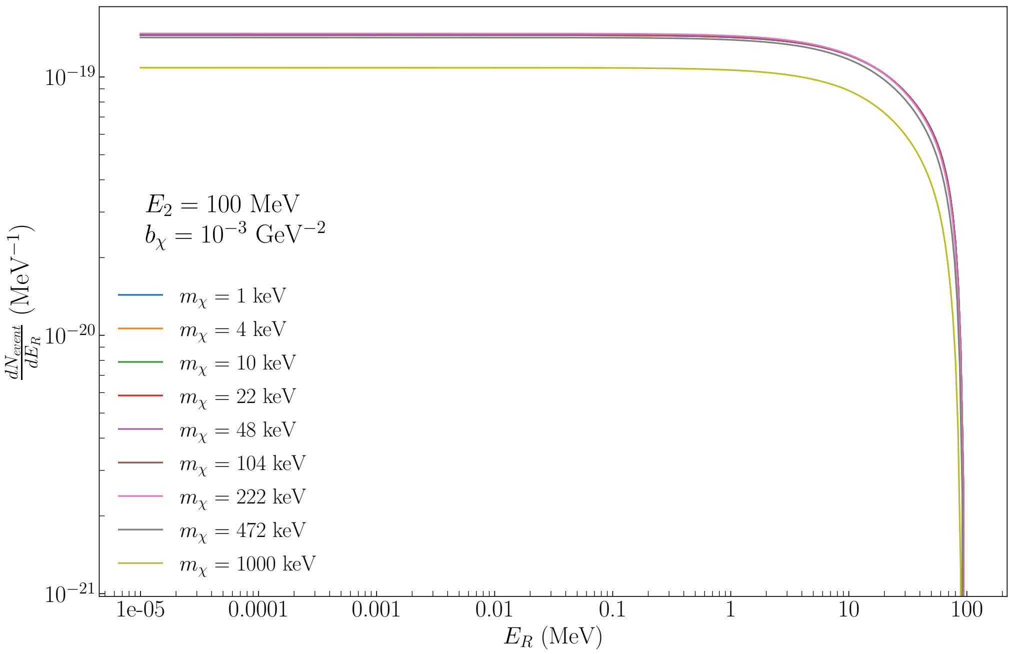

Figure 31: Differential event count per recoil energy E_R of produced χ particles with an AM or CR at a beam energy of $E = 100\,\text{MeV}$ for nine different masses of χ. The upper graph shows the results for an AM of $a_\chi = 10^{-3}\,\text{GeV}^{-2}$. The lower graph shows the results for CR of $b_\chi = 10^{-3}\,\text{GeV}^{-2}$. The difference in mass dependence can be seen.

Fig. 31 shows the results for AM and CR with a beam energy of 100 MeV for nine χ masses. The AM and CR used are $a_\chi = 10^{-3}\,\mathrm{GeV}^{-2}$ and $b_\chi = 10^{-3}\,\mathrm{GeV}^{-2}$, respectively. The E_R behaviour is in accordance with (43d) and (43e) up until the kinematic endpoint, where there is a noticeable deviation. Again, as was the case for MDM and EDM, the values of AM and CR are overall similar. However, as before, their mass dependence differs due to the presence of a γ^5, being more noticeable for AM. As done before for millicharged χ, the total event count is computed by integrating the differential event count in Fig. 30 and 31. The results of this can be seen in Tab. 4. It shows the predicted events of the four EM form factors for four different masses, with their couplings and the electrons on target N_{EOT} factored out.

Table 4: The predicted detection events of produced χ particles for the four EM form factor interactions at a beam energy of 100 MeV. All results are given with N_{EOT}, the number of total electrons incident on the beam dump, as well as the corresponding couplings, factored out.

	$N_{\mathrm{event}} \times (10^{-20} N_{\mathrm{EOT}})$	
m_χ(MeV)	MDM	EDM
0.001	$4.2 \times 10^{15} (\mu_\chi/\mu_B)^4$	$4.2 \times 10^{15} (d_\chi/\mu_B)^4$
0.01	$4.4 \times 10^{15} (\mu_\chi/\mu_B)^4$	$4.1 \times 10^{15} (d_\chi/\mu_B)^4$
0.1	$4.4 \times 10^{15} (\mu_\chi/\mu_B)^4$	$2.9 \times 10^{15} (d_\chi/\mu_B)^4$
1	$9.5 \times 10^{14} (\mu_\chi/\mu_B)^4$	$1.5 \times 10^{14} (d_\chi/\mu_B)^4$

	$N_{\mathrm{event}} \times (10^{-20} N_{\mathrm{EOT}})$	
m_χ(MeV)	AM	CR
0.001	$6.3 \times 10^{-6} (a_\chi/\mathrm{GeV}^{-2})^4$	$6.3 \times 10^{-6} (b_\chi/\mathrm{GeV}^{-2})^4$
0.01	$6.3 \times 10^{-6} (a_\chi/\mathrm{GeV}^{-2})^4$	$6.3 \times 10^{-6} (b_\chi/\mathrm{GeV}^{-2})^4$
0.1	$6.2 \times 10^{-6} (a_\chi/\mathrm{GeV}^{-2})^4$	$6.3 \times 10^{-6} (b_\chi/\mathrm{GeV}^{-2})^4$
1	$2.4 \times 10^{-6} (a_\chi/\mathrm{GeV}^{-2})^4$	$4.1 \times 10^{-6} (b_\chi/\mathrm{GeV}^{-2})^4$

10 Constraints of Millicharged and Electromagnetic Form Factor Dark Matter

Before discussing the implications of the results from above, it is necessary to briefly discuss existing constraints of the DM model discussed here, originating from different sources. Broadly speaking, there are three types of constraints: astrophysical observations, including the CMB; high-energy experiments and DM direct detection; high-precision SM observables.

First, we will look at the constraints of millicharged χ. These were already discussed in the intro of this work and can be seen in Fig. 8. The mass range of DM investigated here is in the most constrained region for millicharge, coming mostly from astrophysical observations, like the supernova SN1987A, red giants and white dwarfs and the CMB [28]. Importantly, however, in the mass range of 0.1 MeV to 100 MeV there was also a DM direct detection experiment for millicharges smaller than about $10^{-5}e$ to $10^{-3}e$, depending on the mass of χ, called MilliQ [74]. MilliQ was carried out at SLAC and had a similar premise to the potential set-up, that was used for the calculation of the predicted events in this work, described earlier. In conclusion, the experimental window that is still unexplored by direct detection ranges between the masses of 0.1 MeV to 0.5 MeV and millicharge of $9 \times 10^{-5}e$ to $6 \times 10^{-6}e$ per [50]. This window could be probed by the method described here.

Now we will look closer at the constraints for the EM form factors. A potential DM candidate with EM form factors is limited by how much it would effect SM precision observables, were it to exist. This can already give strong constraints from tree level contributions, and even more so for loops. Important to note is, however, that these calculations are usually model dependent as, for instance, other new particles could lead to cancellations. A direct detection signal of some new particle, on the other hand, would be independent of the model. We will briefly discuss these SM constraints taken from [51]. The EM form factors would naturally contribute to the vacuum polarisation of the photon and hence to the running of the fine structure constant α. The χ mass independent limit for the form factors are thus [51]

$$|\mu_\chi|, |d_\chi| \leq 3.2 \times 10^{-6} \mu_B \quad \text{and} \quad |a_\chi|, |b_\chi| \leq 3.2 \times 10^{-5}\,\text{GeV}^{-2}. \tag{110}$$

The χ particles would then also contribute to the triangle loop diagram that induces the anomalous magnetic moment of the electron, but especially of the muon. In the muon case, there is tension between the theoretical predication and the measured value [75]. This tension could be explained by a new particle, potentially providing additional motivation for χ, independent of its possible DM nature. The limits on the form factors from this are maximal if χ explains the tension fully, and are otherwise weaker. As can be seen in [51], in the mass region investigated here, the constraints coming from this are already bounded by other effects. It is, however, important to mention that recent lattice simulations indicate that the tension in the anomalous magnetic moment of the muon can potentially be fully explained by SM physics [76]. Another set of constraints come from high energy experiments. In colliders there is a certain amount of known energy going into a collision. When the resulting products are subsequently measured and their total energy is summed up, this sum does not add up to the total energy that was put into the collision. This is called missing energy and comes from final state particle that were not measured. This often includes weakly interacting particles like neutrinos, but could also potentially include BSM particles, like χ. Since the amount of missing energy is known, χ particles can only contribute less than it. This puts constraints on the EM form factors. The limits on the dipole interactions MDM and EDM [77], as well as AM and CR [51], from this are

$$|\mu_\chi|, |d_\chi| \leq 1.3 \times 10^{-5} \mu_B \quad \text{and} \quad |a_\chi|, |b_\chi| \leq 1.5 \times 10^{-5}\,\text{GeV}^{-2} \tag{111}$$

While these limits appear more stringent than (110), they depend on how one analyses the data from the detector, in this case specifically LEP. Additionally, due to the high energies that are usually probed in collider experiments, these limits can be sensitive to the UV, as the EFTs describing the form factor interactions likely break done at those scales.

Lastly, for the purpose of this work, it is especially interesting to investigate astrophysical and DM limits. Existing DM direct detection results for non-relativistic sub-MeV mass χ constrains MDM similarly to (110) and (111), while EDM, AM and CR are only weakly constrained at the masses considered here [51]. Similarly to millicharged χ, form factor DM would effect astrophysical processes. An example for these are supernovae. DM introduces additional cooling of the collapsing core by carrying away energy, assuming it interacts sufficiently weakly. This puts a bound on the couplings of χ, due to observational bounds on how quickly the core of a supernova cools. On a different scale, DM with form factors would necessarily self-interact. This would effect the distribution of DM in regions of high density, like the DM halos of galaxies, changing their shapes and velocity profile. However, for sub-MeV mass χ with non-relativistic velocities, these constraints are weak relative to the SM bounds discussed above. Another important class of DM constraints come from cosmological observations. DM behaves similarly to neutrinos in the early universe and decouple from the thermal bath much earlier than SM particles. The time of this χ-decoupling is determined by the form factor coupling. Since dark matter is responsible for the large scale structure (LSS) of the universe, late DM decoupling would imprint itself by over-damping the LSS. This puts an upper bound on the size of the form factors. These bounds are also less stringent than those from SM observables [51].

11 Conclusion

A novel millicharged particle χ of mass between 1 keV and 1 MeV could be observed for the described accelerator and CCD-detector set-up. This is especially interesting in the unconstrained window seen in Fig. 8. For instance, the predicted events in Tab. 3 for a χ of mass 0.1 MeV, a millicharge of 10^{-5} and 10^{20} total incident electrons on the beam dump are 2.2, with a beam energy of 100 MeV. Additionally, this can be improved by increasing the energy of the electron beam and/or the electrons on target. This could be achieved by more beam time or, in case of a pulsed beam, by more pulses. For EM form factor interactions, however, at a beam energy of 100 MeV, the predicted events at the detector are well below one for couplings that are not already excluded, as can be seen in Tab. 4. Even increasing the beam energy or the electrons on target does not move the prediction into a detectable range. The ambition in this thesis was also to develop the four-body phase space fully analytically from scratch, which was achieved successfully.

The calculation of the production of χ particles involves the eight Feynman diagrams (21) and (22). Since it is identical particles (electrons) that scatter, we cannot neglect any of the diagrams and need to take into account the additional u-channel exchange diagrams. This leads to a large number of terms in the scattering matrix element. Furthermore, the mass range investigated here also coincides with the mass of the electrons being scattered, meaning that we cannot make any approximation by neglecting the mass of electrons or of χ. Compounding this issue, the calculation needs to be fully relativistic. All this combined means that the matrix elements are very long expressions. These needed to be simplified in order to be able to compile them and numerically compute them.

Generally speaking, the numerical evaluation of the relevant five- and seven-dimensional integrals can be improved. The calculations were done with 80-bit extended precision floating point numbers. Although this enabled us to get reliable results without too much computing time, quad precision numbers would be preferable. Due to technical limitations however, this was infeasible for this work. The numerical demand, in part,likely traces back to a forward-peaked scattering process. Even more so, a general streamlining of the numerics using more powerful hardware would certainly improve the numerical stability of the lowest mass end considered in this work.

In conclusion, a millicharged particle of keV-MeV mass, in an unconstrained window of parameter space, could feasibly be observed by a potential underground accelerator-detector set-up 9 using novel, yet, inexpensive detectors for dark matter direct detection experiments. Particles with other EM form factors, however, could only be probed for couplings already excluded by other observations.

A Derivation of Feynman Rules

A more rigorous way to derive the Feynman rules for the couplings is the Feynman path integral [27, 53]. For this the effective action functional $\tilde{\Gamma}[\phi] = iS_{\text{int}}[\phi]$ is used, where S_{int} is the action of the interaction for which the Feynman rule is desired, and ϕ refers to a generic field. In order to derive said Feynman rule for a particular vertex $\{\phi(p_1), \ldots, \phi(p_n)\}$, the functional derivatives with respect to the fields are applied. Then one can use the relation between these, generic n-point functions, and the overall momentum conservation, to get

$$\{\phi(p_1), \ldots, \phi(p_n)\} = \frac{\delta^n \tilde{\Gamma}}{\delta\phi(p_1)\cdots\delta\phi(p_n)} = \frac{1}{(2\pi)^{4(n-1)}}\delta^{(4)}(p_1 + \ldots + p_n) i\Gamma^{(n)}(p_1, \ldots, p_n), \tag{A.1}$$

where $\delta\phi(p_i)$ refers to the functional derivative, and $i\Gamma^{(n)}$ is the vertex function for a given interaction. The path integral method ensures that all permutations of fields are accounted for and that the momentum dependency and combinatoric factors are correct. The general derivation for the 3-vertices of one photon and an DM particle pair is

$$\begin{aligned}
\{A^\mu(p_1), \chi(p_2), \bar{\chi}(p_3)\} &= \frac{\delta^3 \tilde{\Gamma}}{\delta A^\mu(p_1)\delta\chi(p_2)\delta\bar{\chi}(p_3)} = \frac{\delta^3(iS_{\text{int}})}{\delta A^\mu(p_1)\delta\chi(p_2)\delta\bar{\chi}(p_3)} \\
&= i\frac{\delta^3}{\delta A^\mu(p_1)\delta\chi(p_2)\delta\bar{\chi}(p_3)} \int d^4x\, d^4y\, d^4z\, \delta^{(4)}(x-y)\delta^{(4)}(x-z) \\
&\qquad\qquad \times \mathcal{L}_{\text{int}}(A(x), \chi(y), \bar{\chi}(z)) \\
&= i\frac{\delta^3}{\delta A^\mu(p_1)\delta\chi(p_2)\delta\bar{\chi}(p_3)} \int d^4x\, d^4y\, d^4z\, \delta^{(4)}(x-y)\delta^{(4)}(x-z) \\
&\quad \times \int \frac{d^4k_1\, d^4k_2\, d^4k_3}{(2\pi)^{3\cdot 4}} \mathcal{L}_{\text{int}}(A(k_1), \chi(k_2), \bar{\chi}(k_3)) e^{ik_1x} e^{ik_2y} e^{ik_3z} \\
&= i\int \frac{d^4k_1\, d^4k_2\, d^4k_3}{(2\pi)^{3\cdot 4}} (2\pi)^4 \delta^{(4)}(k_1+k_2+k_3) \frac{\delta^3 \mathcal{L}_{\text{int}}(A(k_1), \chi(k_2), \bar{\chi}(k_3))}{\delta A^\mu(p_1)\delta\chi(p_2)\delta\bar{\chi}(p_3)}.
\end{aligned} \tag{A.2}$$

Now, we only have to find the derivative $\frac{\delta^3 \mathcal{L}_{\text{int}}(A(k_1),\chi(k_2),\bar{\chi}(k_3))}{\delta A^\mu(p_1)\delta\chi(p_2)\delta\bar{\chi}(p_3)}$ in order to find the vertex function. The derivatives for the interaction (1a-1e) and (2a-2b) are

$$\frac{\delta^3 \mathcal{L}_{\varepsilon e}(A(k_1), \chi(k_2), \bar{\chi}(k_3))}{\delta A^\mu(p_1)\delta\chi(p_2)\delta\bar{\chi}(p_3)} = \varepsilon e \gamma_\mu \delta^{(4)}(p_1 - k_1)\delta^{(4)}(p_2 - k_2)\delta^{(4)}(p_3 - k_3), \tag{A.3a}$$

$$\frac{\delta^3 \mathcal{L}_{\text{MDM}}(A(k_1), \chi(k_2), \bar{\chi}(k_3))}{\delta A^\mu(p_1)\delta\chi(p_2)\delta\bar{\chi}(p_3)} = i\mu_\chi \sigma_{\mu\nu} k_1^\nu \delta^{(4)}(p_1 - k_1)\delta^{(4)}(p_2 - k_2)\delta^{(4)}(p_3 - k_3), \tag{A.3b}$$

$$\frac{\delta^3 \mathcal{L}_{\text{EDM}}(A(k_1), \chi(k_2), \bar{\chi}(k_3))}{\delta A^\mu(p_1)\delta\chi(p_2)\delta\bar{\chi}(p_3)} = -d_\chi \sigma_{\mu\nu}\gamma^5 k_1^\nu \delta^{(4)}(p_1 - k_1)\delta^{(4)}(p_2 - k_2)\delta^{(4)}(p_3 - k_3), \tag{A.3c}$$

$$\begin{aligned}
\frac{\delta^3 \mathcal{L}_{\text{AM}}(A(k_1), \chi(k_2), \bar{\chi}(k_3))}{\delta A^\mu(p_1)\delta\chi(p_2)\delta\bar{\chi}(p_3)} &= -a_\chi \left(k_1^2 \gamma_\mu - k_{1,\mu} \not{k}_1\right) \gamma^5 \\
&\quad \times \delta^{(4)}(p_1 - k_1)\delta^{(4)}(p_2 - k_2)\delta^{(4)}(p_3 - k_3),
\end{aligned} \tag{A.3d}$$

$$\frac{\delta^3 \mathcal{L}_{\text{CR}}(A(k_1), \chi(k_2), \bar{\chi}(k_3))}{\delta A^\mu(p_1)\delta\chi(p_2)\delta\bar{\chi}(p_3)} = b_\chi \left(k_1^2 \gamma_\mu - k_{1,\mu} \not{k}_1\right) \delta^{(4)}(p_1 - k_1)\delta^{(4)}(p_2 - k_2)\delta^{(4)}(p_3 - k_3), \tag{A.3e}$$

$$
\begin{aligned}
\frac{\delta^3\mathcal{L}_{\mathrm{Rs}}(A(k_1),A(k_2),\chi(k_3),\bar{\chi}(k_4))}{\delta A^\mu(p_1)\delta A^\nu(p_2)\delta\chi(p_3)\delta\bar{\chi}(p_4)} =& -\frac{1}{2}r_\chi\delta^{(4)}(p_3-k_3)\delta^{(4)}(p_4-k_4) \\
&\times\Big[\delta^{(4)}(p_1-k_1)\delta^{(4)}(p_2-k_2)\left(k_1\cdot k_2\eta_{\mu\nu}-k_{2,\mu}k_{1,\nu}\right) \\
&\quad+\delta^{(4)}(p_1-k_2)\delta^{(4)}(p_2-k_1)\left(k_2\cdot k_1\eta_{\mu\nu}-k_{1,\mu}k_{2,\nu}\right)\Big],
\end{aligned} \tag{A.3f}
$$

$$
\begin{aligned}
\frac{\delta^3\mathcal{L}_{\mathrm{Rp}}(A(k_1),A(k_2),\chi(k_3),\bar{\chi}(k_4))}{\delta A^\mu(p_1)\delta A^\nu(p_2)\delta\chi(p_3)\delta\bar{\chi}(p_4)} =& -i\bar{r}_\chi\varepsilon^{\mu\nu\sigma\rho}k_{1,\sigma}k_{2,\rho}\gamma^5\delta^{(4)}(p_3-k_3)\delta^{(4)}(p_4-k_4) \\
&\times\delta^{(4)}(p_1-k_2)\delta^{(4)}(p_2-k_1),
\end{aligned} \tag{A.3g}
$$

where the 4-vertices also use the relation (A.1) and a similar derivation to (A.2) for an additional photon. Although in that case, care has to be taken to account for the indistinguishable photons. After integrating over the redundant momentum variables, the Feynman vertex rules (3a-3g) are obtained.

B Four-Body Phase Space Integration Limits

Here we present the detailed derivation of the integration limits of t_{13} and t_{14}. Starting with

$$
t_{13}=(p_1-p_3)^2=m_N^2+m_X^2-2E_1E_3+2|\vec{p}_1||\vec{p}_3|\cos\theta_{13} \tag{B.1}
$$

in the CM frame $\vec{q}_{34\bar{\chi}}=0$. The limits of (B.1) are determined by the extreme values of the angle. Taking $\cos\theta_{13}$ to be ±1 lets us derive the three-momenta $|\vec{p}_1|,|\vec{p}_3|$ similarly to 84, starting with

$$
\begin{aligned}
\vec{p}_1^{\,2}&=\frac{1}{s_{34\bar{\chi}}}(q_{34\bar{\chi}}\cdot p_1)^2-p_1^2=\frac{1}{4s_{34\bar{\chi}}}\Big[(t_{2\chi}-s_{34\bar{\chi}}-m_N^2)^2-4s_{34\bar{\chi}}m_N^2\Big] \\
&=\frac{1}{4s_{34\bar{\chi}}}\lambda(t_{2\chi},s_{34\bar{\chi}},m_N^2)
\end{aligned} \tag{B.2}
$$

and having used $q_{34\bar{\chi}}\cdot p_1=\sqrt{s_{34\bar{\chi}}}E_1$. For the other three-momentum, we have

$$
\begin{aligned}
\vec{p}_3^{\,2}&=\frac{1}{s_{34\bar{\chi}}}(q_{34\bar{\chi}}\cdot p_3)^2-p_3^2=\frac{1}{4s_{34\bar{\chi}}}\Big[(s_{4\bar{\chi}}-s_{34\bar{\chi}}-m_X^2)^2-4s_{34\bar{\chi}}m_X^2\Big] \\
&=\frac{1}{4s_{34\bar{\chi}}}\lambda(s_{4\bar{\chi}},s_{34\bar{\chi}},m_X^2),
\end{aligned} \tag{B.3}
$$

having used $q_{34\bar{\chi}}\cdot p_3=\sqrt{s_{34\bar{\chi}}}E_3$. Re-expressing the energy term in (B.1) using the results obtained just now, and assuring that it remains positive, yields

$$
\begin{aligned}
E_1E_3&=\frac{1}{4s_{34\bar{\chi}}}\sqrt{4s_{34\bar{\chi}}m_N^2+\lambda(s_{34\bar{\chi}},t_{2\chi},m_N^2)}\sqrt{4s_{34\bar{\chi}}m_X^2+\lambda(s_{34\bar{\chi}},s_{4\bar{\chi}},m_X^2)} \\
&=\frac{1}{4s_{34\bar{\chi}}}\sqrt{(t_{2\chi}-s_{34\bar{\chi}}-m_N^2)^2}\sqrt{(s_{4\bar{\chi}}-s_{34\bar{\chi}}-m_X^2)^2} \\
&=\frac{1}{4s_{34\bar{\chi}}}(s_{34\bar{\chi}}+m_N^2-t_{2\chi})(s_{34\bar{\chi}}+m_X^2-s_{34\bar{\chi}}),
\end{aligned} \tag{B.4}
$$

recalling that $s_{34\bar{\chi}}>s_{4\bar{\chi}}$. Thus, the physical integration limits of t_{13} from (88) are obtained. Moving on to

$$
t_{14}=(p_1-p_4)^2=m_N^2+m_e^2-2E_1E_4+2|\vec{p}_1||\vec{p}_4|\cos\theta_{14} \tag{B.5}
$$

in the CM frame $\vec{q}_{4\bar{\chi}} = 0$. The derivation for the limits of (B.5) is exactly the same as above, just with the momenta $|\vec{p}_1|, |\vec{p}_4|$. We start with

$$\begin{aligned} \vec{p}_1^{\,2} &= \frac{1}{s_{4\bar{\chi}}}(q_{4\bar{\chi}} \cdot p_1)^2 - p_1^2 = \frac{1}{4s_{4\bar{\chi}}}\left[(q_{23\chi}^2 - s_{4\bar{\chi}} - m_N^2)^2 - 4s_{4\bar{\chi}}m_N^2\right] \\ &= \frac{1}{4s_{4\bar{\chi}}}\lambda(q_{23\chi}^2, s_{4\bar{\chi}}, m_N^2), \end{aligned} \tag{B.6}$$

having used $q_{4\bar{\chi}} \cdot p_1 = \sqrt{s_{4\bar{\chi}}}E_1$. The remaining momentum is

$$\begin{aligned} \vec{p}_4^{\,2} &= \frac{1}{s_{4\bar{\chi}}}(q_{4\bar{\chi}} \cdot p_4)^2 - p_4^2 = \frac{1}{4s_{4\bar{\chi}}}\left[(m_\chi^2 - s_{4\bar{\chi}} - m_e^2)^2 - 4s_{4\bar{\chi}}m_e^2\right] \\ &= \frac{1}{4s_{4\bar{\chi}}}\lambda(s_{4\bar{\chi}}, m_\chi^2, m_e^2), \end{aligned} \tag{B.7}$$

having used $q_{34\bar{\chi}} \cdot p_4 = \sqrt{s_{4\bar{\chi}}}E_4$. Again, we re-express the energy term of (B.5) and assure positivity, yielding

$$\begin{aligned} E_1E_4 &= \frac{1}{4s_{4\bar{\chi}}}\sqrt{4s_{4\bar{\chi}}m_N^2 + \lambda(q_{23\chi}^2, s_{4\bar{\chi}}, m_N^2)}\sqrt{4s_{4\bar{\chi}}m_e^2 + \lambda(s_{4\bar{\chi}}, m_\chi^2, m_e^2)} \\ &= \frac{1}{4s_{4\bar{\chi}}}\sqrt{(q_{23\chi}^2 - s_{4\bar{\chi}} - m_N^2)^2}\sqrt{(m_\chi^2 - s_{4\bar{\chi}} - m_e^2)^2} \\ &= \frac{1}{4s_{4\bar{\chi}}}(s_{4\bar{\chi}} + m_N^2 - q_{23\chi}^2)(s_{4\bar{\chi}} + m_e^2 - m_\chi^2), \end{aligned} \tag{B.8}$$

recalling that $s_{4\bar{\chi}} > m_\chi$. Thus, we have the physical integration limits of t_{14} from (89).

C Scalar Products in Lorentz Invariants

Here we will express all of the 14 scalar products (SPs), excluding $p_1 \cdot p_2 = m_N E_2 = (s - m_N^2 - m_e^2)/2$, in terms of masses and invariants. In order to do this, first we rewrite seven SPs directly using the definitions of the invariants (53)

$$\begin{aligned} p_1 \cdot p_3 &= \frac{1}{2}\left(m_N^2 + m_X^2 - t_{13}\right), \\ p_1 \cdot p_4 &= \frac{1}{2}\left(m_N^2 + m_e^2 - t_{14}\right), \\ p_2 \cdot p_\chi &= \frac{1}{2}\left(m_e^2 + m_\chi^2 - t_{2\chi}\right), \\ p_3 \cdot p_{\bar{\chi}} &= \frac{1}{2}\left(s_{34\bar{\chi}} - s_{4\bar{\chi}} - m_X^2 - 2p_3 \cdot p_4\right), \\ p_4 \cdot p_{\bar{\chi}} &= \frac{1}{2}\left(s_{4\bar{\chi}} - m_e^2 - m_\chi^2\right), \end{aligned} \tag{C.1}$$

and $p_2 \cdot p_3$ from (70), as well as $p_3 \cdot p_4$ from (64), which can both also be expressed purely in terms of invariants and masses. After eliminating these seven SPs, seven are still left. As described in the main text, $p_\chi \cdot p_{\bar{\chi}}$ is determined through the Gram determinant, as can be seen in Fig. 20, and subsequently expressed only with invariants and masses. We will not write down the explicit form for this SP, as it is very long.

For the remaining six it is necessary to use a different method. By utilising overall four-momentum conservation, it is possible to derive six relations that express SPs in terms of other SPs, like so:

$$
\begin{aligned}
p_1 \cdot p_\chi &= p_3 \cdot p_\chi + p_4 \cdot p_\chi + m_\chi^2 + p_\chi \cdot p_{\bar\chi} - p_2 \cdot p_\chi \\
&= \frac{1}{2}\left(s + s_{4\bar\chi} - s_{34\bar\chi} + t_{14} - t_{13} - m_N^2 + 2p_3 \cdot p_4 - 2p_\chi \cdot p_{\bar\chi}\right), \\
p_1 \cdot p_{\bar\chi} &= \frac{1}{2}\left(t_{13} + s_{4\bar\chi} - t_{2\chi} - 2p_1 \cdot p_4 + 2p_3 \cdot p_4 + 2p_3 \cdot p_{\bar\chi}\right) \\
&= \frac{1}{2}\left(s_{34\bar\chi} + t_{13} + t_{14} - m_N^2 - m_X^2 - m_e^2 - t_{2\chi}\right), \\
p_2 \cdot p_4 &= p_1 \cdot p_2 + m_e^2 - p_2 \cdot p_3 - p_2 \cdot p_\chi - p_2 \cdot p_{\bar\chi} \\
&= \frac{1}{2}\left(s + t_{13} + t_{14} - 2m_N^2 - 2m_\chi^2 + 2p_3 \cdot p_4 - 2p_2 \cdot p_3 - 2p_\chi \cdot p_{\bar\chi}\right), \\
p_2 \cdot p_{\bar\chi} &= p_3 \cdot p_{\bar\chi} + p_4 \cdot p_{\bar\chi} + p_\chi \cdot p_{\bar\chi} + m_\chi^2 - p_1 \cdot p_{\bar\chi} \\
&= \frac{1}{2}\left(t_{2\chi} + m_\chi^2 + m_N^2 - t_{13} - t_{14} + 2p_\chi \cdot p_{\bar\chi} - 2p_3 \cdot p_4\right), \\
p_3 \cdot p_\chi &= p_1 \cdot p_3 + p_2 \cdot p_3 - m_X^2 - p_3 \cdot p_4 - p_3 \cdot p_{\bar\chi} \\
&= \frac{1}{2}\left(s_{4\bar\chi} + m_N^2 - s_{34\bar\chi} - t_{13} + 2p_2 \cdot p_3\right), \\
p_4 \cdot p_\chi &= p_1 \cdot p_4 + p_2 \cdot p_4 - p_3 \cdot p_4 - m_e^2 - p_2 \cdot p_{\bar\chi} \\
&= \frac{1}{2}\left(s + t_{14} - t_{2\chi} - 3m_\chi^2 - 2m_N^2 - m_e^2 + 2p_3 \cdot p_4 - 2p_2 \cdot p_3 - 4p_\chi \cdot p_{\bar\chi}\right).
\end{aligned}
\tag{C.2}
$$

In our specific case, we just replace $m_N \to m_e$ and $m_X \to m_e$ to get the correct expressions for electron-electron scattering.

D Full DM Self-Scattering Matrix Elements

The full relativistic matrix elements of $\chi\chi$ scattering for the different interactions in terms of the masses and Mandelstam variables, defined in (46), are:

$$
|\mathcal{M}_{\chi\chi}|^2_{\varepsilon e} = 2\varepsilon^2 e^4 \left[\frac{s^2 + u^2 - 8m_\chi^4}{t^2} + 2\frac{28m_\chi^4 - 12m_\chi^2 s + s^2}{tu} + \frac{s^2 + t^2 - 8m_\chi^4}{u^2}\right], \tag{D.1a}
$$

$$
\begin{aligned}
|\mathcal{M}_{\chi\chi}|^2_{\mathrm{MDM}} = \mu_\chi^4 \Bigg[& \frac{4m_\chi^2}{t}\Big(32m_\chi^4 - 12m_\chi^2 s - 16m_\chi^2 u + s^2 + 3su + 2u^2\Big) \\
& + \frac{4m_\chi^2}{u}\Big(32m_\chi^4 - 12m_\chi^2 s - 16m_\chi^2 t + s^2 + 3st + 2t^2\Big) \\
& + \frac{1}{2}\Big(144m_\chi^4 - 56m_\chi^2 s + 13s^2 + t^2 + u^2\Big)\Bigg],
\end{aligned}
\tag{D.1b}
$$

$$
\begin{aligned}
|\mathcal{M}_{\chi\chi}|^2_{\mathrm{EDM}} = d_\chi^4 \Bigg[& -\frac{4m_\chi^2}{t}\Big(16m_\chi^4 - 12m_\chi^2 s - 8m_\chi^2 u + 2s^2 + 3su + u^2\Big) \\
& - \frac{4m_\chi^2}{u}\Big(16m_\chi^4 - 12m_\chi^2 s - 8m_\chi^2 t + 2s^2 + 3st + t^2\Big) \\
& + \frac{1}{2}\Big(48m_\chi^4 - 56m_\chi^2 s + 13s^2 + t^2 + u^2\Big)\Bigg],
\end{aligned}
\tag{D.1c}
$$

$$
\begin{aligned}
|\mathcal{M}_{\chi\chi}|^2_{\mathrm{AM}} = 2a_\chi^4 \Big[& s^4 + 2t^2u^2 - 192m_\chi^8 + 48m_\chi^6 s + 4m_\chi^4\Big(7s^2 + 6t^2 + 8tu + 6u^2\Big) \\
& - m_\chi^2\Big(11s^3 + 3t^3 + 5t^2u + 5tu^2 + 3u^3\Big)\Big],
\end{aligned} \tag{D.1d}
$$

$$
\begin{aligned}
|\mathcal{M}_{\chi\chi}|^2_{\mathrm{CR}} = 2b_\chi^4 \Big[& s^4 + 2t^2u^2 + 128m_\chi^8 - 128m_\chi^6 s + 8m_\chi^4\Big(7s^2 - tu\Big) \\
& - 4m_\chi^2\Big(3s^3 + stu - t^3 - u^3\Big)\Big].
\end{aligned} \tag{D.1e}
$$

Additionally, the full relativistic matrix elements of $\chi\bar{\chi}$ scattering for the different interactions in terms of the masses and Mandelstam variables, defined in (46), are:

$$
|\mathcal{M}_{\chi\bar{\chi}}|^2_{\varepsilon e} = 2\varepsilon^2 e^4 \left[\frac{t^2 + u^2 - 8m_\chi^4}{s^2} + 2\frac{28m_\chi^4 - 12m_\chi^2 u + u^2}{st} + \frac{s^2 + u^2 - 8m_\chi^4}{t^2}\right], \tag{D.2a}
$$

$$
\begin{aligned}
|\mathcal{M}_{\chi\bar{\chi}}|^2_{\mathrm{MDM}} = \mu_\chi^4 \Big[& \frac{4m_\chi^2}{t}\Big(32m_\chi^4 - 12m_\chi^2 u - 16m_\chi^2 s + u^2 + 3su + 2s^2\Big) \\
& + \frac{4m_\chi^2}{s}\Big(32m_\chi^4 - 12m_\chi^2 u - 16m_\chi^2 t + u^2 + 3tu + 2t^2\Big) \\
& + \frac{1}{2}\Big(144m_\chi^4 - 56m_\chi^2 u + 13u^2 + t^2 + s^2\Big)\Big],
\end{aligned} \tag{D.2b}
$$

$$
\begin{aligned}
|\mathcal{M}_{\chi\bar{\chi}}|^2_{\mathrm{EDM}} = d_\chi^4 \Big[& -\frac{4m_\chi^2}{s}\Big(16m_\chi^4 - 12m_\chi^2 u - 8m_\chi^2 t + 2u^2 + 3tu + t^2\Big) \\
& - \frac{4m_\chi^2}{t}\Big(16m_\chi^4 - 12m_\chi^2 u - 8m_\chi^2 s + 2u^2 + 3su + s^2\Big) \\
& + \frac{1}{2}\Big(48m_\chi^4 - 56m_\chi^2 u + 13u^2 + t^2 + s^2\Big)\Big],
\end{aligned} \tag{D.2c}
$$

$$
\begin{aligned}
|\mathcal{M}_{\chi\bar{\chi}}|^2_{\mathrm{AM}} = 2a_\chi^4 \Big[& u^4 + 2s^2t^2 - 192m_\chi^8 + 48m_\chi^6 u + 4m_\chi^4\Big(7u^2 + 6t^2 + 8st + 6s^2\Big) \\
& - m_\chi^2\Big(11u^3 + 3t^3 + 5st^2 + 5s^2t + 3s^3\Big)\Big],
\end{aligned} \tag{D.2d}
$$

$$
\begin{aligned}
|\mathcal{M}_{\chi\bar{\chi}}|^2_{\mathrm{CR}} = 2b_\chi^4 \Big[& u^4 + 2s^2t^2 + 128m_\chi^8 - 128m_\chi^6 u + 8m_\chi^4\Big(7u^2 - st\Big) \\
& - 4m_\chi^2\Big(3u^3 + stu - t^3 - s^3\Big)\Big].
\end{aligned} \tag{D.2e}
$$

Expectedly, due to the crossing symmetry of the u and s-channel at tree level for the processes considered, the swap $s \leftrightarrow u$ of the results in (D.1) yields the correct matrix elements for $\chi\bar{\chi}$ scattering. Furthermore, one can notice that the difference of the matrix elements for effective operators which have equivalent Dirac structure only up to a γ^5, ignoring coupling factors, are terms proportional to the mass m_χ of the particles, again as expected.

References

[1] Zwicky, F. "Die Rotverschiebung von extragalaktischen Nebeln". *Helvetica Physica Acta* 6 (1933), pp. 110–127.

[2] V. C. Rubin, N. Thonnard and J. Ford W. K. "Rotational properties of 21 SC galaxies with a large range of luminosities and radii, from NGC 4605 (R = 4kpc) to UGC 2885 (R = 122 kpc)". *The Astrophysical Journal* 238 (1980), p. 471.

[3] G. Bertone and D. Hooper. "History of Dark Matter". *Reviews of Modern Physics* 90.4 (2018), p. 045002. arXiv: `1605.04909 [astro-ph.CO]`.

[4] A. A. Penzias and R. W. Wilson. "A Measurement of Excess Antenna Temperature at 4080 Mc/s." *The Astrophysical Journal* 142 (1965), p. 419.

[5] S. Weinberg. *Cosmology*. Oxford Univ. Press, 2008. ISBN: 9780198526827.

[6] G. Bertone, ed. *Particle Dark Matter: Observations, Models and Searches*. Cambridge University Press, 2010. ISBN: 9781107653924.

[7] P. Tisserand et al. "Limits on the Macho content of the Galactic Halo from the EROS-2 Survey of the Magellanic Clouds". *Astronomy & Astrophysics* 469.2 (2007), pp. 387–404. arXiv: `astro-ph/0607207`.

[8] D. Clowe, A. Gonzalez and M. Markevitch. "Weak-Lensing Mass Reconstruction of the Interacting Cluster 1E 0657-558: Direct Evidence for the Existence of Dark Matter". *The Astrophysical Journal* 604.2 (2004), pp. 596–603. arXiv: `astro-ph/0312273`.

[9] H. Hoekstra, H. K. C. Yee and M. D. Gladders. "Properties of Galaxy Dark Matter Halos from Weak Lensing". *The Astrophysical Journal* 606.1 (2004), pp. 67–77. arXiv: `astro-ph/0306515`.

[10] M. Bradač et al. "Revealing the Properties of Dark Matter in the Merging Cluster MACS J0025.4-1222". *The Astrophysical Journal* 687.2 (2008), pp. 959–967. arXiv: `0806.2320 [astro-ph]`.

[11] M. Markevitch et al. "Direct Constraints on the Dark Matter Self-Interaction Cross Section from the Merging Galaxy Cluster 1E 0657-56". *The Astrophysical Journal* 606.2 (2004), pp. 819–824. arXiv: `astro-ph/0309303`.

[12] D. Clowe et al. "A Direct Empirical Proof of the Existence of Dark Matter". *The Astrophysical Journal* 648.2 (2006), pp. L109–L113. arXiv: `astro-ph/0608407`.

[13] N. Aghanim et al. "Planck2018 results: VI. Cosmological parameters". *Astronomy & Astrophysics* 641 (2020), A6. arXiv: `1807.06209 [astro-ph.CO]`.

[14] N. Aghanim et al. "Planck2018 results: V. CMB power spectra and likelihoods". *Astronomy & Astrophysics* 641 (2020), A5. arXiv: `1907.12875 [astro-ph.CO]`.

[15] W. Hu and N. Sugiyama. "Small-Scale Cosmological Perturbations: An Analytic Approach". *The Astrophysical Journal* 471.2 (1996), pp. 542–570. arXiv: `astro-ph/9510117`.

[16] V. Springel et al. "Simulations of the formation, evolution and clustering of galaxies and quasars". *Nature* 435.7042 (2005), pp. 629–636. arXiv: `astro-ph/0504097`.

[17] V. Springel et al. "First results from the IllustrisTNG simulations: matter and galaxy clustering". *Monthly Notices of the Royal Astronomical Society* 475.1 (2017), pp. 676–698. arXiv: `1707.03397 [astro-ph.GA]`.

[18] M. Milgrom. "A modification of the Newtonian dynamics as a possible alternative to the hidden mass hypothesis". *The Astrophysical Journal* 270 (1983), p. 365.

[19] B. Paczynski. "Gravitational microlensing by the galactic halo". *The Astrophysical Journal* 304 (1986), p. 1.

[20] K. Griest. “Galactic microlensing as a method of detecting massive compact halo objects”. *The Astrophysical Journal* 366 (1991), p. 412.

[21] B. Carr et al. “Constraints on primordial black holes”. *Reports on Progress in Physics* 84.11 (2021), p. 116902. arXiv: 2002.12778 [astro-ph.CO].

[22] J. Yoo, J. Chaname and A. Gould. “The End of the MACHO Era: Limits on Halo Dark Matter from Stellar Halo Wide Binaries”. *The Astrophysical Journal* 601.1 (2004), pp. 311–318. arXiv: astro-ph/0307437.

[23] D. Carney et al. “Proposal for gravitational direct detection of dark matter”. *Physical Review D* 102.7 (2020), p. 072003. arXiv: 1903.00492 [hep-ph].

[24] L. J. Hall et al. “Freeze-in production of FIMP dark matter”. *Journal of High Energy Physics* 2010.3 (2010). arXiv: 0911.1120 [hep-ph].

[25] J. R. Primack. “Whatever Happened to Hot Dark Matter?” (2001). arXiv: astro-ph/0112336.

[26] J. Lesgourgues and S. Pastor. “Neutrino Mass from Cosmology”. *Advances in High Energy Physics* 2012 (2012), pp. 1–34. arXiv: 1212.6154 [hep-ph].

[27] M. D. Schwartz. *Quantum Field Theory and the Standard Model*. Cambridge University Press, 2013. ISBN: 9781107034730.

[28] M. Fabbrichesi, E. Gabrielli and G. Lanfranchi. *The Physics of the Dark Photon: A Primer*. Springer International Publishing, 2021. ISBN: 9783030625191. arXiv: 2005.01515 [hep-ph].

[29] Q. R. Ahmad et al. “Measurement of the Rate of $\nu_e + d \to p + p + e^-$ Interactions Produced by ^{8}B Solar Neutrinos at the Sudbury Neutrino Observatory”. *Physical Review Letters* 87.7 (2001), p. 071301. arXiv: nucl-ex/0106015.

[30] H. Murayama. *Supersymmetry Phenomenology*. 2000. arXiv: hep-ph/0002232.

[31] S. Weinberg. “A New Light Boson?” *Physical Review Letters* 40.4 (1978), pp. 223–226.

[32] F. Wilczek. “Problem of Strong P and T Invariance in the Presence of Instantons”. *Physical Review Letters* 40.5 (1978), pp. 279–282.

[33] R. D. Peccei and H. R. Quinn. “CP Conservation in the Presence of Pseudoparticles”. *Physical Review Letters* 38.25 (1977), pp. 1440–1443.

[34] R. D. Peccei and H. R. Quinn. “Constraints imposed by CP conservation in the presence of pseudoparticles”. *Physical Review D* 16.6 (1977), pp. 1791–1797.

[35] R. D. Peccei. “The Strong CP Problem and Axions”. *Axions*. Springer Berlin Heidelberg, 2008, pp. 3–17. ISBN: 9783540735182. arXiv: hep-ph/0607268.

[36] P. F. de Salas and A. Widmark. “Dark matter local density determination: recent observations and future prospects”. *Reports on Progress in Physics* 84.10 (2021), p. 104901. arXiv: 2012.11477 [astro-ph.GA].

[37] ATLAS Collaboration. “The quest to discover supersymmetry at the ATLAS experiment” (2024). arXiv: 2403.02455 [hep-ex].

[38] E. Aprile et al. “The XENONnT dark matter experiment”. *Eur. Phys. J. C* 84.8 (2024), p. 784. arXiv: 2402.10446 [physics.ins-det].

[39] A. H. Abdelhameed et al. “First results from the CRESST-III low-mass dark matter program”. *Phys. Rev. D* 100.10 (2019), p. 102002. arXiv: 1904.00498 [astro-ph.CO].

[40] S. Asztalos et al. “Large-scale microwave cavity search for dark-matter axions”. *Phys. Rev. D* 64.9 (2001), p. 092003.

[41] Y. Kahn and T. Lin. “Searches for light dark matter using condensed matter systems”. *Rept. Prog. Phys.* 85.6 (2022), p. 066901. arXiv: 2108.03239 [hep-ph].

[42] J. Tiffenberg et al. "Single-Electron and Single-Photon Sensitivity with a Silicon Skipper CCD". *Phys. Rev. Lett.* 119.13 (2017), p. 131802. arXiv: `1706.00028 [physics.ins-det]`.

[43] L. Barak et al. "SENSEI: Direct-Detection Results on sub-GeV Dark Matter from a New Skipper-CCD". *Phys. Rev. Lett.* 125.17 (2020), p. 171802. arXiv: `2004.11378 [astro-ph.CO]`.

[44] A. E. Chavarria et al. "DAMIC at SNOLAB". *Phys. Procedia* 61 (2015). Ed. by F. Avignone and W. Haxton, pp. 21–33. arXiv: `1407.0347 [physics.ins-det]`.

[45] J. Billard et al. "Direct detection of dark matter—APPEC committee report". *Rept. Prog. Phys.* 85.5 (2022), p. 056201. arXiv: `2104.07634 [hep-ex]`.

[46] N. Castelló-Mor. "DAMIC-M Experiment: Thick, Silicon CCDs to search for Light Dark Matter". *Nucl. Instrum. Meth. A* 958 (2020), p. 162933. arXiv: `2001.01476 [physics.ins-det]`.

[47] B. Dasgupta and J. Kopp. "Sterile Neutrinos". *Phys. Rept.* 928 (2021), pp. 1–63. arXiv: `2106.05913 [hep-ph]`.

[48] T. Bringmann et al. "Minimal sterile neutrino dark matter". *Phys. Rev. D* 107.7 (2023), p. L071702. arXiv: `2206.10630 [hep-ph]`.

[49] I. G. Irastorza and J. Redondo. "New experimental approaches in the search for axion-like particles". *Prog. Part. Nucl. Phys.* 102 (2018), pp. 89–159. arXiv: `1801.08127 [hep-ph]`.

[50] H. An et al. "Solar reflection of dark matter". *Phys. Rev. D* 104.10 (2021), p. 103026. arXiv: `2108.10332 [hep-ph]`.

[51] X. Chu, J. Pradler and L. Semmelrock. "Light dark states with electromagnetic form factors". *Physical Review D* 99.1 (2019), p. 015040. arXiv: `1811.04095 [hep-ph]`.

[52] N. Weiner and I. Yavin. "How dark are Majorana WIMPs? Signals from magnetic inelastic dark matter and Rayleigh dark matter". *Physical Review D* 86.7 (2012), p. 075021. arXiv: `1206.2910 [hep-ph]`.

[53] M. E. Peskin and D. V. Schroeder. *An Introduction to Quantum Field Theory.* CRC Press, 2019. ISBN: 9780367320560.

[54] I. B. Zel'Dovich. "ELECTROMAGNETIC INTERACTION WITH PARITY VIOLATION". *Soviet Phys. JETP* 6 (1958), pp. 1184–1186.

[55] B. J. Kavanagh, P. Panci and R. Ziegler. "Faint light from dark matter: classifying and constraining dark matter-photon effective operators". *Journal of High Energy Physics* 2019.4 (2019). arXiv: `1810.00033 [hep-ph]`.

[56] V. Barger, W.-Y. Keung and D. Marfatia. "Electromagnetic properties of dark matter: Dipole moments and charge form factor". *Phys. Lett. B* 696.1–2 (2011), pp. 74–78. arXiv: `1007.4345 [hep-ph]`.

[57] H. H. Patel. "Package-X: A Mathematica package for the analytic calculation of one-loop integrals". *Comput. Phys. Commun.* 197 (2015), pp. 276–290. arXiv: `1503.01469 [hep-ph]`.

[58] H. H. Patel. "Package-X 2.0: A Mathematica package for the analytic calculation of one-loop integrals". *Comput. Phys. Commun.* 218 (2017), pp. 66–70. arXiv: `1612.00009 [hep-ph]`.

[59] R. Mertig, M. Böhm and A. Denner. "Feyn Calc - Computer-algebraic calculation of Feynman amplitudes". *Computer Physics Communications* 64.3 (1991), pp. 345–359.

[60] V. Shtabovenko, R. Mertig and F. Orellana. "New developments in FeynCalc 9.0". *Computer Physics Communications* 207 (2016), pp. 432–444. arXiv: `1601.01167 [hep-ph]`.

[61] V. Shtabovenko, R. Mertig and F. Orellana. "FeynCalc 9.3: New features and improvements". *Computer Physics Communications* 256 (2020), p. 107478. arXiv: `2001.04407 [hep-ph]`.

[62] E. Byckling and K. Kajantie. *Particle Kinematics.* New York: Wiley, 1973. ISBN: 0471128856.

[63] T. Hahn. "Cuba—a library for multidimensional numerical integration". *Computer Physics Communications* 168.2 (2005), pp. 78–95. arXiv: `hep-ph/0404043`.

[64] W. S. Boyle and G. E. Smith. “Charge Coupled Semiconductor Devices”. *Bell System Technical Journal* 49.4 (1970), pp. 587–593.

[65] G. F. Amelio, M. F. Tompsett and G. E. Smith. “Experimental Verification of the Charge Coupled Device Concept”. *Bell System Technical Journal* 49.4 (1970), pp. 593–600.

[66] M. Traina et al. “Confirmation of the excess of ionization events in DAMIC at SNOLAB with skipper CCDs”. *PoS.* TAUP2023 TAUP2023 (2024), p. 059.

[67] A. Aguilar-Arevalo et al. “Search for low-mass WIMPs in a 0.6 kg day exposure of the DAMIC experiment at SNOLAB”. *Phys. Rev. D* 94.8 (2016), p. 082006. arXiv: `1607.07410 [astro-ph.CO]`.

[68] A. Aguilar-Arevalo et al. “First Direct-Detection Constraints on eV-Scale Hidden-Photon Dark Matter with DAMIC at SNOLAB”. *Phys. Rev. Lett.* 118.14 (2017), p. 141803. arXiv: `1611.03066 [astro-ph.CO]`.

[69] A. Aguilar-Arevalo et al. “Constraints on Light Dark Matter Particles Interacting with Electrons from DAMIC at SNOLAB”. *Phys. Rev. Lett.* 123.18 (2019), p. 181802. arXiv: `1907.12628 [astro-ph.CO]`.

[70] S. Lee, B. Kilminster and A. Macchiolo. “Dark Matter in CCDs at Modane (DAMIC-M) : A silicon detector apparatus searching for low-energy physics processes”. *JINST* 15.02 (2020). Ed. by M. Nessi, p. C02050. arXiv: `2001.01209 [physics.ins-det]`.

[71] I. J. Arnquist et al. “The DAMIC-M experiment: Status and first results”. *SciPost Phys. Proc.* 12.12 (2023), p. 014. arXiv: `2210.12070 [hep-ex]`.

[72] P. Privitera. “The DAMIC-M experiment: status and first results”. *PoS.* TAUP2023 TAUP2023 (2024), p. 066.

[73] Particle Data Group. “Review of particle physics”. *Phys. Rev. D* 110.3 (2024), p. 030001.

[74] A. A. Prinz et al. “Search for Millicharged Particles at SLAC”. *Phys. Rev. Lett.* 81.6 (1998), pp. 1175–1178. arXiv: `hep-ex/9804008`.

[75] D. P. Aguillard et al. “Measurement of the Positive Muon Anomalous Magnetic Moment to 0.20 ppm”. *Phys. Rev. Lett.* 131.16 (2023), p. 161802. arXiv: `2308.06230 [hep-ex]`.

[76] D. Djukanovic et al. “The hadronic vacuum polarization contribution to the muon g-2 at long distances” (2024). arXiv: `2411.07969 [hep-lat]`.

[77] J.-F. Fortin and T. M. P. Tait. “Collider Constraints on Dipole-Interacting Dark Matter”. *Phys. Rev. D* 85.6 (2012), p. 063506. arXiv: `1103.3289 [hep-ph]`.